Imperial College London

A Flexible Tool Design and Integrated Modelling Techniques for Springback Compensation in Creep-Age Forming

by

Aaron C L Lam

A thesis submitted to the
Department of Mechanical Engineering
Imperial College London

In conformity with the requirements for the Degree of Doctor of Philosophy and for the Diploma of the Imperial College London

London, November 2015

ACKNOWLEDGEMENTS

I wish to express my gratitude to the many people who have supported me during my PhD journey.

Primarily I would like to express my sincere gratitude to Prof. Jianguo Lin and Dr. Daniel Balint for the opportunity they had given me to join this research programme. I am most grateful to my supervisor, Prof. Jianguo Lin, for his invaluable guidance throughout my research. I have benefitted greatly from his immense knowledge of the field and his vision.

I would like to express my very great appreciation to Dr. Zhusheng Shi for his constructive advice and assistance. He had shared his time with me so generously and worked so tirelessly to safeguard the quality and accuracy of my work. I enjoyed working with him very much.

My grateful thanks extend to Prof. Trevor Dean for his much useful advice and critique during the design phase of the flexible creep-age forming tool. I also thank Mr. Yong Li and Mr. Yo-Lun Yang for their occasional help on my work.

The technical support I had received from Mr. Suresh Viswamathan Chettiar, Mr. Mark Holloway and Dr. Judith Thei and the collaboration with them in the laboratories had enabled on-time delivery of the experimental results essential to completing this thesis; for that I thank them. Particularly, Suresh had contributed

significantly in overcoming the many unforeseeable challenges associated to performing testing with a bespoke creep-age forming tool.

This research was performed at the Aviation Corporation of China (AVIC) Centre for Structural Design and Manufacture at Imperial College London. The strong support from AVIC Beijing Aeronautical Manufacturing Technology Research Institute (BAMTRI) for this funded research is much appreciated.

I wish to thank my senior colleagues of Room 361: Mr. Omer El Fakir, Dr. Erofili Kardoulaki, Dr. Nan Li and Dr. Aditya Narayanan. Their generous advice from past experience had helped me to settle quickly in a new environment thus let me to really focus on my research.

Special thanks go to Mr. Joseph Ahn and Mr. Lee Junyi, two members of the AVIC Centre 2012 cohort, for our many inspiring and stimulating – fruitful and fruitless – discussion sessions.

Last but not least, I wish to thank my family members, brothers, sisters, friends and *them* for their love, support and encouragement throughout my study and beyond. I will always be indebted to them.

Aaron C L Lam

DECLARATION OF ORIGINALITY

I hereby declare that this thesis 'A Flexible Tool Design and Integrated Modelling Techniques for Springback Compensation in Creep-Age Froming' and the work reported herein was composed by and originated entirely from me. Information derived from the published and unpublished work of others has been acknowledged in the text and references are given in the list of sources.

Aaron C L Lam

DECLARATION OF COPYRIGHT

Aaron C L Lam

ABSTRACT

This thesis presents the development of ad-hoc experimental and integrated modelling techniques for springback compensation in creep-age forming (CAF). A test programme is presented which describes the material and workpiece information and the test plans for the experimental evaluation of the creep-ageing and springback behaviour of aluminium alloy 7B04-T651 under 115 °C. Experimental results from the creep-ageing and tensile tests were used to determine a CAF material model for the alloy. A flexible tool design has been proposed and a laboratory-scale prototype has been delivered and used to perform the CAF tests in this research. The determined CAF material model and geometry of the flexible tool design were treated as input and used to construct a CAF process model using finite element (FE) method. Comparisons between final deflections of FE-simulated and experimentally formed plates validated the springback predictive ability of the FE process model. The model was eventually employed to model springback-compensated tool shapes and using the modelled tool shapes to perform CAF tests have produced formed plates that have an average 0.81 ± 0.14 mm of maximum absolute vertical difference from target shape. CAF can now be used to produce accurately shaped panel components in a laboratory environment using the equipment and techniques developed in this research.

LIST OF TABLES

LIST OF FIGURES

TABLE OF CONTENTS

CHAPTER 1.

INTRODUCTION

1.1. Manufacturing of extra-large panels for the transportation industry

Extra-large panel components make up a large proportion of the structural parts in modern-day vehicles across the transportation industry. They can be found in the form of fuselage panels of aircrafts, roof panels of trains, ship and submarine hulls and fuel tank skin panels of launch vehicles (Figure 1). Because of their extra-large dimensions, lightweighting them can significantly reduce the overall weight of the vehicle. Lightweighting is mainly driven by the requirement to increase payload for launch vehicles and to improve fuel-efficiency and reduce emissions for other modes of transport vehicle. In all cases, lightweighting needs to be achieved without compromising the capability of the component to withstand structural loads, which brings forth the concept of strength-to-weight ratio in structural components.

(a)

(b)

(c)

(d)

Figure 1. Extra-large transport vehicles. (a) Airbus A380 aircraft (Air France, 2011). (b) CSR Sifang CRH380A high-speed train (Yiyuan, 2013). (c) Virginia-class submarine (General Dynamics Electric Boat, n.d.). (d) European Ariane V launch vehicle (Ignis, 2006).

Lightweight panel components utilise the combination of advance materials and structural designs. Conventional lightweight panel components typically consist of a base panel with riveted or welded stiffeners to improve their strength specification (Figure 2a). The use of rivets and welds were later replaced by the practice of machining of integral features directly into the panels (Figure 2b), which have major advantages over the conventional method of construction in terms of product quality and manufacturing costs (Munroe *et al.*, 2000).

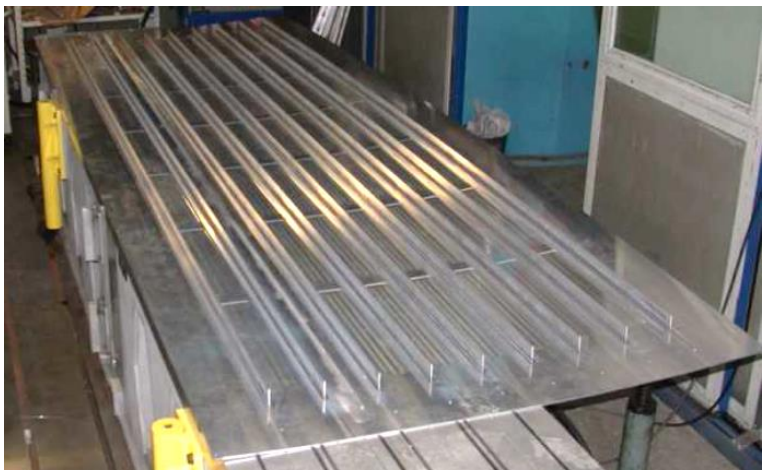

(a)

(b)

Figure 2. (a) A commercial aircraft fuselage panel with machined square pockets, laser beam welded stringers and friction stir welded neighbouring panels in the longitudinal direction. Adapted from Eberl *et al.* (2006). (b) Milling of integrally stiffened aerostructures (Premium AEROTEC, n.d.).

Because stiffeners are now incorporated to the primary structure, conventional forming technique such as roll forming and bump forming were soon

found inadequate for shaping integrally stiffened panel components (Holman, 1989). Creep-age forming (CAF) and shot-peen forming are amongst the few forming techniques that have been proven viable for the production of extra-large integrally stiffened panels in industrial settings (Zeng and Huang, 2008).

Shot-peen forming is a dieless process that utilises round metallic shots to impact metal surfaces. Each shot produces a combination of elastic stretching and compressive stress that cause the peened surface to develop a convex curvature. Accurately shaped components from shot-peening require a precise control on many process parameters including shot density, nozzle and shot characteristics, impact angle and exposure time (Petit-Renaud, 2006).

CAF refers to a process that concurrently shapes and heat-treats aluminium alloy components. As an alternative to shot-peen forming and other conventional forming techniques, CAF has a number of advantages over the former processes. These include (i) higher process repeatability as well as (ii) lower forming stress, (iii) lower residual stresses, (iv) better corrosion resistance and (v) better surface quality in the formed component (Islamoff, 1965; Holman, 1989; Zhan *et al.*, 2011a). One of CAF's greatest attributes is its (vi) independence from skilled operators, as opposed to the conventional forming processes where experienced operators are invaluable, making possible a high degree of process automation and better quality control (Holman, 1989). CAF is also (vii) less labour intensive and (viii) much more environmentally friendly than shot-peen forming which has a strong impact on the environment due to the generation of dust and noise (Eberl *et al.*, 2008). In addition, as a result of the concurrent material processing and panel shaping functionality of CAF, (ix) simpler processing routes (Figure 3) can be employed with CAF which leads to an overall lower manufacturing time and costs (Eberl *et al.*, 2006).

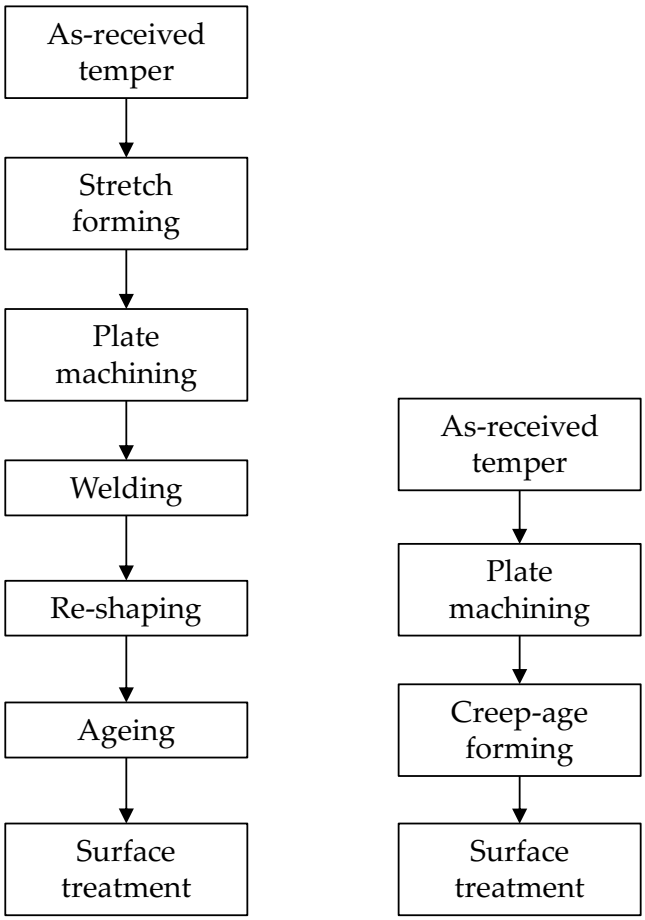

Figure 3. (a) A conventional processing route for manufacturing aircraft skin panels and (b) a simpler processing route with creep-age forming. Adapted from Eberl *et al.* (2006).

1.2. Description of a typical creep-age forming process

A typical CAF process can be split into three main steps and is illustrated in Figure 4.

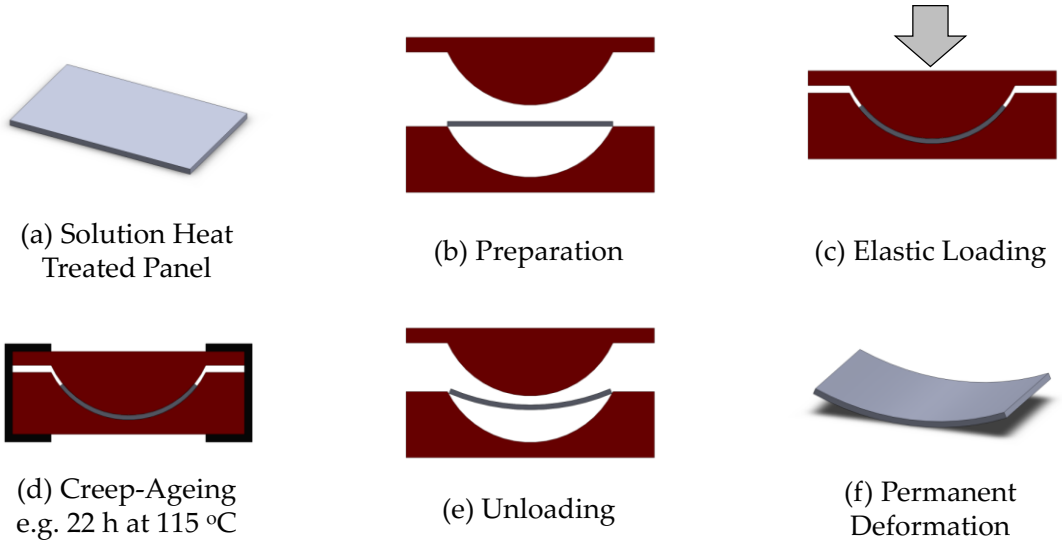

Figure 4. Schematics of a creep-age forming process.

The first step in CAF is workpiece preparation, where a solution heat-treated aluminium panel component is placed on a tool with thermocouples attached to the panel (Figure 4a and Figure 4b). The panel component is then loaded (Figure 4c).

Once fully loaded, the die is locked and the whole apparatus is placed inside an oven (Figure 4d) where the second creep-ageing step takes place. The oven applies a heat treatment cycle to both the panel and tool, whilst internal stresses in the panel, inducted by a combination of thermal reactions and constraint forces, relax. At the same time, constituent of the material precipitates due to ageing and alters the microstructure of the material, which results in a change in mechanical properties of the formed panel.

After the heat treatment cycle, the tool is submitted to the final unloading step. The tool is unloaded and the panel is allowed to springback (Figure 4e). As a result, permanent deformation is attained in the panel (Figure 4f). The amount of springback is determined by the amount of internal elastic stresses that remain in the panel immediately before unloading.

As the heat treatment cycle determines the final mechanical properties of the formed panel, the creep-ageing temperature and time are essentially process parameters that are unique to each alloy and cannot be altered to accommodate springback. This as a result makes springback inevitable and a major problem in CAF.

1.3. Development of techniques for overcoming springback

Figure 5 shows the concepts of three springback elimination strategies. The common aim amongst elimination strategies is to achieve no springback in the formed part. Springback elimination can be achieved via the mechanical approach or by means of development of new materials. Due to the simplicity of the mechanical elimination approach, which can be achieved by increasing sheet tension during bending for example, it is an easily adaptable, economic and a flexible method for overcoming springback.

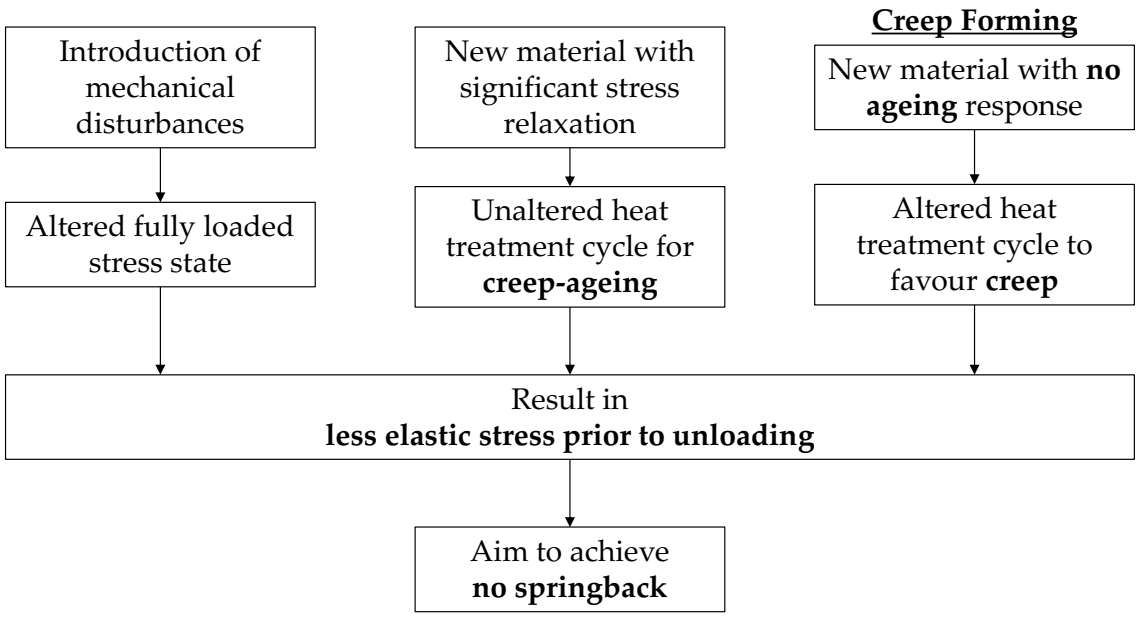

Figure 5. The concepts of three springback elimination strategies.

Although the mechanical approach promotes consistent response and is insensitive to process and material conditions, it is not suitable for forming operations where increased sheet tension may cause sheet fracture. Furthermore, the

unnecessary increase in forming stress is also undesirable as it can deteriorate formed part's quality.

The second elimination approach is the development of new materials that exhibit significant stress relaxation under the known creep-ageing conditions that the material will be submitted to during CAF. The newly devised material should undergo a significant amount of stress relaxation whilst its mechanical properties are changed under a controlled and predictable manner. This approach is feasible but is also theoretically challenging – it requires a huge amount of resources and man-months to achieve and is therefore not economic.

The third elimination approach has been employed by the Airbus Group in conjunction with the development of a patented material, the Scalmalloy®. Scalmalloy® is a naturally hardened Al-Mg-Sc alloy that the Airbus Group had developed specifically for creep forming. The patented Scalmalloy® material differs significantly from the conventional rolled Al-Mg-Sc alloys (e.g. the Russia RUS1570, Germany KO8242 and U.S.A. C557) (Leuschner *et al.*, 2010). In its original state, Scalmalloy® has high strength-to-weight ratio and exceptional fatigue properties, corrosion resistance and weldability for laser beam and friction stir welding. More importantly, it exhibits a highly stable microstructure under temperatures of up to 325 ^{o}C, which makes Scalmalloy® capable of fully relaxing its internal stresses without changes to the material's metallurgical and physical characteristics (ATL Technology Licensing, 2014). Its use therefore eliminates the need to consider changes in the material's mechanical properties during forming, thus the heat treatment cycle needs only to ensure internal stresses are fully relaxed to eliminate springback (Pacchione and Fideu, 2014). However, since no ageing occurs in the material during the creep process, it is no longer regarded as CAF but can instead be called creep forming. Similar to the second approach, this approach involves the development of new alloys and is very expensive to achieve.

An alternative to the elimination strategies is the compensation approach (Figure 6). Unlike the elimination strategies, the focus of the compensation approach is to achieve the target shape. The most widely adopted springback compensation method is known as the displacement adjustment (DA) method. Whilst the elimination strategies all focus on mechanisms to eliminate springback, the DA method provides an alternative by designing tooling in such a way to compensate for springback. That is, whilst springback may remain large, the final formed shape will still closely approximate that of the target shape after springback (Gan and Wagoner, 2004).

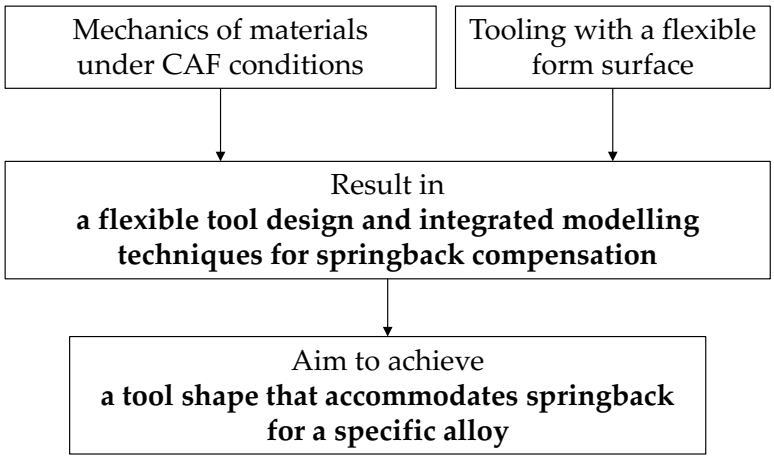

Figure 6. The concept of springback compensation.

The DA method is intuitive and simple to apply. The idea is to measure the form shape and calculate its distance from the target shape. The tool shape is then displaced by the same distance in the direction opposite to the springback deformation. The successful implementation of the springback compensation approach requires one to first be able to accurately predict springback of the panel. This must be based on a fundamental understanding of the mechanics of materials in conjunction with the use of flexible tooling.

1.4. Aim and approach

The ultimate aim that motivates this research is the development of the CAF technique to find a wider range of applications in the context of manufacturing of

extra-large panel components, targeting specifically at the transportation industry where components with high strength-to-weight ratios are crucial.

This thesis hypothesises that manufacturers in the transportation industry are already aware of the benefits of the CAF technique for forming extra-large integrally stiffened panels. However, there remains a technological gap to overcome springback in CAF which hinders its wider industrial application. Consequently, this thesis sets the goal to develop ad-hoc techniques to accurately shape panel components via CAF and to inform transportation equipment manufacturers about the developed techniques via example showcase studies. In order to achieve this goal, this research will be carried out by means of tooling design, experimentation and modelling and the following objectives will be met:

- To identify, through a critical review of the literature, key areas where the potential for further development exists to achieve springback compensation for industrial CAF.
- To study and quantify, through experimental and modelling work, the creep-ageing and springback behaviour of a typical aerospace-grade metallic alloy used in CAF.
- To design the associated equipment/tooling that will (i) allow the devised experimental and modelling work to be performed and evaluated, (ii) make possible springback compensation in CAF and (iii) have a scalable potential for real industrial use.
- To develop, based on the acquired understanding of the creep-ageing and springback behaviour of the metallic alloy, ad-hoc techniques for springback compensation in CAF by means of experimentation and modelling.
- To evaluate and summarise all the equipment/tooling and experimental and modelling techniques developed from this research by demonstrating their applications through example showcase studies.

1.5. Thesis organisation

Figure 7 illustrates a flowchart of the organisation of this thesis.

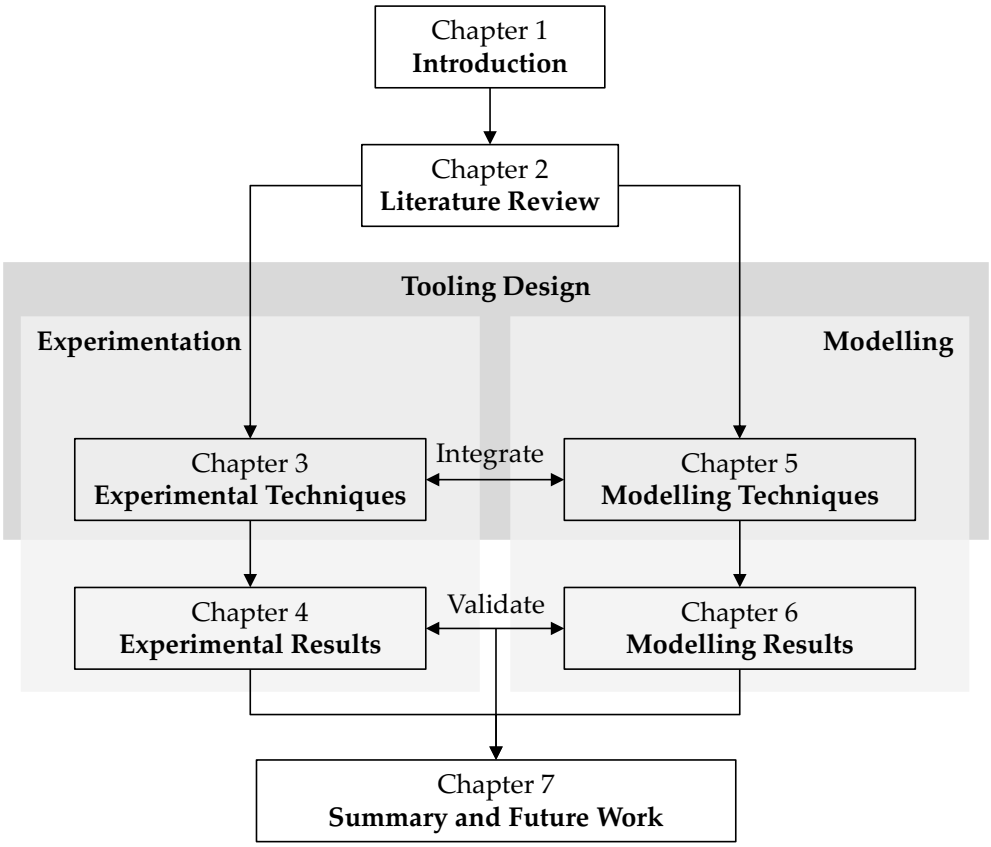

Figure 7. A flowchart of thesis organisation.

Chapter 1 provides an introduction and the general background and justification for this research. The aim and purpose of this thesis are discussed and the overall approach to this research is presented.

Chapter 2 reviews the relevant literature whose purpose was to better inform decision-making for the subsequent work and to define a specific research methodology for this thesis. Firstly, a general review of the creep-age forming technique is given which covers its applications, modelling technique and past experimental studies. Secondly, the mechanisms of springback, including factors that may affect springback, are reviewed in the broader context of sheet metal forming. Thirdly, reviews are given for tooling technologies and techniques that are associated with CAF and extra-large industrial fixtures. Lastly, conclusions are

drawn from the above reviews by identifying key areas where the potential for further development exists. Based on the conclusions, a specific research methodology is devised for this thesis and presented at the end of this chapter.

Chapter 3 details everything about the physical experimentation carried out in this thesis. A detailed description of the material investigated, the test programme used and the equipment and procedures involved in the tests are all contained in this chapter. A highlight description of the flexible form tool developed in this research is also given.

Chapter 4 presents and discusses the experimental results obtained from the material and forming tests. These include the creep-ageing behaviour of the material and its springback behaviour in creep-age forming.

Chapter 5 describes the material and process modelling techniques developed in this research. The first section details the procedures that were used to determine, implement and verify a material model for modelling creep-ageing response. The second section details the construction of an integrated process model in a step-by-step manner and also provides instructions for using it to perform process modelling and springback prediction.

Chapter 6 presents and discusses the modelling results obtained using the developed process model. The first section validates the ability of the process model to predict springback, by making shape comparisons between the experimental and modelling results to establish model accuracy. The second section showcases the research output from this thesis by applying all the tooling and experimental and modelling techniques developed in this thesis to produce accurately shaped components via CAF.

Chapter 7 summarises and discusses the outcomes of this thesis. The main contributions of this research are highlighted and suggestions are given to the possible areas of development for the continuation of this work.

CHAPTER 2.

LITERATURE REVIEW

2.1. Creep-age forming: applications, modelling and experimentation

To build a solid understanding of the state-of-the-art in the topic of CAF as a whole, this section provides a general review of the CAF technique covering its applications and the modelling and experimental techniques in the literature. This review is divided into three subsections; in the first subsection, the current applications of CAF are summarised and followed by a discussion of its potential applications. In the second subsection, current modelling techniques are categorised into material and process modelling activities with the purpose of each explained and the existing models discussed. In the last subsection, a review is given specifically for the past experimental investigations of springback in CAF.

2.1.1. Current and potential applications of creep-age forming

One of the earliest applications of CAF has been found in the production of integrally stiffened panels for launch vehicles. Figure 8 shows an expanded diagram of the Apollo/Saturn V launcher with its basic technical data presented on the right. The Saturn V moon rocket, first launched in 1967, was a multistage liquid-fuel expendable rocket used by NASA's Apollo and Skylab programs (Boeing, n.d.). With its first stage (also known as the S-IC) being 42 m tall and 10 m in diameter and

having five engines, the S-IC propellant tanks were amongst the largest such lightweight vessels ever built.

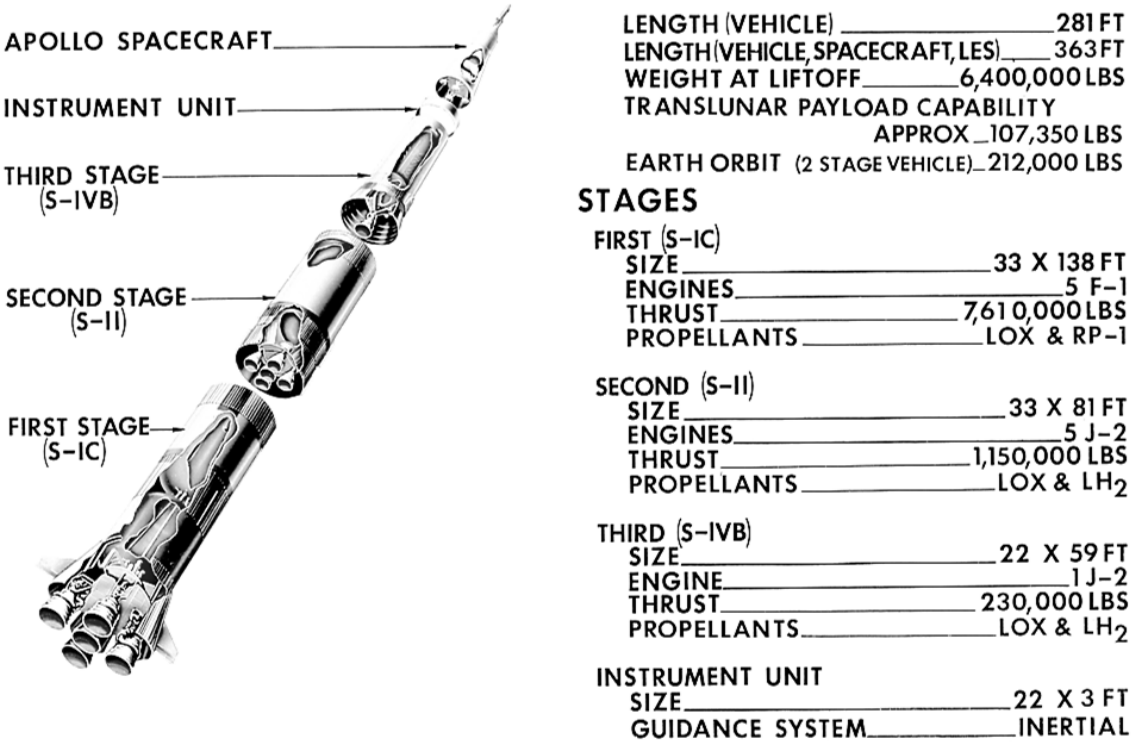

Figure 8. Schematic and characteristics of the Apollo/Saturn V launcher (MiX, 1971).

According to Bilstein (1980), Boeing had devised a technique for the production of the S-IC's integrally stiffened fuel and liquid oxygen tank skins. In such technique, AA2219 sheets of up to 27.6 square meters in size (with an aspect ratio of 3 : 8) and 57 mm thick, which simulated a full-scale quarter panel of Saturn V's S-IC propellant tank (Islamoff, 1965), were simultaneously age-hardened and formed in the same process inside an electric furnace.

Figure 9 shows the other possible applications of CAF for making structural components of launch vehicles. In order to make the pressure vessel of the SpaceX Dragon spacecraft shown in Figure 9, an initially flat aluminium stock was machined with triangular isogrid patterns (the integral stiffeners), curved into conic sections and finally welded into the vessel (SpaceX, 2010). Integrally stiffened isogrid panel constructions as such cannot be easily formed by conventional forming techniques and CAF had been proposed as a suitable technique by Holman (1989).

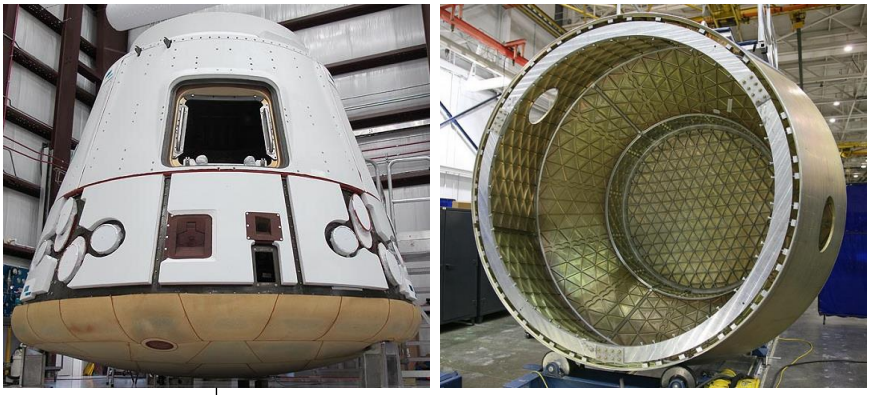

Spacecraft

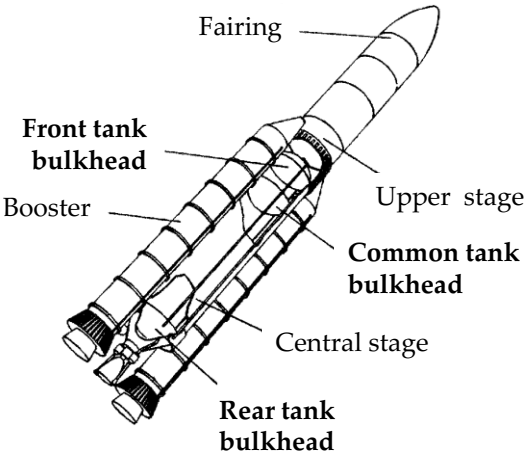

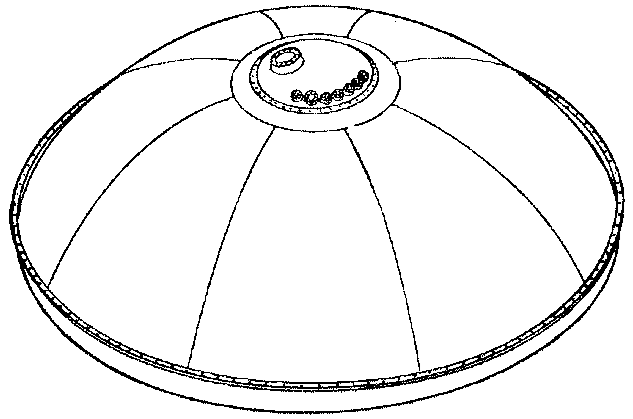

Schematic of a bulkhead

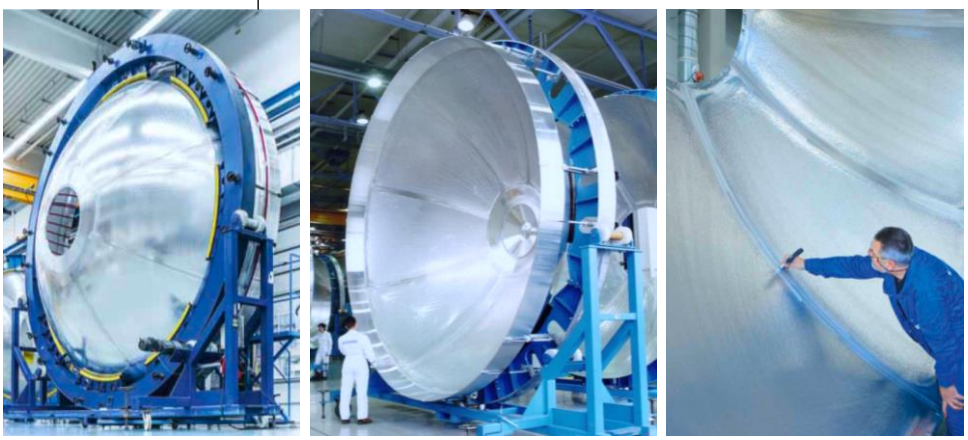

Bulkheads

Figure 9. Possible applications of creep-age forming in launch vehicles (Spacecraft – SpaceX, 2010; Ariane V launcher and bulkhead schematics – Wustefeld *et al.*, 1996; Ariane V's bulkheads – MT Aerospace, n.d. and Lo *et al.*, 2007).

Forming bulkheads of propellant tanks is another interesting area of exploration for CAF in launch vehicles. A typical launcher has three bulkheads – two of which close the cylindrical part of the launcher, front and rear, and the other is used to divide the oxygen from the hydrogen tank. Figure 9 shows several

photographs of the European Ariane V's bulkheads. A typical bulkhead of the Ariane V has a diameter of 5.4 m and consists of eight segments of AA2219 that have been peen formed (Friese *et al.*, 2006) and then welded together into complete domes for the fuel and liquid oxygen tanks.

In the past, different forming techniques such as spin forming and shot peen forming have been investigated for bulkhead production. Spin forming had been used to produce the bulkheads of Ariane IV. However, availability in sheet sizes limited its application for the larger bulkheads of Ariane V as no single sheets were available with a 6 m width. Attempts to first weld multiple sheets together and then submit the welded component to spin forming did not lead to success. This was due to failure of the weld before the necessary depth could be reached. Consequently, Dornier Flugzeugwerke, a defunct German aircraft manufacturer, investigated peen forming of gore panels and found significant advantages of the process (Hornauer and Kohler, 1990).

As previously mentioned, CAF has already been replacing peen forming for aircraft wing skin production. The adoption of CAF for bulkhead production may therefore also be possible. In fact, a series of bulkhead CAF simulation and optimisation studies were conducted by Bonnafe *et al.* (1996), Bourdin *et al.* (1999) and Kebir *et al.* (2000) of Aérospatiale (now part of the Airbus Group), and subsequent industrial CAF tests on bulkhead segments of Ariane V have shown results that correlate well with predictions. Though, actual evidence of using CAF for bulkhead production has not been found.

From the Boeing's B-1B bomber to the latest Airbus A380 Superjumbo and Dassault's Falcon 7X long range business jet, CAF has already been proven as a viable forming technique for aircraft's upper wing skin production. Despite the advantages that CAF has already demonstrated in aircraft upper wing skin production, it could not yet be used for other applications that require high damage tolerance (Borradaile, 1999). These include the bottom wing skins and fuselage

structures where 2000-series aluminium alloys (i.e. 2024A) in T3 (solution heat treated, cold worked and naturally aged to become substantially stable) condition were mainly used. As a result, the Ageform project was organised in 2002 in order to tackle such problems (Ageform, n.d.). With six project partners (Airbus UK, Alcan, Alenia, Dassault Aviation, Sabca and the University of Manchester) from four European countries, key results were realised within three years into the project and include the successful development of CAF for:

- integrally stiffened bottom wing skin of aircraft, and
- fuselage panel containing friction stir welded (FSW) panel-joints and laser beam welded (LBW) stringers (Eberl *et al.*, 2006).

Table 1 summarises the previous studies that have demonstrated either known or potential applications of CAF. The use of CAF for the production of aircraft wing skins is much better documented than the other spacecraft applications.

Table 1. A summary of the feasibility studies or applications documented for CAF.

First flight	Vehicle type	Make	Component	Reference
Nov 1967	Launch	Boeing Saturn V	S-IC Tank skins	Islamoff (1965); Bilstein (1980)
Dec 1974	Aircraft	Boeing B-1B	Upper and lower wing skins	Holman (1989)
Sep 1985	Aircraft	Gulfstream G-IV C20 F/G/H/J	Upper wing skins	Holman (1989) Lamartin (2004)
Oct 1991	Aircraft	Airbus A340	Upper wing skins	Holman (1989)
Nov 1992	Aircraft	Airbus A330	Upper wing skins	Holman (1989)
Nov 1995	Aircraft	Gulfstream G-V	Upper wing skins	Triumph Group (2010)
Jun 1996	Launch	MT Aerospace Ariane V	EPC Bulkheads	Bonnafe *et al.* (1996); Bourdin *et al.* (1999); Kebir *et al.* (2000)
Apr 2005	Aircraft	Airbus A380	Upper wing skins	Levers (2003); JRLZAGS03 (2009)
May 2005	Aircraft	Dassault Falcon 7X	Upper wing skins	ACARE (2010)

With a general trend of transport structures becoming larger in size and as a forming technique that is particularly suitable for the production of extra-large and integrally stiffened panels that contain FSW and LBW components, it is foreseeable that CAF has a potential to see wider applications in the future. Figure 10 illustrates the possible applications of CAF for making structural components of aircrafts.

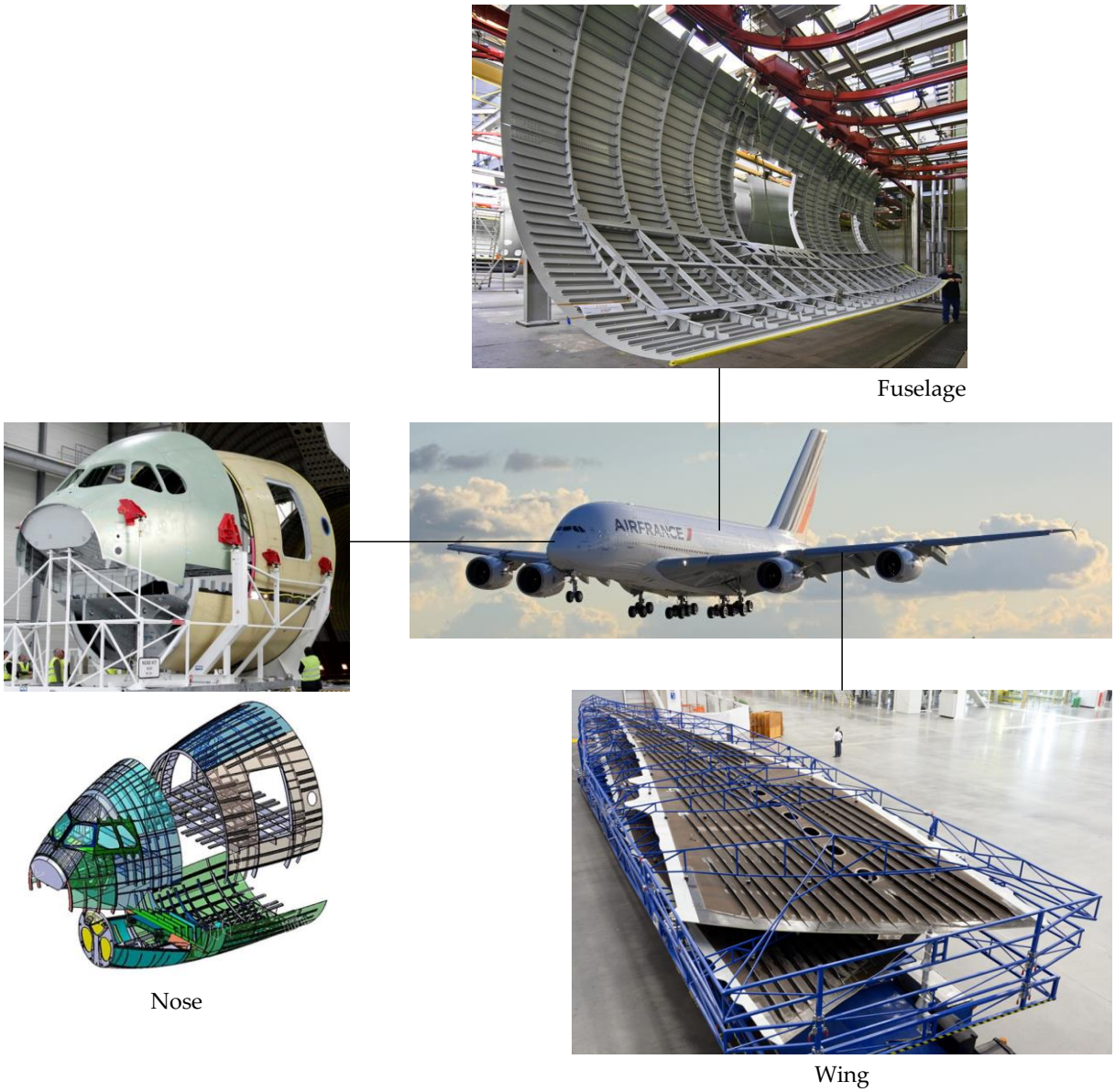

Figure 10. Possible applications of creep-age forming in aircrafts (Aircraft – Air France, 2011; Fuselage – Premium AEROTEC, n.d.; Nose – Flightglobal, 2011; Wing – Airbus, 2011).

CAF could possibly be used also for naval applications for the production of ship and submarine hulls. More specifically, it could potentially replace the light hull of double-hulled submarines, which is usually made of 2 to 4-mm-thick steel and

only intended to provide a more hydrodynamic shape for the submarine than the cylindrical inner pressure hull (Mahendra *et al.*, 2013). The congenital advantages of using aluminium to replace steel as the hull material include reductions in (i) operation cost, it saves over 20% of fuel per year of operation, and (ii) maintenance cost, as it eliminates the need for protective coatings in service (Austal, n.d.). For similar reasons, the application of CAF for the production of structural components of high-speed trains is also possible (Figure 11).

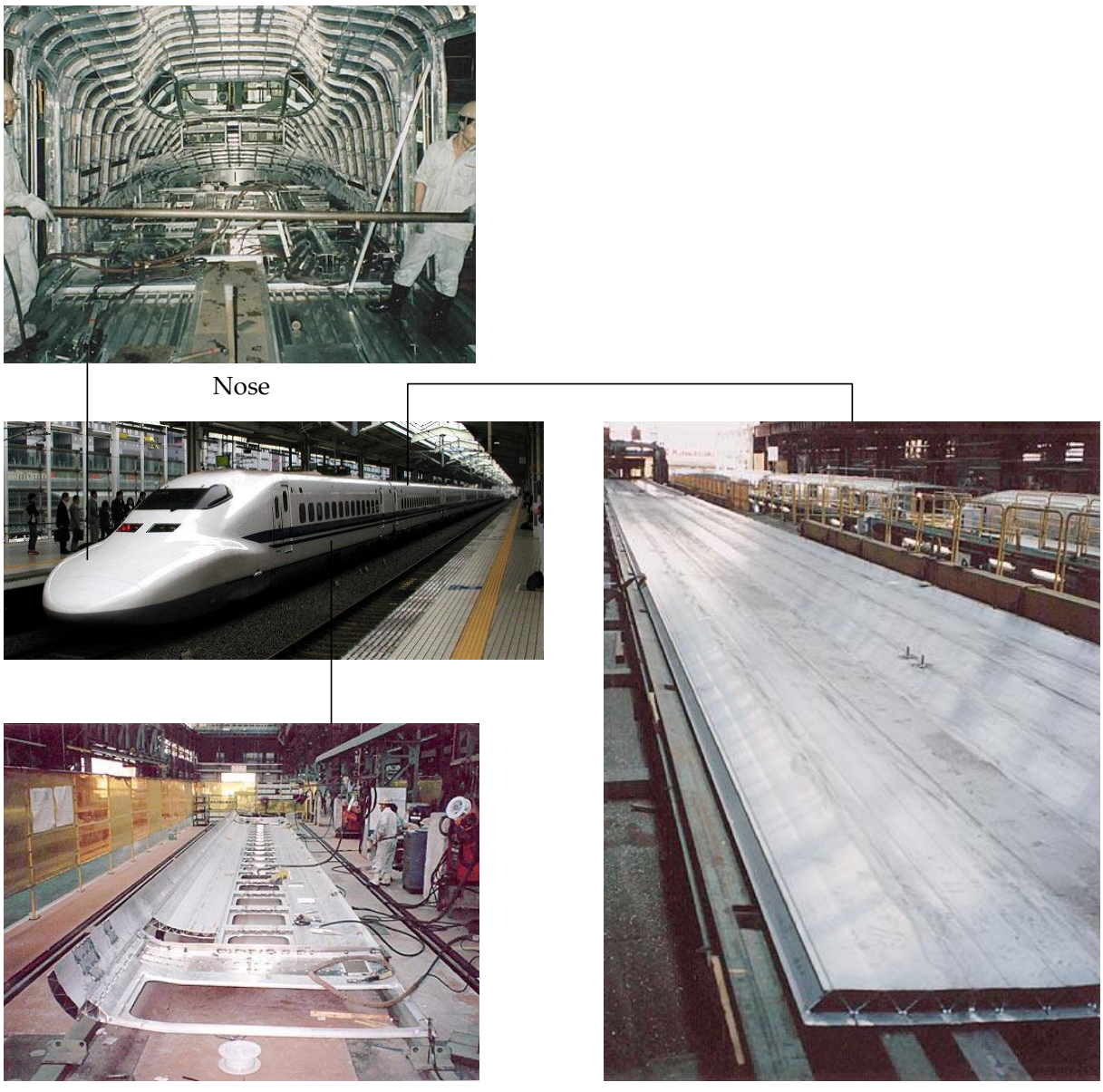

Figure 11. Possible applications of creep-age forming in high-speed trains (Train – JPRail, 2014; Nose, side and roof panels – Dranevitan, 2011).

2.1.2. Material and process modelling for creep-age forming

2.1.2.1. Material modelling

In CAF, the springback of components upon tooling release is unavoidable and presently challenges the art of form tool design for net-shape manufacturing. The need to control the mechanical properties of a part, which differs from one alloy composition to another with the way the part is loaded as well as the processing temperature and time, further complicates the problem. The purpose of material modelling for CAF is to enable accurate prediction of mechanical properties and the amount of springback upon tool unloading, so that parts can be manufactured to meet the required specifications.

(a) Classic stress relaxation/creep models

Sallah *et al.* (1991) analysed the autoclave age forming technique and the whole process was divided into three stages – loading, stress relaxation and springback. The loading and springback stages were treated as linearly elastic and an inelastic constitutive equation was used to model stress relaxation during the forming process:

$$\dot{\sigma} + F(\sigma, \varepsilon) = E\dot{\varepsilon} \tag{2.1}$$

with the superposed dots denote time differentiation. Two stress relaxation models were investigated:

$$\varepsilon_i = \sigma_i / E \tag{2.2}$$

and

$$\dot{\sigma} + F(\sigma, \sigma_i/E) = 0, \sigma(0) = \sigma_i \tag{2.3}$$

which are respectively a generalisation of the linear Maxwell model and an equation based on Walker/Wilson model. The model was applied to simulate forming on a cylindrical tool and a good agreement was obtained between experimental and simulation results.

Idem and Peddieson (2005) used a simplified one-dimensional version of the nonlinear Maxwell model for modelling stress relaxation:

$$\frac{dQ}{dT} + F(Q) = \frac{d\varepsilon}{dT} \tag{2.4}$$

where Q is the dimensionless axial tensile stress (normalised by the modulus of elasticity). Four different functions of $F(Q)$ were employed and were found to predict qualitatively similar stress-time curves having consistent shapes with experimental data. It was concluded that any realistic viscoelastic model could be used to simulate the ageing phase of age forming for any relaxation time. Thus a simple ageing function that has the same qualitative shape as the experimental data and the predictions of the nonlinear stress relaxation models was used. The specific working equation selected was:

$$Q_s = \begin{cases} aQ_t - bQ_t{}^2; Q_t < \frac{a}{2b} \\ \frac{a^2}{4b}; Q_t > \frac{a}{2b} \end{cases} \tag{2.5}$$

where Q_t and Q_s are respectively the stresses at time t and at the end of the relaxation period.

(b) Unified creep models

Continuum damage mechanism with three state variables was justified and used by Kowalewski *et al.* (1994) to model primary creep hardening and tertiary creep softening in an aluminium alloy. Hardening is due to dislocation at the initial stage of creep deformation. Softening is due to material ageing at high temperature and grain boundary cavity formation at tertiary creep. The equations in uniaxial form are:

$$\dot{\varepsilon} = \left[\frac{A}{(1-\omega_2)^n}\right] \sinh\left[\frac{B\sigma(1-H)}{1-\varphi}\right] \tag{2.6}$$

$$\dot{H} = \left(\frac{h}{\sigma_e}\right)\dot{\varepsilon}\left(\frac{1-H}{H^*}\right) \tag{2.7}$$

$$\dot{\varphi} = \frac{K_c}{3}(1-\varphi)^4 \tag{2.8}$$

where n is given as

$$n = \left[\frac{B\sigma_e(1-H)}{1-\varphi}\right] \coth \left[\frac{B\sigma_e(1-H)}{1-\varphi}\right] \quad (2.9)$$

Material parameters may be divided into three groups: (i) the constants h and H^* which describe primary creep; (ii) the parameters A and B which characterise secondary creep; and (iii) the parameters K and D responsible for damage evolution. The variable H describes primary creep and varies from 0 at the beginning of the creep process to H^*, the saturation value of H at the end of primary creep. Ho *et al.* (2004a) used the above equations for CAF springback simulation, where only primary and secondary creeps are considered. The damage, which is related only to tertiary creep, does not appear in the simulations. Thus only the first two equations were used. The constants within the constitutive equations were determined from experimental creep data of an aluminium alloy at 150°C under the stress levels of 241.3, 250.0, 262.0 and 275.0 MPa.

Similarly, Huang *et al.* (2007) noted the prospect to omit the damage terms during CAF and simplified the equations as follows:

$$\dot{\varepsilon}_c = A\sinh[B(\sigma - \sigma_0)(1-H)^{m_0}] \quad (2.10)$$

$$\dot{H} = \frac{h}{\sigma^{m_1}}\left(1 - \frac{H}{H^*}\right)\dot{\varepsilon}_c \quad (2.11)$$

where $\dot{\varepsilon}_c$ is the effective creep strain rate and σ the effective stress. Creep-ageing test of AA7B04 was conducted at 155°C and under stress levels of 240, 260, 280 and 300 MPa. Material constants were determined using genetic algorithm. The equations and material constants were then implemented in FE analysis with user-defined subroutine in Abaqus to predict springback.

(c) Physically based unified creep-ageing models

Ho *et al.* (2004b) developed a set of constitutive equation, which models primary and secondary stages of creep and precipitation nucleation and growth for a 7000-series aluminium alloy:

$$\dot{\varepsilon}_e = A\sinh\left\{B[(\sigma_e - \sigma_A)(1-H)]\left(\frac{C_{ss}}{\sigma_{ss}}\right)^n\right\} \tag{2.12}$$

$$\dot{H} = \frac{h_c}{{\sigma_e}^{0.1}}\left(1 - \frac{H}{H^*}\right)\dot{\varepsilon}_e \tag{2.13}$$

$$\dot{r}_p = C_0\left(Q - r_p\right)^{m_0}\left(1 + \left|\frac{\dot{\varepsilon}_e}{\gamma}\right|^{m_1}\right) \tag{2.14}$$

$$\sigma_A = C_A r_p^{m_2} \tag{2.15}$$

$$\sigma_{ss} = C_{ss}\left(1 + r_p\right)^{-m_3} \tag{2.16}$$

$$\sigma_y = \sigma_{ss} + \sigma_A \tag{2.17}$$

where A, B, h_c, H^*, n, Q, C_0, g, C_A, C_{ss}, m_0, m_1, m_2 and m_3 are material constants determined from creep-ageing experimental data using an evolutionary algorithm (EA)-based optimisation package. The basis of EA-based optimisation has been detailed by Li *et al.* (2002) and Lin and Yang (1999).

Eq. (2.12) describes evolution of the effective creep-ageing strain. Creep rate is not only a function of effective stress, σ_e, and dislocation hardening, H, but also of age (precipitation) hardening, σ_A, and solute hardening, σ_{ss}. The nucleation and growth of precipitates are related to the creep deformation (i.e., dynamic ageing). C_{ss}, σ_{ss} and n are responsible for softening of the matrix material due to particle coarsening.

Eq. (2.13) describes primary creep using variable H, which varies from 0 at the beginning of creep process to H^* where H^* is the saturation value at the end of the primary period, and subsequently, maintains this value for the remaining of the creep deformation.

Eq. (2.14) describes the evolution of the precipitate radius during isothermal ageing process. As the precipitates evolve or grow monotonically during isothermal ageing, the coarsening kinetic of the ageing mechanism can be modelled using a single precipitate radius growth equation, as proposed in the third equation. Because

CAF is a combination of creep deformation and age hardening, this equation includes the creep strain rate effect to describe the dynamic ageing behaviour.

The yield strength is the summation of solid solution hardening and age hardening. This set of constitutive equations was used to model creep-ageing of AA7010 at 150°C for 25 h. Very close agreement was achieved between the predicted and experimental creep-ageing strain at different stress levels.

Based on the experimental observations, Zhan *et al.* (2011b) formulated a set of mechanism-based unified creep-ageing constitutive equations, which models creep-induced evolution of precipitates, dislocation hardening, solid solution hardening and age hardening. In this model, the yield strength is derived from three sources: dislocation hardening, age hardening, and solid solution hardening. The constitutive equations are:

$$\dot{\varepsilon}_c = A_1 \sinh\{B_1[|\sigma|(1-\overline{\rho}_d) - k_{\varepsilon c}\sigma_y]\}\,\mathrm{sign}\{\sigma\} \tag{2.18}$$

$$\dot{\sigma}_{age} = C_a \dot{\overline{r}}_p^{\,m_1}(1-\overline{r}_p) \tag{2.19}$$

$$\dot{\sigma}_{sol} = C_s \dot{\overline{r}}_p^{\,m_2}(\overline{r}_p - 1) \tag{2.20}$$

$$\dot{\sigma}_{dis} = A_2 \cdot n_d \cdot \overline{\rho}_d^{\,n_d-1}\dot{\overline{\rho}}_d \tag{2.21}$$

$$\sigma_y = \sigma_{sol} + \sqrt{\sigma_{age}^2 + \sigma_{dis}^2} \tag{2.22}$$

$$\dot{\overline{r}}_p = C_r(Q_r - \overline{r}_p)^{m_3}(1 + \gamma_r \overline{\rho}_d^{\,m_4}) \tag{2.23}$$

$$\dot{\overline{\rho}}_d = A_3(1-\overline{\rho}_d)|\dot{\varepsilon}_c| - C_\rho \overline{\rho}_d^{\,m_5} \tag{2.24}$$

where the normalised precipitate size $\dot{\overline{r}}_p$ is defined as:

$$\dot{\overline{r}}_p = \frac{r_p}{r_{pc}} \tag{2.25}$$

where r_{pc} is the precipitate size at the peak-aged state, which considers the best match of precipitate size and spacing for the alloy. When $0 < \overline{r}_p < 1$, under-ageing exists; $\overline{r}_p = 1$, represents peak-ageing; and $\overline{r}_p > 1$ indicates over-ageing.

Eq. (2.18) shows that creep rate is not only a function of stress and dislocation density, but also a function of age hardening, solute hardening and dislocation hardening, which vary during CAF and together contribute to the yield strength.

Material constants were determined with CAF test results of AA7055 at 120 °C for 20 h. A multi-step fitting process was used to obtain the material constants efficiently: determine material constants (a) related to normalised precipitate size using yield strength under stress-free condition, (b) related to yield strength using yield strength under different stress condition, (c) related to creep strain rate according to initial and minimum creep rate at different stress levels and (d) finally re-evaluate and optimise all predetermined constants. Using this procedure, material constants were determined and the numerical results agree well with the experiments.

Li *et al.* (2010) developed a unified constitutive model for creep-ageing of 7B04 aluminium alloy, which takes into account the size, shape and volume fraction of precipitates. A fixed value of aspect ratio was assumed for the platelet precipitates. The constitutive equations are:

$$\dot{\varepsilon}_c = A\sinh\left\{B(\sigma-\sigma_0)(1-H_c)^{m_0}\left(1-\frac{\sigma_{ss}}{\sigma_{ppt}}\right)^k\right\} \tag{2.26}$$

$$\dot{H}_c = \frac{h}{\sigma^{m_1}}\left(1-\frac{H_c}{H_c^*}\right)\dot{\varepsilon}_c \tag{2.27}$$

$$\dot{H}_r = C_r(1-H_r)\varepsilon_c^{n_0} \tag{2.28}$$

$$\dot{L} = \left(C_k + C_0 H_r^{w_4}\right)L^{-1} \tag{2.29}$$

$$\dot{f}_r = \frac{2\pi L^3}{q} R N_0 Z\left(1-\frac{f_r}{f_r^*}\right)^{n_2}\varepsilon_c^{n_3} \tag{2.30}$$

$$\sigma_{ppt} = C_2 r^{m_2-1} f_r^{1/2} \tag{2.31}$$

$$\sigma_{ss} = C_{ss}(1-f_r)^{n_4} \tag{2.32}$$

$$\sigma_y = \sigma_{ppt} + \sigma_{ss} + \sigma_l \tag{2.33}$$

The growth of precipitates in fourth equation contains two terms: one for the effect of the ageing temperature and the other the creep strain. The change in yield strength is the result of age hardening and solid solution hardening. The parameters were obtained by EA to fit the experiment curve. Simulation results were in agreement with experimental knowledge at different stress levels.

Zhang *et al.* (2013a) investigated creep-ageing of aluminium alloys containing plate or rod-shaped precipitates. They introduced microstructural parameters such as volume fraction, characteristic size and aspect ratio, which evolve during creep-ageing, into the constitutive equations. The hardening mechanisms include solute hardening, age hardening and dislocation hardening, and the yield strength is a simple sum of these contributions and intrinsic strength of the matrix. In addition, temperature parameter was included in the formulation. The proposed constitutive equations are:

$$\dot{\varepsilon}_c = A\sinh\left(\frac{B\sigma}{\sigma_y}\right)^n \exp\left(-\frac{Q}{RT}\right) \tag{2.34}$$

$$\dot{\bar{f}}_v = \frac{C_1 l^{n_1} \dot{l}}{q^{n_2}}\left(1-\bar{f}_v\right)^{m_1} \tag{2.35}$$

$$\dot{l} = C_2(Q_1 - l)^{m_2}\left(1 + k_1 \bar{\rho}_m^{n_3}\dot{\rho}_m\right)\exp\left(-\frac{Q_2}{RT}\right) \tag{2.36}$$

$$\dot{\bar{\rho}}_m = C_3(Q_3 - \bar{\rho}_m)\dot{\varepsilon}_c \tag{2.37}$$

$$q = \frac{C_4}{\exp[k_2(T-T^*)^2 + k_3(t-t^*)^2]} \tag{2.38}$$

$$\sigma_{ss} = C_{ss}\left(1-\bar{f}_v\right)^{m_3} \tag{2.39}$$

$$\sigma_{ppt} = C_{ppt}\left(q\bar{f}_v\right)^{n_4} l^{n_5} \tag{2.40}$$

$$\sigma_{dis} = C_{dis}\bar{\rho}_m^{1/2} \tag{2.41}$$

$$\sigma_y = \sigma_0 + \sigma_{ss} + \sigma_{ppt} + \sigma_{dis} \tag{2.42}$$

Hot-rolled plates of AA2124 were used for creep-ageing and microstructural examination. The results were then used to determine the material constants, with an

optimisation software package based on universal global optimisation (UGO) and EA. A "step-by-step solution" was adopted and the material constants were determined in sequence for those related to (a) precipitate size, (b) aspect ratio of precipitates, (d) relative volume fraction, (d) yield strength and (e) all remaining constants. Figure 12 shows their modelling results agree well with experimental ones between the stress levels of 192 to 265 MPa under 453 and 463 K.

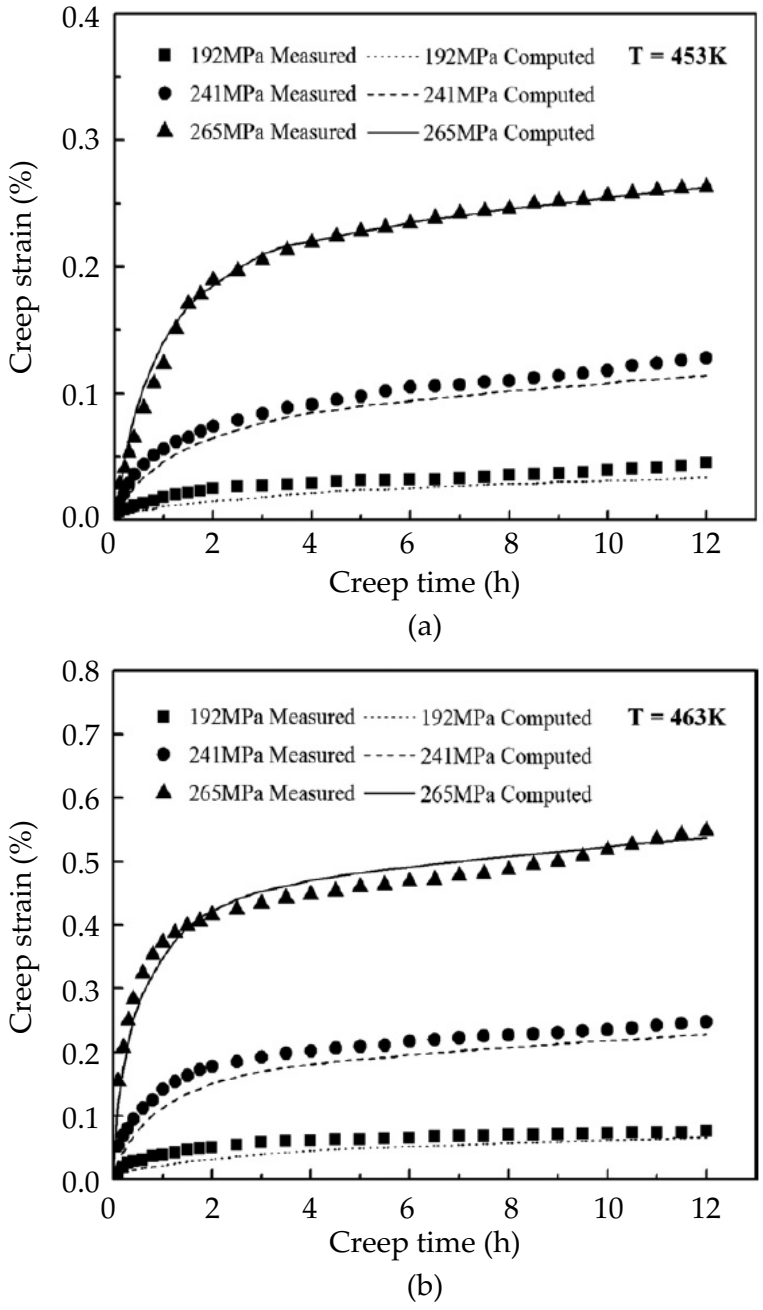

Figure 12. Comparisons of predicted and measured creep-ageing curves of AA2124 under different stress levels at (a) 453K and (b) 463K. Adapted from Zhang *et al.* (2013a).

(d) Aluminium alloys with determined material constants

Table 2 summarises the different aluminium alloys that have had their creep or creep-ageing material constants determined for different constitutive models by various researchers. Under the 'Prior treatment' column, SHT & Q refers to solution heat-treated and quenched with the alloy designation given in the brackets. (n.s.) refers to alloy designation not specified in the referenced work. C and CA refer to creep and creep-ageing models respectively. The creep/creep-ageing temperature and time under which the material constants were determined is given under the 'Condition' column with the final column referencing the researchers who performed the work.

Table 2. A summary of the aluminium alloys with their creep or creep-ageing material constants determined for modelling CAF.

AA	Prior treatment	Model	Condition	Reference
2124	SHT & Q (n.s.) SHT & Q (n.s.)	C CA	185 °C, 12 h 180 °C, 12 h 190 °C, 12 h	Zhan *et al.* (2012) Zhang *et al.* (2013a) Zhang *et al.* (2013a)
2219	SHT & Q (T4)	CA	175 °C, 18 h	Yang (2013)
2324	SHT & Q and cold worked (T39)	C	190 °C, 25 h	Huang *et al.* (2009a)
6056	(n.s.)	C	175 °C, 6 h 193 °C, 13 h	Guines *et al.* (2008)
7010	SHT & Q, and stretched (W51)	CA	150 °C, 24 h	Ho *et al.* (2004b)
7055	SHT & Q (n.s.)	CA	120 °C, 20 h	Zhan *et al.* (2011b)
7075	(n.s.)	C	163 °C, 24 h	Peddieson and Buchanan (1990); Sallah *et al.* (1991)
7B04	SHT & Q, stretched and artificially aged (T7451)	CA	150 °C, 15 h	Li *et al.* (2010)

2.1.2.2. Process modelling for creep-age forming

With the material model fully determined, CAF process modelling then enables manufacturers to assess the material behaviour under multiple CAF scenarios (such as the use of different tooling and lubrication condition) through computer simulation, thereby reaching the most cost-effective way of producing a part whilst avoiding the high cost of physical trials. Being able to predict various scenario

outcomes consequently enables manufacturers to produce good quality component first-time-right and thus reduce the associated costs.

In the past, fundamental studies in CAF process modelling have been based on analytical and empirical methods. These methods contain a large number of assumptions adapted from the classic Euler-Bernoulli beam or Kirchhoff-Love plate theories. The limitations of these models commonly include pure bending assumption, radius of curvature dependent analysis, unable to predict mechanical properties evolution and the effects of thermal-friction interactions are often neglected (Peddieson and Buchanan, 1990; Sallah *et al.*, 1991; Idem and Peddieson, 2005; Jeunechamps *et al.*, 2006; Inforzato *et al.*, 2012; Lam and Lin, 2014). As a result, these studies have usually been found only to help establish theoretical understanding in the topic or applied to small-scale laboratory studies where complex tool geometry and mechanical properties evolution of the part need not be considered.

On the other hand, the growing demand in modelling more complex forming operations combined with the rapid reduction in computational costs have made the use of numerical methods widely accessible by researchers. Finite element (FE) method in particular, has become a popular tool in sheet metal forming analysis. The development of FE models with validated predictive ability can provide a cost-effective alternative to costly experimental setups and make possible the simulation of multiple scenarios (such as tooling design, blank material, heating temperature and time) by simply altering modelling input. The versatility of the method also allows for material nonlinearities to be introduced, rendering it a highly attractive method amongst studies that look into capturing the nonlinear creep-ageing behaviour of aluminium alloys in CAF.

Ho *et al.* (2004a) are one of the pioneers in the field who utilise FE analysis to perform modelling of the forming process. Although ageing behaviour of the aluminium alloy was not yet involved, this work has laid an important foundation

on the stress relaxation behaviour and the effects of forming time, sheet thickness and double curvature forming surface on springback in sheet metal forming processes that utilise creep as a mean to introduce permanent deformation.

Lin *et al.* (2006) later developed an FE process model that was integrated with a set of physically-based, unified creep-ageing constitutive equations for AA7010. Using their technique, the paper has demonstrated the possibility of concurrently modelling precipitate growth, yield strength evolution and creep deformation during CAF.

Flat plates were mostly used in the early research where the main focus was on the development of fundamental understanding of creep and creep-ageing behaviour of aluminium alloys in CAF. Guines *et al.* (2008) numerically modelled the CAF of a singly curved integrally stiffened panel in order to evaluate the influence of different mechanical boundary conditions on stiffened structures. Hardening, thermal softening, and stress relaxation effects of the stiffened panel have been considered in their model. Their results show that it is possible to minimise springback by making an appropriate choice of boundary conditions. Further experimental studies were suggested to be performed by the authors to establish reliability of the modelling method they proposed.

Modelling research on stiffened component continued with the work of Inforzato *et al.* (2012) who adapted a semi-empirical model for CAF springback estimation of AA7475 stiffened panel. The simplified model, which is based on classical plate bending theory combined with the concept of equivalent height, requires calibration using experimentally measured deflections. A 600 mm × 300 mm AA7475 plate was flat-machined down from a 50.8-mm-thick plate to an integrally stiffened panel with a 5-mm-thick base and eleven height-varying blade stiffeners. CAF of the stiffened component was carried out using a vacuum bagging technique for load application. The calculated radii of the creep-age formed part ranged from

820 to 2600 mm and the calibrated model was able to provide springback estimations to an accuracy of within ±1.3%.

Upon identifying the two major load cases commonly used in CAF for research and industrial purposes, Yang *et al.* (2013) developed a number of numerical models to analyse the effect of an end clamp (research laboratory) and uniform pressure (industrial manufacturing) loading cases on springback prediction using FE. The study found that given a sufficient loading pressure, contact between CAF tool and workpiece surfaces can be better established by uniform pressure loading than end clamp loading. Furthermore, a significantly different local springback distributions of components formed via the two different load cases was observed. As a result, a suggestion was made that the springback measured from components formed using a laboratory end clamp device should not be used to compare with those formed using a vacuum forming device.

Utilising the AA2219 CAF material model determined by Yang (2013), Lam *et al.* (2015a) investigated the effect of different stiffener designs and pre-form age conditions on CAF of AA2219 plates. Integrally stiffened AA2219 plates were studied on an end clamp device with the introduction of PTFE fillers to protect stiffeners during forming. Using the corresponding FE models to investigate multiple CAF scenarios, pre-form age condition was found to have effects on both the peak stress levels of plates during CAF operations and their springback. Moreover, when bending stiffeners were present, the highest stress level was found more likely to occur within and around those stiffeners. Bending stiffeners may therefore be seen as a form of stress shields for the base plates and take up a greater proportion of the creep strain in CAF.

2.1.3. Experimental investigations of springback in creep-age forming

Despite the growing use of numerical methods such as FE analysis, the role of experimental investigation is still significant to CAF research. In particular, the use

of experimental results to validate model predictions remains a standard practice to establishing the springback predictive ability of newly developed models.

In order to reduce manufacturing cost and weight of aircraft wings, Adachi *et al.* (2004) investigated the potential of applying CAF to form doubly curved skin panels with variable thickness and established a method to predict their springback. Integrally stiffened AA7475-T7351 skin panels of 1000-mm-long and 400-mm-wide were creep-age formed on doubly curved tools that have chord and span curvatures that range from 800 to 4000 mm and 8000 to 48000 mm respectively. All specimens were formed successfully with springback ranged from 51 to 67% in the chord direction and 54 to 70% in the span direction. The formed components have shown no buckling on the stringers and excellent repeatability was achieved for each tool.

Huang *et al.* (2009b) conducted CAF experiments on artificially aged AA2324 to investigate the effects of thickness, elastic deformation, ageing time and temperature on formed part radius of curvature and mechanical properties. A regression equation was established with the four factors taken into consideration which provides useful guidance for the optimisation of CAF process parameters and springback prediction.

Zhang *et al.* (2013b) compared the influences of the CAF of AA2124 on single and double curvature tools. Springback was found to have been influenced by ageing condition and related to the internal stress state of material. In particular, a minimum springback value could be achieved with them in an optimal coupling state. Specimens formed on a double curvature tool appeared to have higher yield strength, ultimate tensile strength and fracture toughness than those formed on a single curvature tool under the same ageing condition.

Using a combination of experimental and FE modelling techniques, Lam *et al.* (2015a) investigated the mechanics of CAF of AA2219 integrally stiffened plates on an end clamp device that has a mean single curvature of 153 mm. PTFE pocket fillers

have been introduced as a novel technique to protect the stiffeners of the 48 by 200 mm plates. Defect-free parts have been formed successfully with smooth curvature.

Zhan *et al.* (2014) designed a series of tests to investigate the combined effects of ageing temperature, ageing time, pre-deformation and part thickness on the springback of creep-age formed AA2524 sheets. Two springback prediction models were developed based on experimental results and multiple linear regressions. The models' ability to predict springback was justified by the close agreement achieved between predicted and experimental data. It was found that the compression side of formed parts possesses more and finer precipitates than the tension side of the same part, resulting in better mechanical performance in the compression side.

Due to the long processing hours required for creep forming processes, such techniques are most often found economic only to be used to manufacture extra-large components. Levers (2008a) disclosed an invention that could improve related forming operations by shortening the manufacturing time. The disclosed technique utilises the combined application of static and cyclic loading to the component during a creep forming process. The application of cyclic loading was claimed to be able to act as an additional energy source during creep forming, which could accelerate stress relaxation and therefore achieve the same amount of deformation in less time, effectively reducing the time required to manufacture a component. The magnitude of cyclic loading was preferred to be less than or equal to at most 10% of that of the static loading.

A recent work by Wang *et al.* (2014) further investigated the effects of introducing vibration to CAF on AA7055. Their results show that under the same amount of creep-ageing time, the rate of stress relaxation was faster with vibration introduced, which agrees with those disclosed by Levers (2008a). In addition, more finely dispersed precipitates have been observed in specimens formed with vibrational energy input. Comparing specimens formed under conventional CAF

conditions and those formed under vibrational CAF conditions, specimens from the latter tests have shown 7% greater strength and 12.3% lower springback.

2.2. Springback of forming metallic panel components

It is essential to fully understand the mechanisms behind the phenomenon of springback in order to develop an accurate model and modelling procedure for springback prediction. Firstly, the major factors that affect springback are demonstrated with the aid of a simple analytical model. The subsequent subsections are then presented to emphasise the importance of the adequate use of modelling parameters and numerical procedure for accurate FE analysis of springback.

2.2.1. Mechanisms of springback

Metallic panel components, such as stiffened and non-stiffened metal sheets and plates, are amongst the most frequently used semi-finished products across manufacturing industries. The various forming techniques for shaping metallic panel components all involve permanently deforming blanks that has a high surface-area-to-thickness-ratio into a target shape. Figure 13a and Figure 13b show an initially flat blank is first placed on a forming tool and then deformed by closure of the forming tool. As the forming tool is unloaded, the component emerges and tends to revert to its original shape–a phenomenon known as springback (Figure 13c).

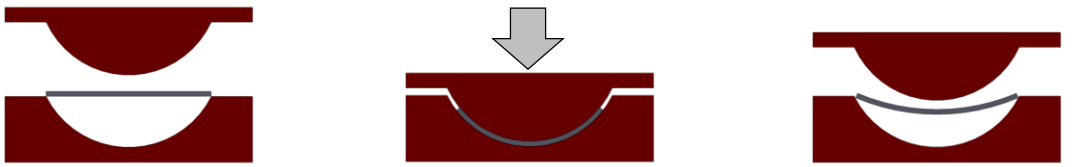

(a) An initially flat blank

(d) Deformed in a forming tool

(c) Unload of tool and springback of the blank

Figure 13. Schematic of a typical metallic panel component forming operation.

The mechanism of springback has been examined by Marciniak *et al.* (2002) using a simple case and is revisited here. Consider a sheet metal part that is bent under a pure bending moment M (Figure 14). The length of its mid-surface is

$$l = R\theta \tag{2.43}$$

where R is the bending radius and θ the bend angle. The length, l, will remain unchanged during unloading as the stress and strain are always zero at the middle surface. Rearranging Eq. (2.43) gives

$$\theta = l\frac{1}{R} \tag{2.44}$$

and differentiating with l treated as a constant

$$\frac{\Delta\theta}{\theta} = \frac{\Delta(1/R)}{1/R} \tag{2.45}$$

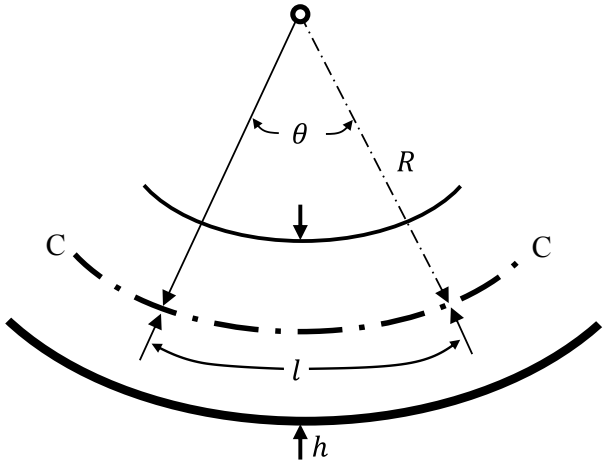

Figure 14. A sheet metal part bent under pure bending moment. The plate centroid is indicated by the line C-C.

Assuming an elastic, perfectly plastic material undergoing an elastic unloading process, the classic bending equation can be written in difference form, such that

$$\frac{\Delta M}{I} = \frac{\Delta\sigma_x}{y} = \frac{E\prime}{\Delta R} \tag{2.46}$$

where ΔM is the change in bending moment, $I = h^3/12$ is the second moment of area for a unit width of sheet, $\Delta\sigma_x$ is the change in stress of the fibre at a distance y from the neutral axis at the mid-thickness and $E' = E/(1-v^2)$ applies for plane strain bending with E being the Young's modulus and v the Poisson's ratio.

With a sheet that has been bent to the fully plastic moment M_p, the unloading curve will be parallel to the elastic loading line which suggests

$$\frac{\Delta(1/R)}{(1/R)_e} = \frac{\Delta M}{M_e} = \frac{-M_p}{M_e} \tag{2.47}$$

where $(1/R)_e$ is the elastic bending curvature and M_e is the elastic bending moment. Therefore

$$\Delta\left(\frac{1}{R}\right) = -\frac{M_p}{M_e}\left(\frac{1}{R}\right)_e = -3\frac{\sigma_y}{E'h} \tag{2.48}$$

If the sheet has been unloaded from a curvature of $(1/R)_0$, the proportional change in curvature is

$$\frac{\Delta(1/R)}{(1/R)_0} = \frac{-3\frac{\sigma_y}{E'h}}{(1/R)_0} = -3\frac{\sigma_y}{E'}\frac{R_0}{h} \tag{2.49}$$

or, according to Eq. (2.45), its change in bend angle is

$$\Delta\theta \approx -3\frac{\sigma_y}{E'}\frac{R_0}{h}\theta \tag{2.50}$$

This equation is only an approximation and applies to small differences in angle or curvature and to the case in which the sheet has been fully plastically deformed. Nonetheless, Eq. (2.50) is very useful for indicating the mechanisms of springback, which is related to

- material behaviour – yield strength (σ_y), Young's modulus (E) and Poisson's ratio (v) of the sheet material,
- bend ratio – the ratio between bend radius (R_0) and sheet thickness (h), and
- bend angle (θ).

2.2.2. Springback sensitivity to material and process parameters

Eq. (2.50) from the above-illustrated example shows that springback can be affected by variables such as material properties (σ_y, E and v), specimen design (h) and forming tool design (R_0 and θ). Under warm forming conditions, the springback of panel components is also sensitive to additional material and process parameters. Using a thermo-mechanically coupled FE model that is capable of simulating a simple draw-bending process, Kim and Koç (2008) performed numerical

investigations on the springback characteristics of AA5754-O sheet metal parts under warm forming conditions. Upon validating the reliability of the FE model by comparing the numerical results with experimental measurements available in the literature at room temperature, the following were found:

- Taking into account the **thermally-induced distortion** of the forming tool by modelling it using a 3D deformable mesh led to some difference in the amount of springback than if the tool were treated as 2D rigid bodies. However, the significant amount of time saving achieved by using 2D rigid bodies to model the tool (120 *vs.* 3 h) had led them to perform the investigations with 2D rigid bodies.
- The amount of springback was significantly reduced by increasing forming temperatures to above 200 ^{o}C. This was due to a **decrease in material's strength at elevated temperature**, which led to an improved formability of the part.
- The dimensional accuracy of the formed part was improved as a result of **modelling the elevated temperature condition** in warm forming.
- Increasing the level of **blank holder force** and **frictions** could help to reduce the amount of springback. This was attributed to the less bending moment required for a given curvature when greater tension force is experienced by the blank.
- The influence of forming rate on springback could be observed at temperatures above 200 ^{o}C due to an increase in **strain rate sensitivity with increasing temperature**.
- Using a **temperature-dependent value of Young's modulus** could improve the accuracy of their numerical results.

2.2.3. Springback sensitivity to numerical methods

Although a versatile numerical method widely used by many for the simulation of sheet metal forming processes, large modelling errors to the accuracy of springback prediction can still be encountered with the use of inappropriate modelling techniques. Narasimhan and Lovell (1999) studied the use of an explicit-to-implicit FE procedure to analyse the forming of an actual automotive component. The rationale behind the use of a coupled FE procedure was because explicit method is computationally efficient at solving large deformation and contact problems; whilst springback calculations are very expensive with respect to processing time in the explicit regime. Conversely, the implicit method is not well suited for nonlinear problems but highly cost-effective at handling the linear springback problem. In summary, the study found that:

- the **selection of appropriate boundary conditions** was a critical factor for obtaining robust and accurate springback solution. Symmetry boundary conditions should always be utilised to restrain rigid body motion where available,
- their numerical results, as validated by experimental measurements, indicate that the **use of shell elements** and the underlying assumptions within them, was able to reduce the overall computational time without degrading the predicted springback results, and
- the **explicit-to-implicit coupled FE procedure** was able to achieve good springback predictive accuracy at low computational cost.

The increase in the use of shell elements for springback simulations had soon led the **number of through-thickness integration points (N_{IP})** required for accurate springback analysis to become a subject of confusion and controversy. Wagoner and Li (2007) addressed the contradictions at the time using an analytical model of elasto-plastic bending under tension, followed by elastic springback. By comparing

the fractional error in springback obtained from three numerical integration schemes with various N_{IP} to the closed-form result, the numerical integration errors were found to be oscillatory in nature with small parametric changes. The authors further concluded that no single integration always performs the best; and in general, the effective use of N_{IP} varies with bend ratio, sheet tension, constraint and the confidence limit required. However, Gauss integration was suggested for problems with high tension force where the integration errors tend to be largest.

Burchitz (2008) carried out an extensive investigation into the improvement of numerical prediction of the springback phenomenon in sheet metal forming. The large topic encompasses the effects of material behaviour, contact scheme, element type, unloading method, time integration scheme as well as blank and tool discretisation error on springback prediction. In addition to the important points that have also been raised by the previous researchers, the author further suggested the following for accurate FE analysis of springback:

- **Appropriate use of constitutive laws** that accurately represent the material behaviour during a deformation. For accurate springback prediction, a material model that takes into account the inelastic effects that occurs during unloading may be required.
- The numerical model must **reflect the physical contact conditions** that exist throughout the forming process. As the component is unloaded after forming, contact forces present between the tools and the blank. It was shown that those forces can influence the amount of springback of the blank and must not be neglected.
- Minimising the **discretisation error of blank and tool** is equally important for accurate springback prediction. It was shown that using less than ten blank and tool elements in a curved regions results in an inaccurate prediction of the stress state immediately before the component is unloaded.

2.3. Tooling technologies for extra-large components

One of the objectives of this research is to deliver the necessary CAF equipment/tooling that can be used in this research, which enables springback compensation and have a scalable potential for real industrial use. This section first gives a summary of the tooling requirements that drive successful forming tool designs in the industry. Existing tooling concepts and designs applicable to extra-large components and CAF are then analysed. Lastly, a review is given which provides the rationale behind the need to address the latest issues in designing flexible CAF tools for extra-large components.

2.3.1. Tooling requirements for creep-age forming extra-large components

A list of the tooling requirements that outline the characteristics of successful CAF tool designs is given below with explanations:

- **Low tool manufacturing costs –** The tool should utilise as many standard parts, and as few part variations, as possible to keep the initial cost of tool manufacturing low.
- **Low tool maintenance costs –** In cases where individual parts of the tool get damaged, or required replacement due to wear, part replacement cost should be kept low.
- **Eliminates the need for having a unique forming tool for each new shape required –** The use of universal tooling eliminates the need for having a unique forming tool for each shape required. Lead time can be reduced and the maintenance and manufacturing costs associated to the production of an additional tool can also be eliminated as a result.
- **Reduce overall manufacturing costs for the production of extra-large panel –** The potential to reduce setup time as well as associated labour and/or computational costs by minimising the efforts required to rectify physical tool shapes.

- **Lightweight** – CAF requires frequent transportation of tooling and the tool design must adopt a lightweight structure that is designed specifically for CAF.

2.3.2. Existing fixtures for handling extra-large components

A review on the structural design of existing fixtures for handling extra-large components is useful to inspire industrial design techniques for large size equipment and forming tools. Figure 15 shows the preparation of a Gulfstream G650 wing skin on a check fixture for peen forming. An overhead crane is a typical equipment for lifting and transporting extra-large panel components (Figure 15a). Fixtures for extra-large components typically consist of multiple chord wise rib boards arranged in the span direction. Such structural arrangement is effective in providing sufficient support to the component and at the same time minimising the use of building material.

(a)

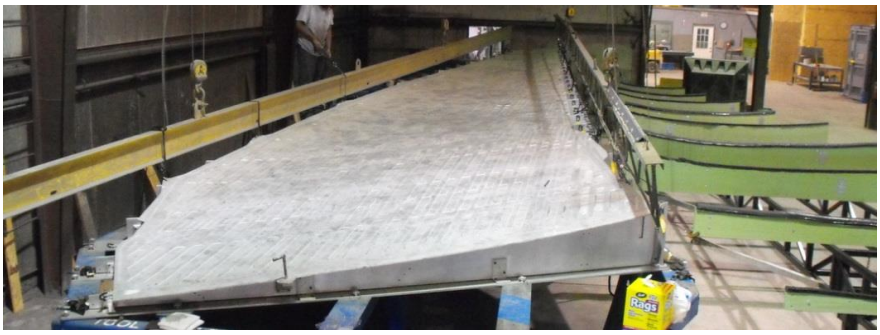

(b)

Figure 15. Preparation of a Gulfstream G650 wing skin on a check fixture for peen forming (National Shot Peening, n.d.). (a) Wing lifted by an overhead crane. (b) Wing placed on the fixture.

Figure 16 shows another wing skin test fixture designed by Robert Moulton for Boeing. The structural design of this fixture largely resembles that of the wing box of an aeroplane. This check fixture is used to verify the contour of formed aluminium wing skin panels. In a typical inspection process, the skin panel is first lowered by an overhead crane and placed on the check fixture. In order for the wing skin panel to past the inspection test, the panel must be bent to within 0.055 inches (approximately 1.4 mm) to ensure it will not be overstressed when it is finally riveted to the substructure (Moulton, 1996).

(a)

(b)

Figure 16. Wing skin test fixture (Moulton, 1996). (a) View looking from the outboard tip of the wing towards the fuselage. (b) View similar to looking at an aircraft wing from inside through the aircraft window.

2.3.3. Existing creep-age forming tools

2.3.3.1. Simple research tools

Simple devices used to investigate different features of the CAF process have been discussed by Zhan *et al.* (2011a). Figure 17 shows the four-point bending and cantilever bending tools that are commonly used in research laboratories. They have been popular in the research field due to their ease of operation and low cost to manufacture. They are also extremely lightweight, which makes the storage and handling of the devices easy.

Pure uniform bending moment seen in a four-point bending test enable experimental results to be acquired more easily compared to both the cantilever and three-point bending test. Nevertheless, more complex shapes such as the doubly curved surfaces frequently seen in practice cannot be reproduced by them.

Figure 17. Left: A four-point bending SSC test jigs (Caltech Engineering Services, 2012). Right: A cantilever bend test to examine the formability of aluminium (McMaster University, 2007).

Advantages
- Lightweight
- Cheap to manufacture
- Easy handling and maintenance

Disadvantages
- Cannot produce complex curvatures and shapes

2.3.3.2. Machined dies

This die group is characterised by die sets consisting of at least one solid die. A solid die is created by machining the exact profile of the loaded component into a solid block of rigid material. Figure 18 shows a single curvature machined die set. The tool

consists of a male upper die and a female lower die. During the loading stage of a typical CAF test, an aluminium sheet is first placed on the lower die. The upper die is then loaded and clamped by means of nuts and bolts.

The main disadvantage of this tool design is the difficulty in altering the shape of the solid die during the iterative process of springback compensation, in which a heavy die must be handled and located so that machining of a large area can be achieved. To obviate this problem, investigations have been undertaken into lightweight tool designs in which shape rectification of die shapes may be cheaply and quickly achieved.

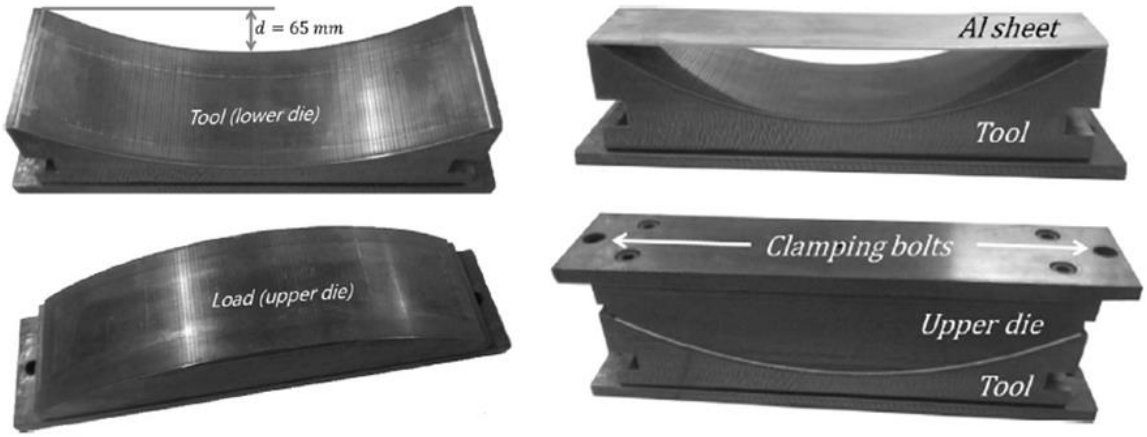

Figure 18. A single curvature machined die set (Jeshvaghani *et al.*, 2012).

Advantages
- Accurate and complex curved shapes may be achieved.

Disadvantages
- Heavy
- Springback compensation is cumbersome and expensive

2.3.3.3. Discrete elements

One of the first discrete element designs can be backdated to the invention by Hess (1931), who invented an apparatus that can manufacture foot supports for shoes up to anatomical accuracy. The concept of the design later blossomed into wider applications, and has been applied to the manufacture of sheet metals for other aerospace, biomedical and shipbuilding applications (Pinson, 1980; Ansted, 1982; Haas *et al.*, 1996; Nardiello *et al.*, 2000; Park *et al.*, 2000).

Figure 19 shows a prototype utilising discrete elements design concept for press-forming aerospace components. The continuous and rigid forming surface features of the machined die group have been replaced by the use of discrete elements in this concept of tool design. Discrete element tools generally have pins of heights that can be varied. The pins are arranged in a lattice form such that the relative height variations of the pins can be changed to form the target contour required for each forming operation. Although they do enable rapid springback compensation and are lighter than equivalent machined dies, they are more expensive to manufacture and assemble due to the multitude of parts. The increased number of parts also means that a lengthy adjustment process is required. Most often, they also lack the structural integrity to withstand high compressive loads.

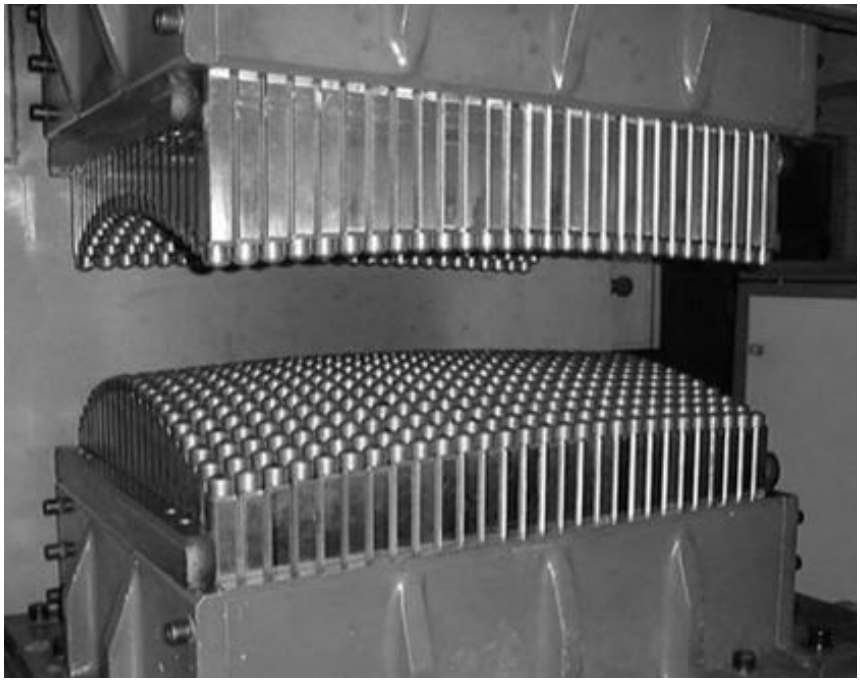

Figure 19. A multipoint forming prototype for aerospace press-forming (SAE International, 2008).

Advantages

- Easy to change die shape
- Potential weight reduction

Disadvantages

- Expensive to manufacture
- Lengthy adjustment process
- Lack of structural integrity to withstand high compressive loads

2.3.3.4. Rib boards with vacuum bagging

The state-of-the-art rib boards design developed by Andrew Levers (Levers, 2003; Levers, 2008b; Levers, 2010) for Airbus quickly proved its value by meeting a number of key requirements. Figure 20a shows an isometric view of the tool, which makes use of two horizontal guide rails that are rigidly bolted on to a base (not illustrated). N_m pairs of vertical guide rails are firmly supported by the horizontal guide rails and can slide only in the x_2 direction. Once slid to the required x_2, each pair of vertical guide rails are bolted to the horizontal guide rails, thus are structurally supported by both the horizontal guide rails and the base. The vertical guide rails from this instance onwards are firmly fixed in position. The i^{th} and $(i+1)^{th}$ pairs of vertical guide rails are now spaced d_j apart in the x_2 direction, where $i = 1,2,3,\ldots,N_m$ and $j = 1,2,3,\ldots,(N_m - 1)$ for a tool with N_m modules.

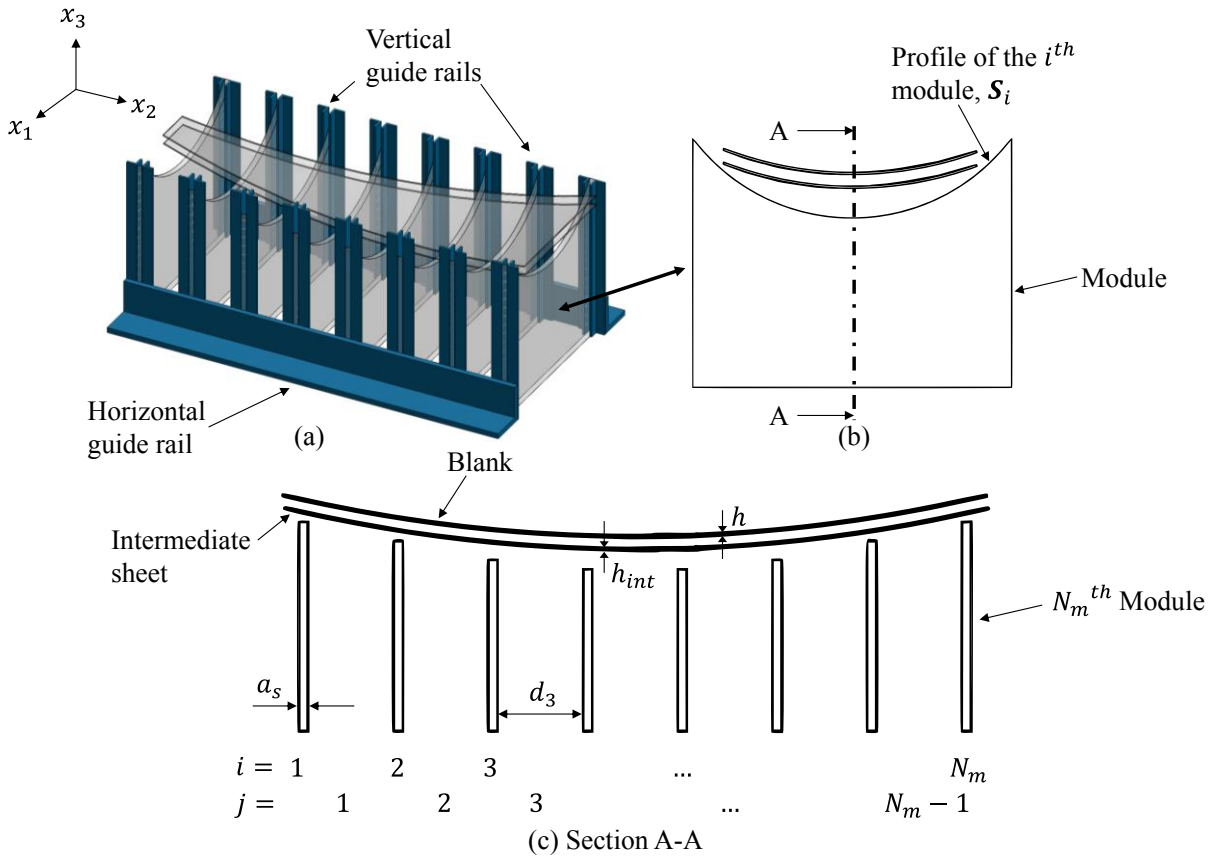

Figure 20. Schematics of a 1D-modularised CAF tool showing (a) an isometric view of the tool, (b) a single module, and (c) view on cross-section A-A (Lam *et al.*, 2015b).

With reference to Figure 20b, the i^{th} module, which is a metal sheet with a profile described by $\boldsymbol{S}_i$, is chosen for each pair of vertical guide rails. Once positioned, each module is firmly bolted to the vertical guide rails. Each of $\boldsymbol{S}_i$ contains a 2D point cloud in the x_1x_3 plane and is chosen so that, when all modules are positioned at the correct x_2, deflection surface of the uniformly loaded intermediate sheet, placed on top of all modules, will form the shape of the required forming surface within pre-defined tolerances.

The positioned modules of thickness a_s, topped by the intermediate sheet and blank, are shown in Figure 20c. This is a generic tool design such that modules with various profiles can be mounted to the vertical guide rails. The modules, vertical and horizontal guide rails and the base, which all together form a rigid supporting structure, are made of tooling steel that are substantially stiff and undergo negligible deformation during a CAF process.

Although a flexible tool, the major shortcoming of the rib boards design is also its flexibility. Whilst the tool is flexible in x_2, aerofoil of the wing panel that is to be formed remains determined by the shape, $\boldsymbol{S}$, that is machined into each module. This means for every new wing design, or any adjustments that are required for springback compensation, a new set of modules must be made. This makes any shape-rectifying process essential for springback compensation lengthy and costly. Bespoke autoclave and associated equipment are also required for creep forming large panels. This device tends to be the limiting factor with respect to the capacity of the manufacturing process to produce a given number of components per month.

Advantages

- Lightweight
- Better flexibility than solid dies

Disadvantages

- Less flexibility than discrete element tools
- Lengthy and costly shape-rectifying process
- Require the use of bespoke autoclave equipment which are expensive and limits the capacity of manufacturing process

2.3.4. Flexible creep-age forming tools for extra-large components

Levers has disclosed a tool that has been designed by utilising rib boards with shaped profiles to form a modular base structure to replace the need for a conventional solid bottom die. These rib boards with shaped profiles act as supports for the intermediate sheet that is topped by the wing skin during forming operations.

As the wing skin is vacuum loaded, the intermediate sheet deforms together with the wing skin towards the shaped profiles. They then begin to conform to the shaped profiles until the maximum vacuum pressure is reached. At such point, the intermediate member and the wing skin both take on a surface which shape is defined by the mechanics of plate bending (Figure 21).

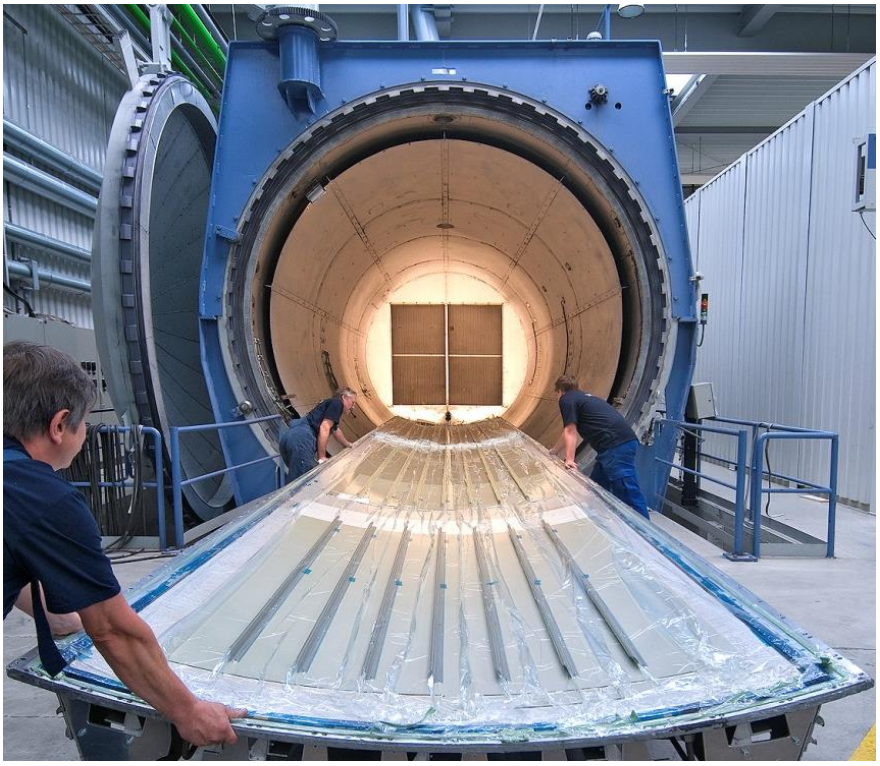

Figure 21. Airbus A380 glare shell goes to the heat treatment process in an autoclave (Premium AEROTEC, n.d.).

Due to the requirement for the forming surfaces to be machined into the rib boards, Levers' tool cannot be used to form wing skin of different shapes unless a new set of rib boards are manufactured for every new wing design. Li *et al.* (2013) disclosed an alternative design which utilises arrays of discretised punch elements as

bottom dies. These bottom punch elements are height-adjustable whilst loading is again achieved by vacuum pressure. Therefore, it is possible to manufacture wing skin components of different shapes using this single tooling.

The tools described above share common disadvantages - Vacuum pressure loading is not always sufficient for full contact between the wing skin and the desired forming surfaces to be achieved. Fully loaded shape of the wing skin cannot always be accurately predicted as a result, and can introduce great uncertainties to the prediction of springback. Moreover, the formable shapes of these tools are limited by a number of factors that are difficult to control. Such as the maximum pressure that can be generated by the vacuum pump, and the ability for the same loading pressure to be maintained throughout the entire creep-ageing period, which may take up to a day (24 h).

Tooling such as those disclosed by Li *et al.* (2013) is very heavy in weight due to the high number of part-count and are unfavourable to CAF processes which require frequent transportation of the tool. Fixed positions of the pins also pose certain limitations on the tool – for example, they can only be used together with the vacuum bagging technique, or otherwise, integrally stiffened panels with certain stiffener designs cannot be formed using such tools. This is because the stiffeners must not be in the way of the pins when the wing skin is being loaded to the required shape. As a result, the use of multipoint tools with pins' positions being fixed will require the wing designer's understanding of the tool's limitations, in order to design wing skin components that can be formed using the tool.

2.4. Conclusions and research methodology

This section discusses the conclusions that can be drawn from the literature review and identifies the potential areas for further development. By aligning these conclusions to the objectives of this work, a research methodology is devised for this thesis and presented at the end.

2.4.1. Material and process modelling techniques

The classic stress relaxation/creep models consider only conventional high temperature stress relaxation/creep that occur(s) under CAF conditions without the consideration of hardening. For the unified creep models, hardening is implicitly contained in the formulation for primary creep stage. Main efforts have been made to calibrate either stress relaxation or simple creep models from experimental data, so that springback can be predicted. However, they do not contain information on microstructural features and the interaction between creep deformation and age hardening. Nevertheless, the equations were determined from experimental data of creep or stress relaxation under ageing conditions, the effect of age hardening was already embedded in the determined constants. Therefore, these models can be used to predict springback in CAF simulation.

The mechanism-based models consider some or all of the major contributing factors to yield strength during CAF. These factors include solid solution hardening, dislocation hardening and age hardening. To predict age hardening, evolution of microstructural features, such as precipitate size, aspect ratio and volume fraction need to be modelled. The mechanism-based models reviewed all consider the interaction of creep deformation and age hardening in one way or another, which provide better insights into the material's behaviour during CAF. These models are able to predict the mechanical properties evolution of the material such as the evolution of yield strength, microstructural features of precipitates and dislocation density.

CAF process models have evolved from the use of simpler empirical or analytical models that requires many assumptions to the use of FE modelling techniques for the ever-growing complexity of new forming operations. Integrated modelling techniques in particular, enable the concurrent simulation of creep deformation and mechanical properties evolution and thus are particularly well-suited for modelling CAF operations.

2.4.2. Experimental techniques

Most physical experiments and their corresponding process models have been developed to better understand the fundamentals of CAF and the process. Single curvature CAF tests on flat panels were amongst the most frequently performed experiments for model validation and recent studies have shown a trend towards investigations of integrally stiffened panel parts. Although CAF is used mainly for the production of doubly curved panel parts in the industry, double curvature CAF tests have remained at the simulation level in the literature. This is partly due to the high cost involved in producing multiple tooling to experiment with the springback feature of panel parts under various degrees of double curvatures in CAF condition.

The majority of the CAF experiments have been carried out on 2000 and 7000-series aluminium alloys. A typical CAF test can be split into three stages: loading, creep-ageing and unloading. In most cases, an experiment begins with attaching thermocouples to the panel part that is to be formed. The part is then loaded on a former, locked at its loaded configuration and put into an oven/a furnace where creep-ageing takes place. At this stage, temperature readings from the thermocouples are used to maintain the creep-ageing temperature at the target level. After a predetermined period of creep-ageing time, the panel part is cooled to room temperature and unloaded. Typically, the panel part will spring back by over 80% with a large radius of curvature, up to 48000 mm, remaining in the formed part.

CAF suffers from the disadvantage of long processing hours required to manufacture a component. Latest research efforts have begun to seek to shorten the manufacturing time for creep forming processes by introducing vibrational energy as a mean to accelerate the mechanisms of stress relaxation and precipitation. Preliminary research results have so far reported the real potential of this technique and the amount of research activities in this field is currently low.

2.4.3. Tooling technologies for creep-age forming extra-large components

Table 3 summarises all the existing CAF tools with the tooling requirements, listed and explained in Section 2.3.1, that they meet.

Table 3. Tooling requirements for creep-age forming extra-large components against existing creep-age forming tool designs.

	Simple research devices	Machined dies	Discrete elements	Rib boards with vacuum bagging
Low tool manufacturing costs	●	●	●	
Low tool maintenance costs	●		●	●
Universal tooling for complex shapes			●	
Low cost for extra-large components				●
Lightweight	●			●

Simple research devices are not scalable for industrial use and have less shape complexity but are the most competitive by cost and weight. This is the reason why they have been very popular amongst researchers carrying out basic investigations of the CAF process. Conventional tools with machined dies cost very little to make, are very robust and can be used to form shapes with complex curvatures. However, they are expensive in the long term when it comes to maintenance and tool shape modification for springback compensation. It is also unrealistic to make them to a dimensionally large scale for forming extra-large components due to their weight. The conventional discrete element tools are able to form more complex shapes than simple research devices and have greater flexibility than solid machined dies. They have drawbacks such as the high number of pins, which leads to their heavy weight and the greater setup time required. Modular rib board structures are commonly employed as an industrial design technique for handling extra-large components. They often utilise the mechanical stiffness of the supported component itself as a mean to minimise the use of tooling material and structure but without

compromising the structural support given to the component. The state-of-the-art rib boards forming tool has adapted such technique in its structural design and combined it with the use of vacuum bagging to provide the forming load. Although the rib boards forming tool can be an expensive equipment to purchase at first, due to the need of using high-temperature vacuum equipment, its design reduces weight significantly. Its industrial scalability is proven and maintenance cost is low due to the use of standard parts. However, it is not universal as changing tool shapes require every time machining the exact shape profile into the modules.

The need for flexible tools is on one hand driven by the high cost of tooling for forming extra-large components, and on the other hand driven by the need to compensate for springback in CAF. During the lifecycle of a metallic airframe, iterative updates to the product may also see the adoption of new and improved alloys, which could mean re-manufacture of the tooling. Designing a CAF tool that meets all of the listed requirements is therefore a big challenge and remains a current technology gap that could be exploited in this research.

2.4.4. Research methodology

A critical review of the state-of-the-art in CAF, springback mechanisms and the latest tooling technologies applicable to CAF enables the formulation of a specific methodology for achieving the research objectives. Figure 22 shows a flowchart of the research methodology set out for this thesis.

This research is split into two main phases that are interconnected, namely (i) research and development and (ii) application. In the first step of the research and development phase, an aerospace-grade aluminium alloy will be selected with its creep-ageing condition determined. The alloy will be tested for its creep-ageing behaviour under the predetermined condition. The material test data will be used to establish a physically based unified creep-ageing material model for this alloy under the given CAF condition. Research will be carried out to propose new forming equipment and tooling that have the required features to close the existing

technology gap in CAF tool design. A laboratory-scale tool will be delivered and in conjunction with the material model, will together serve as inputs for the development of an FE process model for CAF.

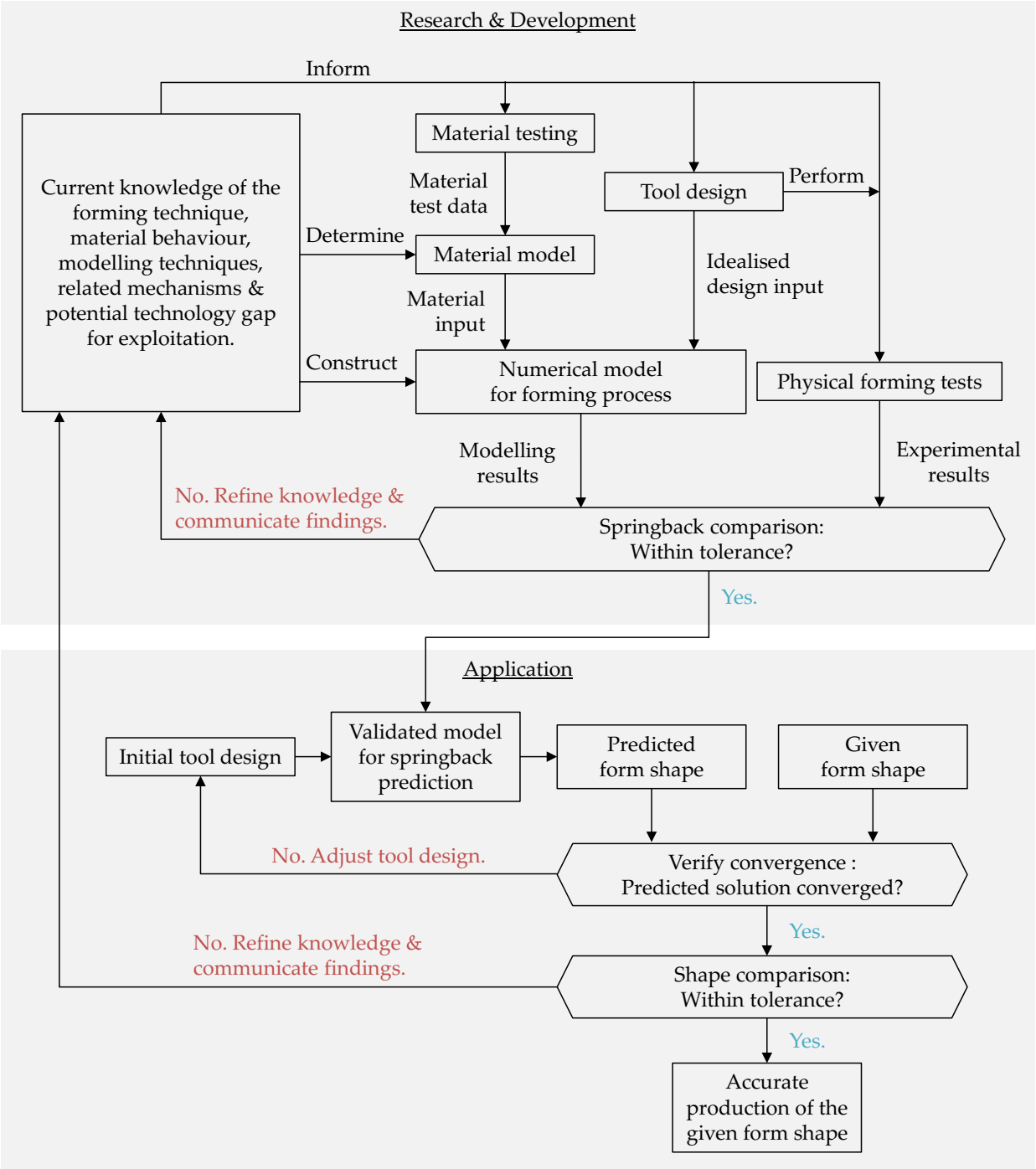

Figure 22. A flowchart of the research methodology.

The forming tool will also be used to perform physical CAF tests on the alloy and the results of which will be used to validate the springback predictive ability of

the developed process model. A failure to accurately predict springback using the FE model at this point will reflect the need for further refinement of the existing knowledge (the literature). This may be in terms of material testing, material and process modelling techniques, experimental techniques or tooling design method, or some or all of the above. This will be through carrying out further research into the specific topic required. New findings from these research activities will be disseminated through publishing journal articles and conference papers and presenting at conferences, workshops and seminars. Potential intellectual property will be protected by various means such as by filing a patent if required.

The outcome of the iterative research and development process will lead to an FE model that has a springback predictive ability that satisfies the required tolerance. The validated FE model will be applied in an iterative process of modelling springback-compensated tool designs. A convergent solution from the springback compensation process but with the shape outside the shape tolerance will indicate the potential need for reinvestigations to further refine existing knowledge in the field. Otherwise, a convergent solution with the shape also within the shape tolerance will indicate a true success of this research.

CHAPTER 3.

EXPERIMENTAL TECHNIQUES

3.1. Introduction

This chapter summarises all the equipment details and experimental techniques involved in this research. Figure 23 provides an overview of the layout of this chapter.

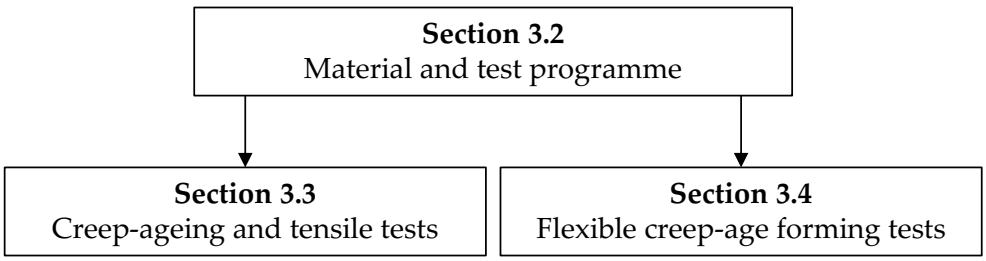

Figure 23. An overview of the layout of Chapter 3.

Firstly in Section 3.2, details about the material investigated in this thesis are provided and a test programme is presented. The test programme consists of two test plans detailing the scope of all the tests performed in this research: (i) the creep-ageing and tensile tests and (ii) flexible CAF tests. The individual test details of (i) and (ii), including descriptions of the test specimens, test equipment and experimental procedures, are given in Sections 3.3 and 3.4 respectively.

3.2. Material and test programme

3.2.1. Material

The material investigated in this research is aluminium alloy 7B04 whose chemical composition is presented in Table 4. The alloy is investigated in its longitudinal rolling orientation throughout this research.

Table 4. Chemical composition (wt%) of 7B04.

Zn	Mg	Cu	Mn	Fe	Cr	Si	Ni	Ti	Al
5.97	2.48	1.51	0.33	0.16	0.16	0.07	< 0.05	< 0.05	Bal.

Figure 24 illustrates the alloy's heat treatment history prior to receiving for investigation. The T651-tempered alloy was provided by the project sponsor, AVIC BAMTRI (Beijing, PR China), after solutionising at 475 °C for 1 h, 1.5% stretching for stress relief and artificial ageing at 115 °C for 24 h to stabilise the microstructure of the alloy.

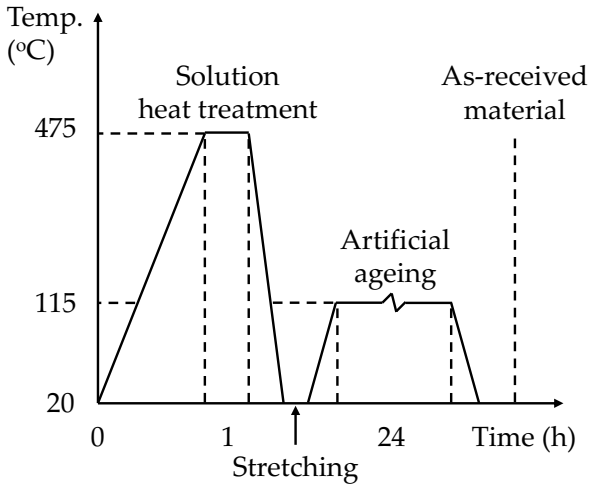

Figure 24. Heat treatment history of the as-received alloy.

The CAF thermal cycle investigated in this research was predetermined by the sponsor such that after this heat treatment, the alloy will reach the desired mechanical properties required by the sponsor for their specific application. This thermal cycle is defined by a creep-ageing temperature of 115 °C and a creep-ageing time of 22 h.

3.2.2. Test programme

3.2.2.1. Test plan for creep-ageing and tensile tests

Interrupted creep-ageing tests and uniaxial tensile tests were performed in order for the creep-ageing behaviour and yield strength evolutions of 7B04 to be determined. Figure 25 illustrates the thermal cycle of the tests, which were performed by Ms Xia Huang, an academic visitor of AVIC BAMTRI, as part of the project collaboration.

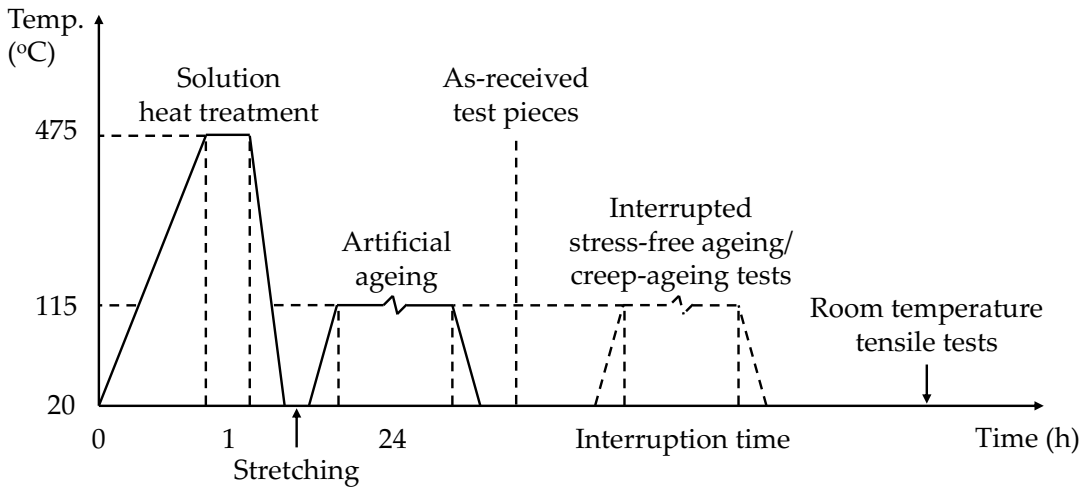

Figure 25. Thermal cycle of the creep-aging and tensile tests.

Table 5 presents the test plan used for the creep-ageing and tensile tests. The applied stress levels and interruption time for the tests are summarised. The tabulated range of test conditions was chosen by compromising between the loading stress levels specified by the sponsor and the number of test pieces available. The stress-free-ageing tests were carried out in a furnace and details about the creep-ageing and tensile tests, including the test piece design, equipment used and the experimental procedures followed, are given in Section 3.3.

Table 5. Test plan for the creep-ageing and tensile tests.

Stress level (MPa)	Interruption time (h)	Number of test pieces
0	0, 2, 5, 8, 10, 15, 18, 23	8
200	22	1
240	0, 6, 14, 22	4
260	22	1
280	0, 6, 14, 22	3
Total number of test pieces		17

In addition, samples of the as-received alloy and those that had received a further 22 h of stress-free-ageing were sent to an external laboratory for transmission electron microscopy (TEM) analysis. The alloy's precipitate growth over the 22 h of stress-free-ageing was expected from the TEM analysis result.

3.2.2.2. Test plan for flexible creep-age forming tests

Flexible CAF tests were performed for model validation and springback compensation studies to be carried out. Figure 26 illustrates the thermal cycle of the CAF tests.

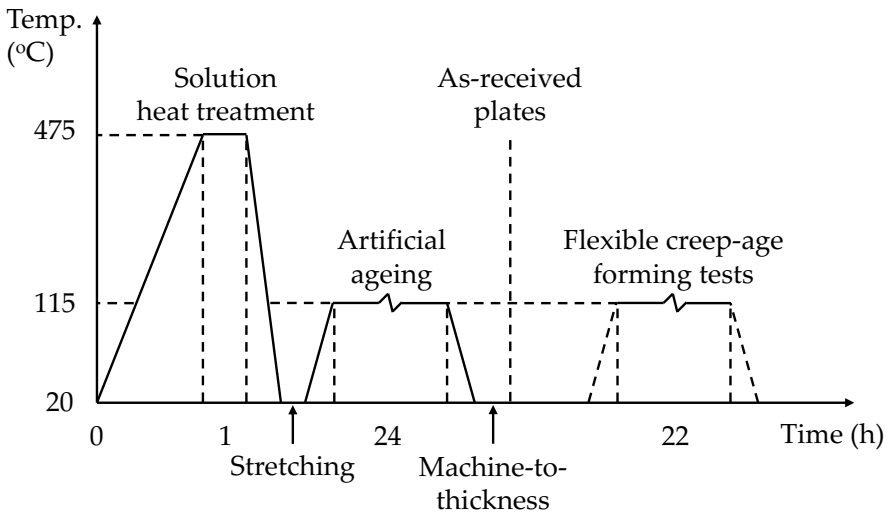

Figure 26. Thermal cycle of the creep-age forming tests.

Table 6 presents the test plan used for the CAF tests. Plates of 3 to 8 mm thicknesses are investigated in this research. Thrice-repeated single curvature CAF tests were performed for each plate thickness for process model validation. The subsequent springback compensation studies were based on one double curvature CAF test for each plate thickness.

Table 6. Test plan for the creep-age forming tests.

		Number of plates in thickness of		
Testing curvature	Purpose of tests	3 mm	5 mm	8 mm
Single	Validation	3	3	3
Double	Compensation	1	1	1
Total number of plates			12	

Decision on the form shape for the CAF tests took into account the mechanical properties and creep-ageing behaviour of 7B04-T651 as well as the physical limitation of the CAF tool. Details about the plate dimensions, CAF tool design, other equipment used and the experimental procedures followed for the flexible CAF tests are given in Section 3.4.

3.3. Creep-ageing and tensile tests

3.3.1. Test piece design

Creep-ageing and tensile test pieces of 7B04-T651 were provided by AVIC BAMTRI in the longitudinal rolling orientation. Figure 27 illustrates the geometry and key dimensions of the generic test piece design that was used for both tests.

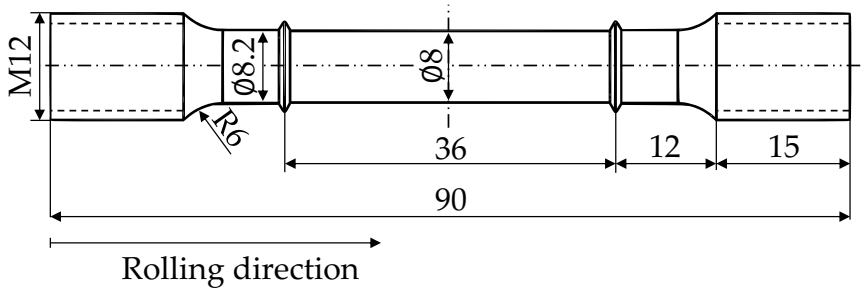

Figure 27. Geometry and key dimensions of a generic test piece design. Units are in millimetres.

3.3.2. Equipment

The creep-ageing tests were performed on a Phoenix (West Midlands, England, UK) F1010 tensile **creep machine**. The creep machine consists of a Lenton (Derbyshire, England, UK) furnace chamber and an auto-balance lever system to ensure uniform load application. Two K-type **thermocouples** were used to record test piece temperature during creep-ageing. The deforming extension was measured using two linear **capacitance gauges** capable of measuring a maximum gauge elongation of up to 2.2 mm. An Instron (Norwood, MA, USA) high magnification **extensometer calibrator** and a **digital voltmeter** were used for calibration of the capacitance gauge unit.

The room temperature tensile tests were carried out on an Instron 5584 **material testing system**. The corresponding strain response was measured using an Instron 2630-107 strain gauge **extensometer**.

3.3.3. Procedures

3.3.3.1. Procedure for calibration of the capacitance gauge unit

The capacitance gauge unit was calibrated before it was used in the creep-ageing tests. The calibration procedure is summarised as follows:

i. A ridged calibration pin was fitted to half a capacitance gauge unit that consists of two capacitance sensors, sensors 1 and 2. The fixture was assembled as shown in Figure 28a. The other half of the gauge unit with sensors 3 and 4 was assembled the same way.

ii. The fixture with sensors 1 and 2 was installed onto one side of the calibrator and the other fixture with sensors 3 and 4 was installed onto the other side (Figure 28b).

iii. The calibrator was connected to the digital voltmeter.

iv. The micrometer head on the calibrator was rotated until a voltmeter reading of 0 V was reached.

v. The voltmeter reading was recorded at predetermined displacement intervals for a linear voltage-displacement relationship unique to the capacitance gauge unit to be obtained.

Upon calibration of the capacitance gauge unit, the ridged calibration pins were replaced by a creep-ageing tensile test piece. The creep-ageing test was now ready to begin.

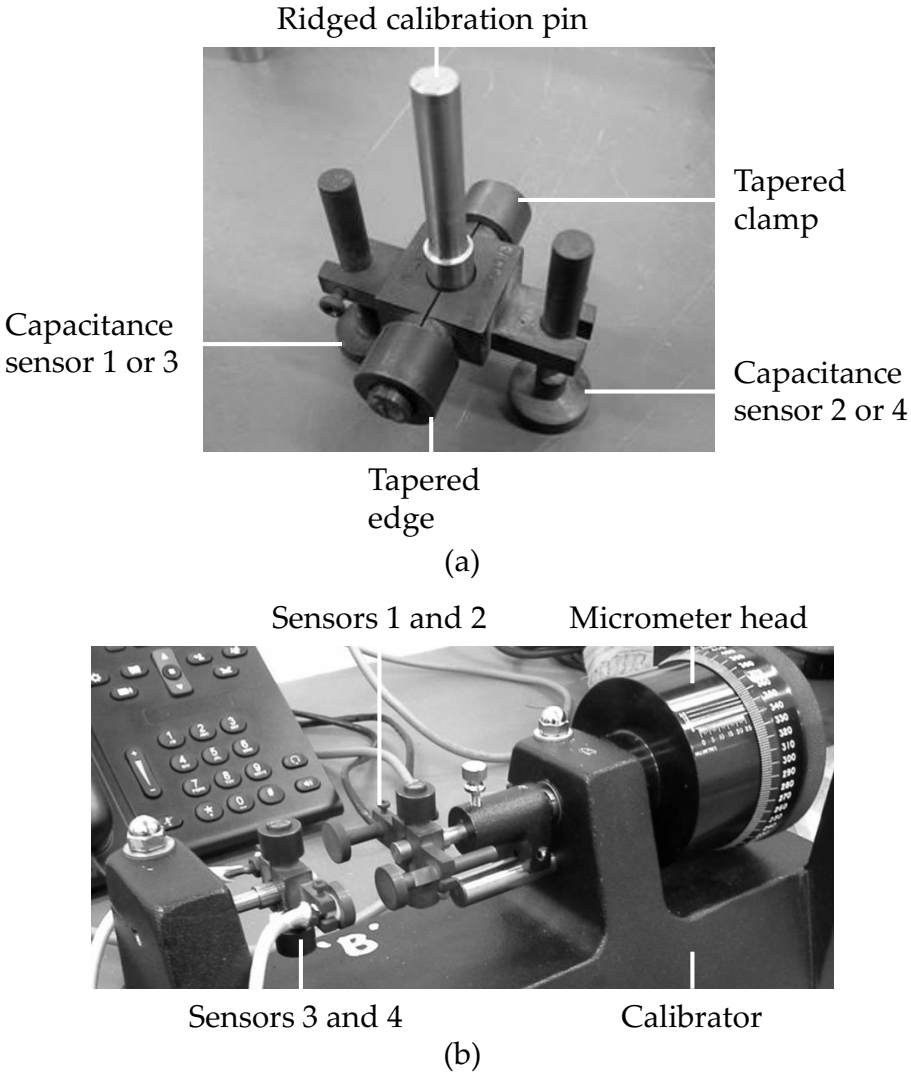

Figure 28. (a) The assembly of half a capacitance gauge unit fitted with a ridged calibration pin. (b) The extensometer calibrator with the capacitance gauge unit installed.

3.3.3.2. Procedure for creep-ageing and tensile tests

Figure 29a illustrates the experimental setup of the creep-ageing tests. The creep-ageing test procedure is summarised as follows:

i. The calibrated capacitance gauge unit was fitted onto the test piece and two thermocouples were attached to the test piece, one near the top ridge and the other near the bottom ridge.

ii. The whole fixture was installed onto the creep machine and aligned.

iii. The thermocouples were plugged-in to a panel that was connected to a data acquisition unit, which was connected to a control computer.

iv. The capacitance sensors were connected to the same digital voltmeter that was used for their calibration, which was now connected to the data acquisition unit.

v. The furnace was shut and thermal cotton was inserted into any visible gaps found between the enclosed chamber and the laboratory environment to reduce heat loss.

vi. The target creep-ageing temperature was set, the required frequency(ies) of data acquisition were input to the control computer and the heating was switched on.

vii. The target temperature of the furnace was reached and stabilised. The loading was gradually applied in the form of weights. The amount of weights was determined to give the required stress level to the initial cross-sectional area of the test piece, taking into account the leverage ratio of the lever system.

viii. The target time was reached, the data logger was stopped and the heating was switched off. The furnace was opened and the weights were removed.

ix. When cooled down, the creep-aged test piece was removed from the furnace chamber and the creep machine.

After each test, the voltage-time data acquired for the gauge extension was first converted into extension-time data and finally into strain-time data.

Room temperature tensile tests were then performed on all of the as-received, stress-free-aged and creep-aged test pieces on the material testing system at a crosshead speed of 1 mm min^{-1} (Figure 29b).

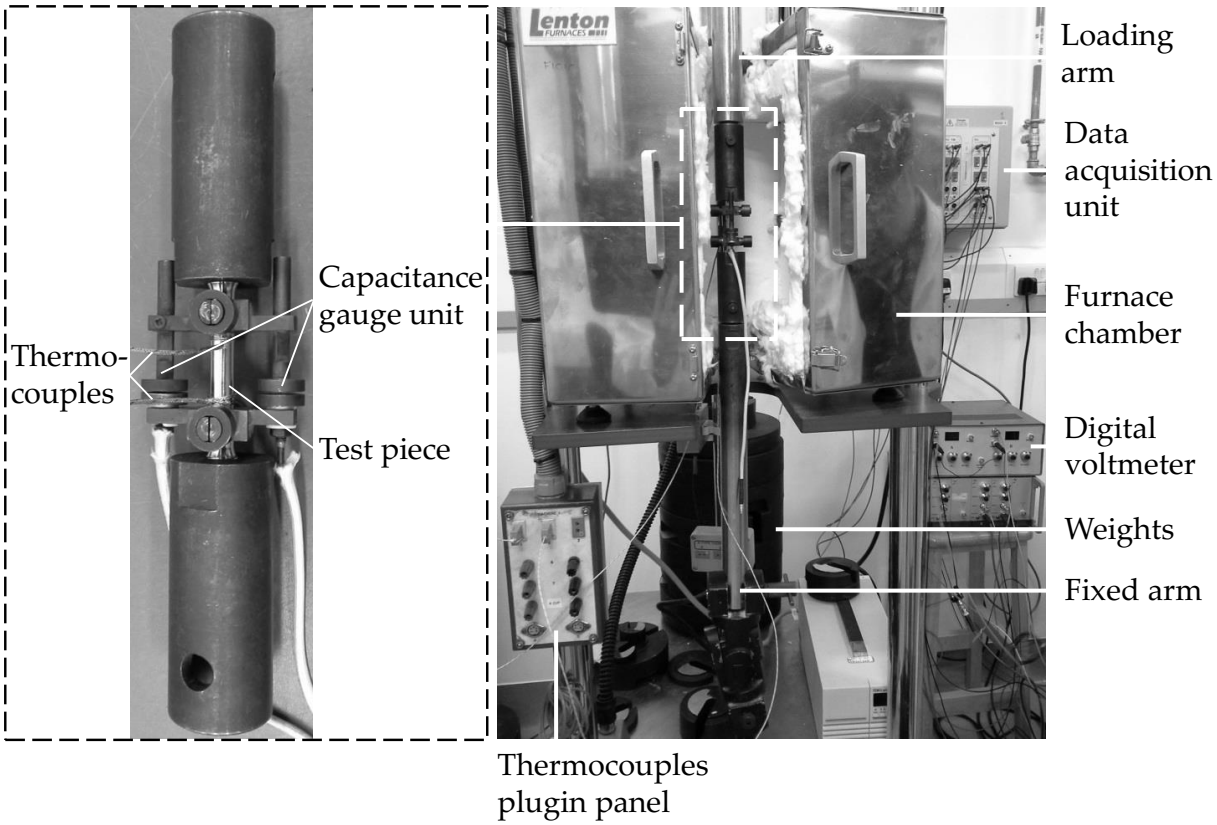

Figure 29. Experimental setup of (a) the creep-ageing test and (b) the tensile test.

3.4. Flexible creep-age forming tests

3.4.1. Plate dimensions

7B04-T651 plates of 600 mm in length and 350 mm in width were provided by AVIC BAMTRI in the longitudinal rolling orientation. The plates were wire-cut from the same batch of materials as those of the creep-ageing and tensile test pieces and further machined down to the required thicknesses.

3.4.2. Equipment

3.4.2.1. Flexible creep-age forming tool

The purpose of designing a flexible CAF tool was twofold: the first was an attempt to close the technology gap that exists in the field of flexible form tools for shaping extra-large components via CAF; the second was for the proposed design to be applied in this research to enable model validation and springback compensation studies to be carried out.

The number of pins in a discrete element multipoint tool, or part-count, was identified as a key to the advancement of the current flexible tooling technology. Part-count plays an important role as reducing it reduces both the weight as well as the costs of manufacturing and maintaining the tool at the same time. A preliminary research has been carried out by the author and colleagues which seeks to propose a lightweight apparatus with improved flexibility and shorter setup time for modifying the shape of an aircraft component. The proposed apparatus adopts the concept of modularity in design, making it capable of being upgraded or downgraded as required, introducing further economic incentives for manufactures to adopt this tool for the production of extra-large components. Figure 30 shows a lightweight and flexible CAF tool for producing extra-large panel components, in the form of a metal wing skin portion of a complex shape.

The tool comprises two halves, a top die and a bottom die, which have the same structural arrangement such that any individual parts from the bottom die can

be taken out and installed in the same way to the top die if required. Each die consists of two guiding rails along the direction of wing span and are rigidly fixed to a base (not illustrated). A number of modules are firmly supported by the guiding rails and can slide along the span direction as allowed by the guiding rails. Once slid to the required position, modules are fixed to the guiding rails, thus are structurally supported by both the guiding rails and the base (not illustrated). The modules from this instance onwards are firmly fixed in position. The number of modules may be increased or decreased by adding on or removing modules from the guiding rails.

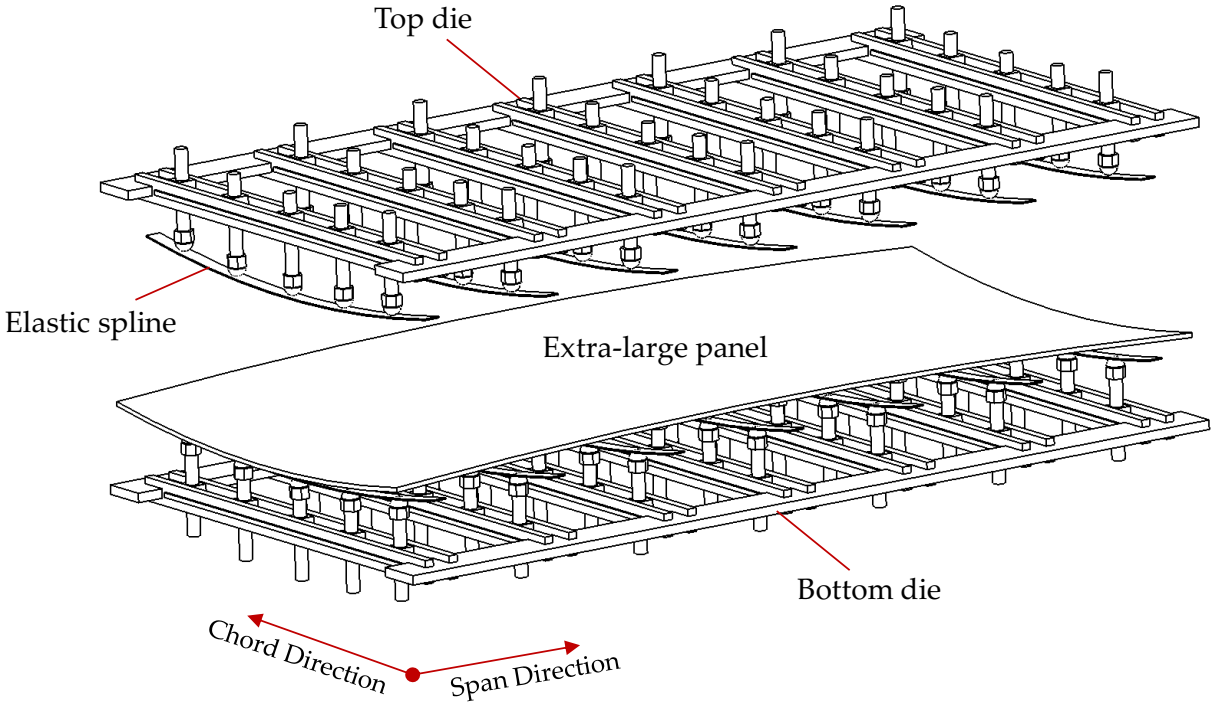

Figure 30. An isometric view of the present invention showing a possible configuration and arrangement of the creep-age forming tool.

Figure 31 shows a cross section of the tool shown in Figure 30. Attached to the forming pins of each module is an elastically deformed spline. The shapes of the elastic splines are controlled by the positions (in the chord direction) and heights of the forming pins that it is being attached to, which are determined according to the shape control requirement for forming the panel. The attachment method between the workhead of each forming pin and the spline enables the spline to slide in the

chord direction over the surface of the workhead but does not detach in the out-of-plane direction.

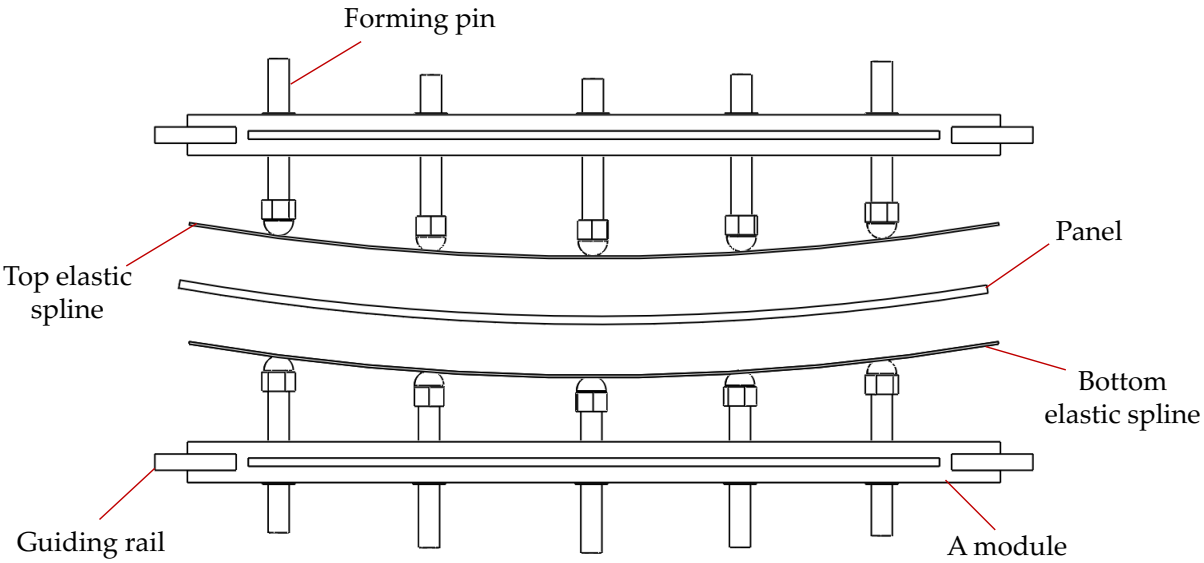

Figure 31. Cross-section view of the tool showing a pair of elastic splines with their shape being controlled by the forming pins that each spline is attached to.

Figure 32 shows the structural arrangement of the base tooling structure. The base unit is designed to enable movements in all orthogonal axes. Movement in the span direction is provided by the sliding motion of the module rack on the guiding rail, whilst that in the chord direction can be achieved by sliding the pin housing on the module rack. Each pin height is achieved by the interaction between the pin housing and the groves on the body of each forming pin.

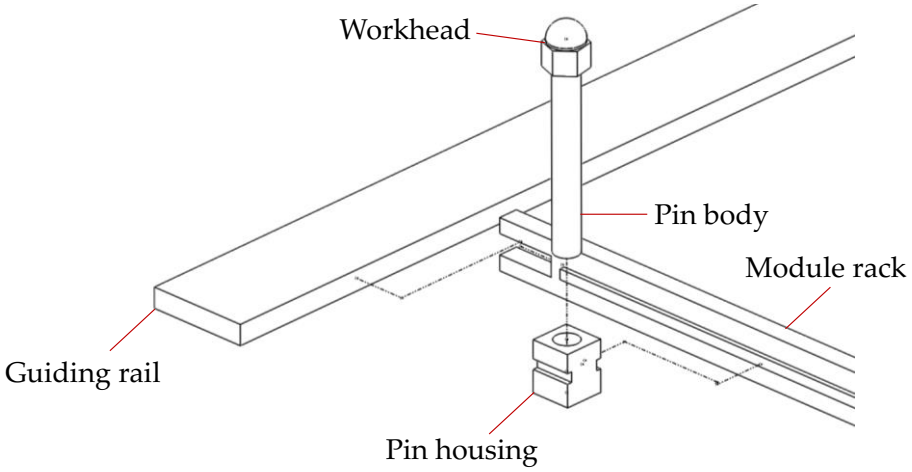

Figure 32. Assembly of the base tooling structure.

Each forming pin unit consists of a forming pin and a pin housing which main role is, together with the module rack, to provide the sliding motion required to slide the forming pin to the required position along the chord direction. Once positioned, each forming pin unit is firmly fixed to the module by fixing the pin housing to the module rack and the positions of the forming pins are chosen so that, when all forming pins are positioned and adjusted correctly in the three dimensional space, deflection surface of the spline that is being attached to the forming pins, will deform to the shape of the required forming surface within pre-defined tolerances.

The forming pins, module racks, guiding rails, pin housing and the base (not illustrated), which all together form a rigid supporting structure, are made of material that are substantially stiff and undergo negligible deformation during a CAF process.

In a typical CAF process, splines with a selected thickness are first attached to the workheads of the forming pins. Forming pins are then moved to the required position and adjusted to the required heights as the splines' shape change accordingly. The splines are made of a material with yield strength sufficiently high to prevent it from deforming plastically at all times. An extra-large panel is then placed on the upper surfaces of the splines which now have the required shape for forming.

Forming pins on the top die are positioned and adjusted in a similar way but with splines' shapes matching those on the bottom die. As the top die is lowered with load applied to the panel, the panel and splines will all deform in a way that can be predicted with a combined knowledge in the panel's material behaviour as well as the mechanics of beam bending, plate bending and sheet metal forming.

When the panel is fully deformed, the tool is locked in place which means that now the deformed panel and splines are no longer movable and being held at such configuration. The whole apparatus is then transported to and placed inside an oven, where a heat treatment cycle is provided to the whole apparatus at an elevated

temperature for a predetermined period of time. The panel undergoes creep deformation during this period, as the material constituents of the panel precipitate, altering the microstructure of the alloy, thereby strengthening it. Each heat treatment cycle is unique to each alloy material of which the panel is made of and is set so that the creep-age formed panel will have final mechanical properties that meet the strength specification.

After the heat treatment cycle, the oven is ventilated to allow the apparatus to return to room temperature. The cooled apparatus is then removed from the oven and the top die is raised to a position sufficiently high so that the panel is allowed to springback. Springback is a result of residual elastic stresses; it springs back to a shape somewhere between its original shape and the shape defined by the splines. As the splines get detached from the forming pins after each forming operation, they return fully to their original shape and are ready to be re-used again.

This apparatus/die mechanism now has a pending patent filed at the UK Intellectual Property Office (Lam *et al.*, 2015c). The preliminary work associated to this design method has been carried out and presented at the International Journal of Advanced Manufacturing Technology (Lam *et al.*, 2015b).

To meet the second purpose of the design initiatives, a laboratory-scale flexible CAF tool was made which represents an explicit form of the original modular tool design. Figure 33 shows the final design of the flexible CAF tool. The CAF tool consists of a top and a bottom plate, each acting as a die holder. The bottom plate is supported by two U-channels designed for forklift entry. Four guide bushes and four guide pillars are secured close to the four corners of the top and bottom plates respectively. The guide bushes ensure stability and low friction contact with the guide pillars. Both plates are machined with forty-five M24-threaded holes across the central plate region for housing forming pins, making the form tool more flexible in configuration and lighter in weight.

In the configuration shown, each plate is fixed with twenty-five forming pins. Each forming pin is put together from an M24 studding bar with an M24 domed cap hex nut fixed to one end of the bar, acting as the workhead. The form tool has a locking mechanism designed to hold the loaded part in place for creep-ageing submission. After the form tool is unlocked and unloaded, the four die springs slightly counteract all downward forces and enable the form tool to self-open.

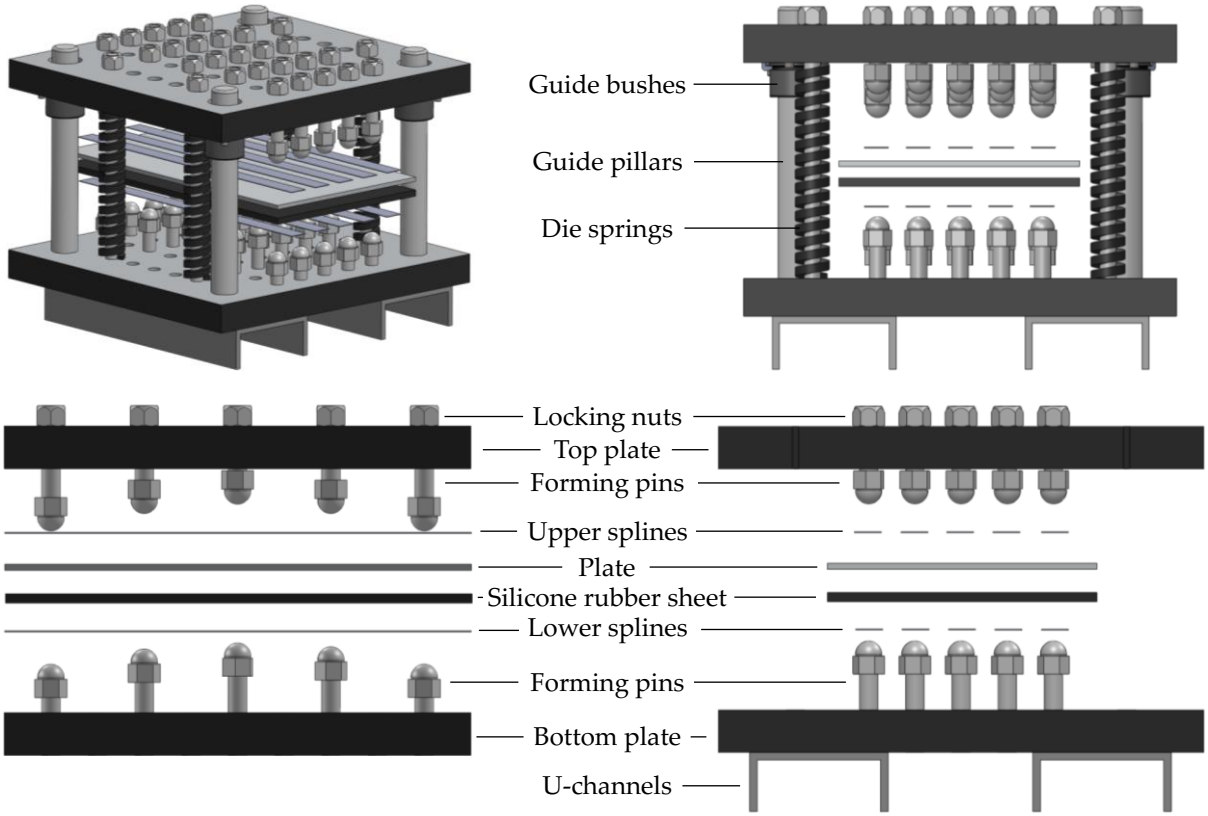

Figure 33. Final design of the flexible form tool.

During setup for CAF, flexible splines are placed above and below the plate with an additional sheet of silicon rubber placed between the lower splines and the plate. This optimal form tool design is recommended based on finite element stress analysis of CAF operations using the form tool. Details of the stress analysis are presented in Appendix B.

The design output of this laboratory-scale flexible CAF tool, containing detail drawings, current forming limit of the tool, record of part count, weight estimation and purchased parts details, is summarised in Appendix C.

3.4.2.2. Other equipment

A **coordinate measuring machine** (CMM, LK G90C, Nikon Metrology UK) was used for part shape measurements. Digital Vernier **callipers**, a digital **height gauge** and **tape measures** were used for general measurements. A pair of HyFlex **gloves** with PU palm coat and Dynema/Lycra liner was used for rough work handling. **Adjustable spanners** and a 38 mm **box spanner** were used for bolts and nuts fixing. A set of **pin height adjustment tool** was made from steel precision rulers and magnets (Figure 34). A 255 ton Instron servo-hydraulic **test machine** was used for loading and unloading. Two solid **load transmission cylinders** of 150 mm in diameter and 350 mm in height were made of aluminium and were designed to transmit load from the loading plate of the test machine to the top plate of the CAF tool. Electric and mechanical **forklifts** were used to carry the CAF tool to and from a **trolley** for transportation. A large Aerotherm (Staffordshire, England, UK) **box oven** was used to provide the creep-ageing thermal cycle. A **digital thermometer** and K-type **thermocouples** were used to monitor the part's temperature during creep-ageing. At every test interval, high temperature **lubricants** were applied to the guide pillars of the CAF tool to ensure smooth loading and unloading motions of the top plate.

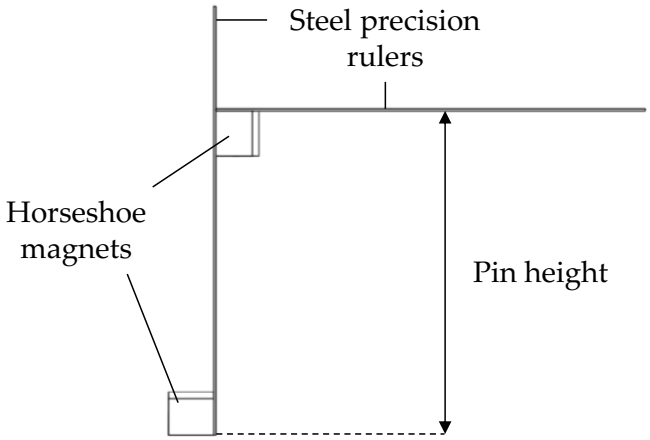

Figure 34. Schematic of the pin height adjustment tool.

3.4.3. Procedures

3.4.3.1. Procedure for part preparation

Gridlines marking. All the as-received plates contained a certain degree of distortions. Their main mode of distortion, as illustrated in Figure 35a, was single curvature bending. Figure 35b shows the plate dimensions and the spacing of the gridlines that were marked on the convex surface of each plate. The gridlines were used to aid thickness measurement, initial distortion measurement and plate-tool alignment during CAF test setup.

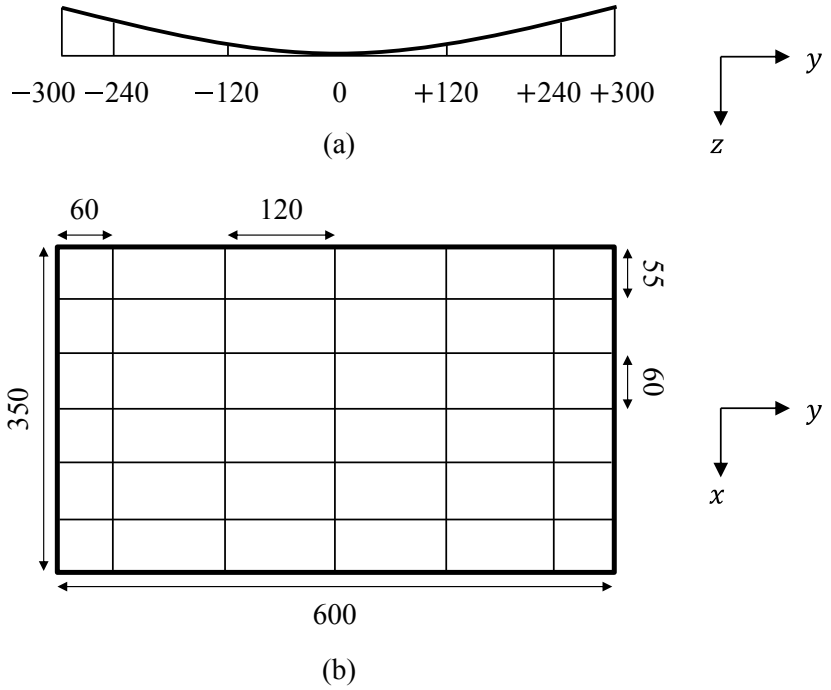

Figure 35. Schematics of (a) the initial plate distortion and (b) the plate dimensions and spacing of the gridlines drawn on the plates upon receiving them. Units are in millimetres.

Thickness measurement. An average plate thickness was obtained for each plate based on twenty measurements that were recorded at the gridline positions along the four edges of each plate using the callipers.

Initial distortion measurement. The height gauge was used to measure the initial deflection of the nine plates that were to be submitted to single curvature CAF tests for model validation. These measurements were made at the gridlines positions as shown in Figure 35a. On the other hand, the CMM was used to record the initial

three-dimensional part shape of the three plates that were to be submitted to double curvature CAF tests for springback compensation studies. The CMM measurements were taken along the gridlines of each plate at 10 mm intervals. An operation manual for the CMM, including a template of the CMM program used, was produced and is presented in Appendix D.

3.4.3.2. Procedure for flexible form tool test setup

Pin height generation. The shape of the forming surface depends on the height of each forming pin. Based on vector and surface calculations, a pin height generation algorithm *dieshape3d.m* has been written in MATLAB (MathWorks, Natick, MA, USA) to predict the required pin heights given a required loaded part shape. The part shape may be described by either a 3D point cloud or an equation of a surface.

Forming test setup. Pin heights were adjusted using the adjustment tool (Figure 36a). Once fully adjusted (Figure 36b), splines were placed on the workheads of the forming pins and topped with silicone rubber sheet (Figure 36c). The plate was then placed on top of the silicone rubber sheet and aligned with the aid of the gridlines (Figure 36d). Finally, the upper splines were placed on top of the plate, again aligned with the gridlines provided.

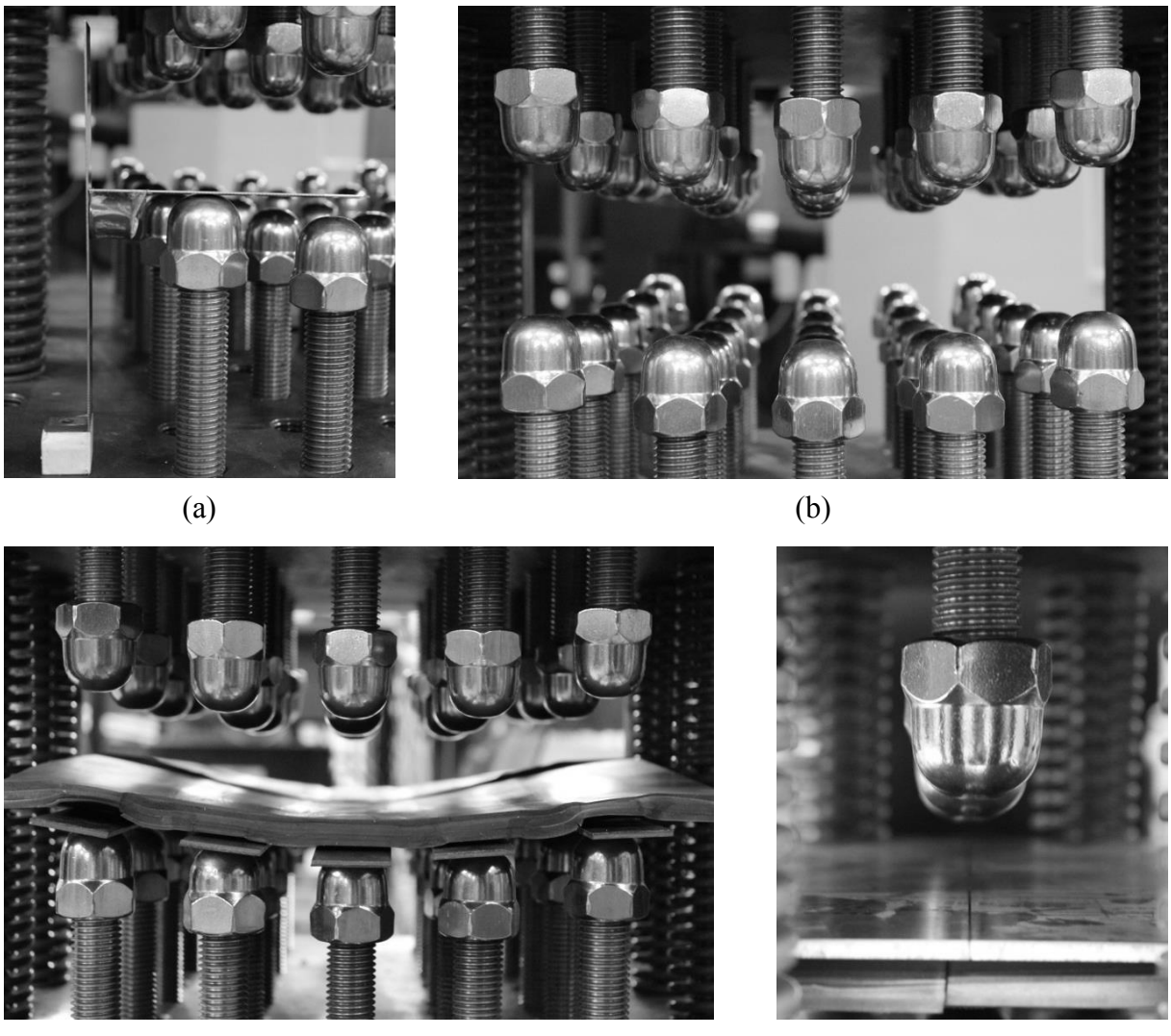

Figure 36. Sequential images of the flexible form tool setup process.

3.4.3.3. Procedure for creep-age forming tests

Loading. The test machine was set to its compression configuration with two hydraulic pumps of the DFF laboratory switched on to maintain oil pressure. The electric forklift must always be on the ground floor and the mechanical forklift must always be on the first floor. The trolley should always be near the form tool at all times. The loading procedure is summarised as follows:

i. The test machine was switched on by starting from low to high pressure. The frame was brought to its lowest position at −250 mm.
ii. The actuator was raised until there was enough room for the form tool to be placed on the base plate of the test machine.
iii. The form tool was placed on the test machine using the electric forklift.
iv. The load transmission cylinders were placed diagonally on the top plate of the form tool so that load can be transmitted from the loading plate of the test machine to the top plate.
v. The actuator was lowered until the load value indicates an initial contact with the cylinders. The load was reset to zero. An image of the CAF test setup at this point is illustrated in Figure 37a.
vi. The actuator was further lowered until the plate is fully loaded. During loading, the machine load was recorded at every 1 mm interval.
vii. When fully loaded, the top plate of the form tool was locked. The actuator was raised and the form tool was carried away from the test machine to the trolley using the electric forklift.
viii. The form tool, now on the trolley, was transported from the ground floor to the first floor. The form tool was carried away from the trolley and placed inside the box oven using the mechanical forklift. The creep-ageing step was now ready to begin.

Creep-ageing. The thermocouples were inserted between the splines and the deformed plate (Figure 37b). The box oven was shut and insulated with the thermocouples extending to the outside of the box oven. The thermocouples were plugged-in to the digital thermometer. The oven temperature and over-heating control were set, safety signs were displayed in correspondence with the laboratory's regulations and the heating was switched on. It was assumed that the creep-ageing time had begun when the plate's temperature had reached -5% of the target temperature (i.e. 109.25 °C for a creep-ageing temperature of 115 °C) and the 22 h of creep-ageing time were counted from then onwards for all the tests. After 22 h, the heating was switched off and the oven was opened.

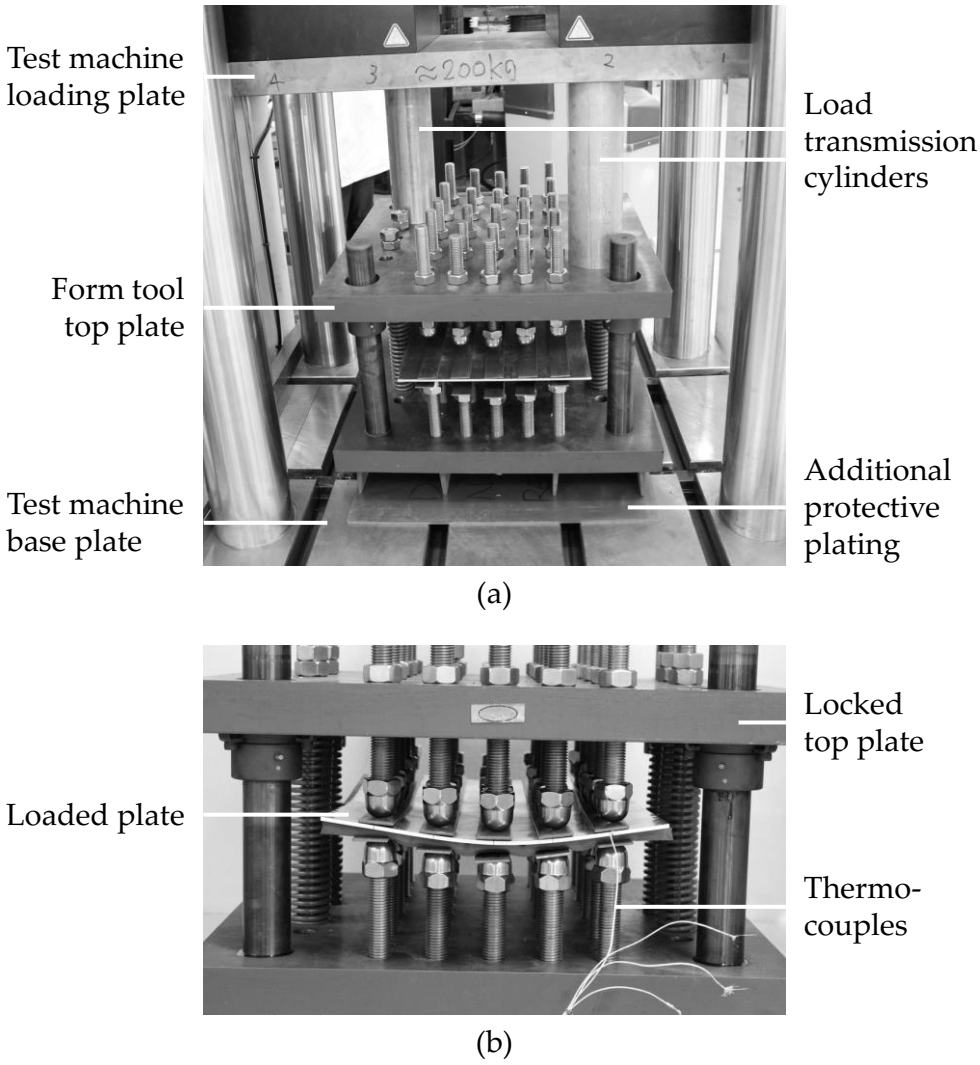

Figure 37. Creep-age forming test setup for (a) the loading stage and (b) the creep-age stage.

Unloading and part shape measurement. The plate was unloaded after it was returned to room temperature. The procedure for unloading can be referred to those for loading but reversed. The formed part shape was measured after unloading. The procedure for measuring the formed part shape is the same as those for initial distortion measurement.

CHAPTER 4.

EXPERIMENTAL RESULTS & DISCUSSIONS

4.1. Creep-ageing behaviour of aluminium alloy 7B04-T651

Figure 38 shows the creep-ageing curves of the 7B04-T651 test pieces creep-aged under the indicated stress levels at a temperature of 115 °C for up to 22 h. All the creep-ageing curves take a similar form of shape–with creep-ageing strain increases with time whilst the strain rate plummets in the primary creep stage (0 to 4 h); the strain rate then remained steady in the secondary creep stage (4 to 22 h). Generally, a higher applied stress level leads to a higher overall creep strain rate.

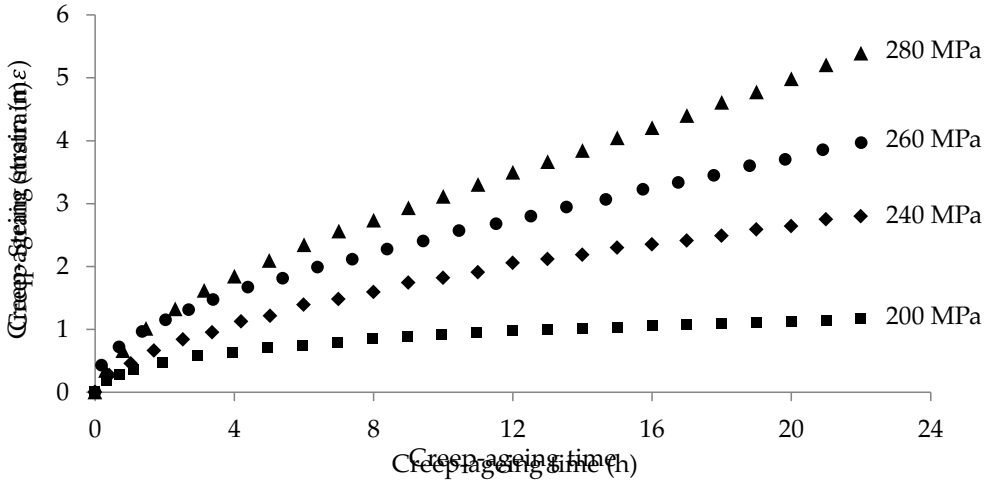

Figure 38. Creep-ageing curves of 7B04-T651 test pieces under the indicated applied stress levels.

Under the CAF conditions studied, the present alloy exhibited a total accumulated strain of between 1.2 to 5.4 millistrain after 22 h of creep-ageing. This

means a lower formability in comparison with the results presented by Li *et al.* (2010) for 7B04-T7451 (150 °C, 15 h) under a range of applied stress levels between 240 to 300 MPa. However, it should be noted that their creep-ageing temperature is different. In addition, the TEM analysis revealed an average growth in precipitate size from 8.5 to 12.6 nm after 22 h of stress-free-ageing (Appendix E). This is comparable with the alloy they studied, which revealed an average growth of 16 to 37 nm after 15 h of creep-ageing under stress levels of between 240 to 300 MPa at 150 °C.

Figure 39 shows the yield strengths of the 7B04-T651 test pieces stress-free-aged/creep-aged under the indicated stress levels at a temperature of 115 °C for up to 22 h. The material's yield strength is generally lower for the stress-free-aged samples in comparison with those that were creep-aged. However, the alloy exhibited no apparent sign of hardening/softening due to further ageing. For the test pieces that were creep-aged under the applied stresses of 200 to 280 MPa, the material's yield strength exhibits no apparent trend and scatters between 530 to 555 MPa. This is much stronger than the alloy studied by Li *et al.* (2010), which exhibited a range of yield strength between 430 to 480 MPa. Complete stress-strain curves of the test pieces are presented in Appendix F.

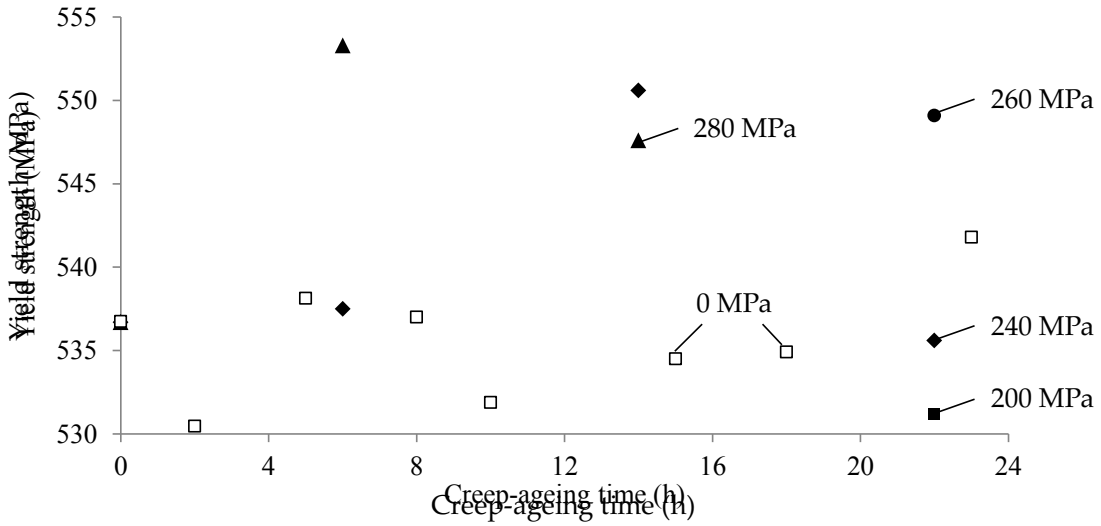

Figure 39. Yield strength evolutions of 7B04-T651 test pieces over creep-ageing time under the indicated applied stress levels.

4.2. Springback of singly curved creep-age formed plates

Table 7 summarises the average plate thickness and initial deflections of the plates selected for the single curvature CAF tests. The thinner plates tend to have larger initial deflections.

Table 7. Average thickness and initial deflections of the formed plates.

#	Average thickness (mm)	Initial deflections (mm) at			
		$y = 0$ mm	$y = 120$ mm	$y = 240$ mm	$y = 300$ mm
1	3.20	0	0.67	1.75	2.42
2	3.26	0	0.75	1.95	2.70
3	3.40	0	1.31	3.05	3.73
4	4.88	0	0.50	2.50	3.50
5	5.30	0	0.65	2.38	4.97
6	5.31	0	0.06	0.10	0.12
7	8.09	0	0.05	0.10	0.13
8	8.20	0	0.35	0.70	0.88
9	8.20	0	0.36	0.92	1.14

Thrice-repeated single curvature CAF tests were performed for each plate at a span bending radius of 1200 mm and chord bending radius of 9E99 mm. Table 8 presents the final deflections of the singly curved formed plates. No apparent trend is observed by making comparisons between plate thickness and final deflections but the latter seem to have a certain degree of correlation with the initial deflections of the plates.

Table 8. Average thickness and final deflections of the formed plates.

#	Average thickness (mm)	Final deflections (mm) at		
		$y = 0$ mm	$y = 120$ mm	$y = 240$ mm
1	3.20	0	2.36	3.27
2	3.26	0	2.77	3.76
3	3.40	0	3.85	5.22
4	4.88	0	3.67	4.99
5	5.30	0	3.63	4.91
6	5.31	0	1.81	2.53
7	8.09	0	2.57	3.57
8	8.20	0	3.32	4.51
9	8.20	0	3.18	4.35

CHAPTER 5.

MATERIAL & PROCESS MODELLING TECHNIQUES

5.1. Introduction

This chapter describes the development of a generic finite element (FE) model for modelling flexible CAF operations and predicting springback of panel components creep-age formed under different loading scenarios. Figure 40 presents an overview of the modelling methodology implemented in this thesis.

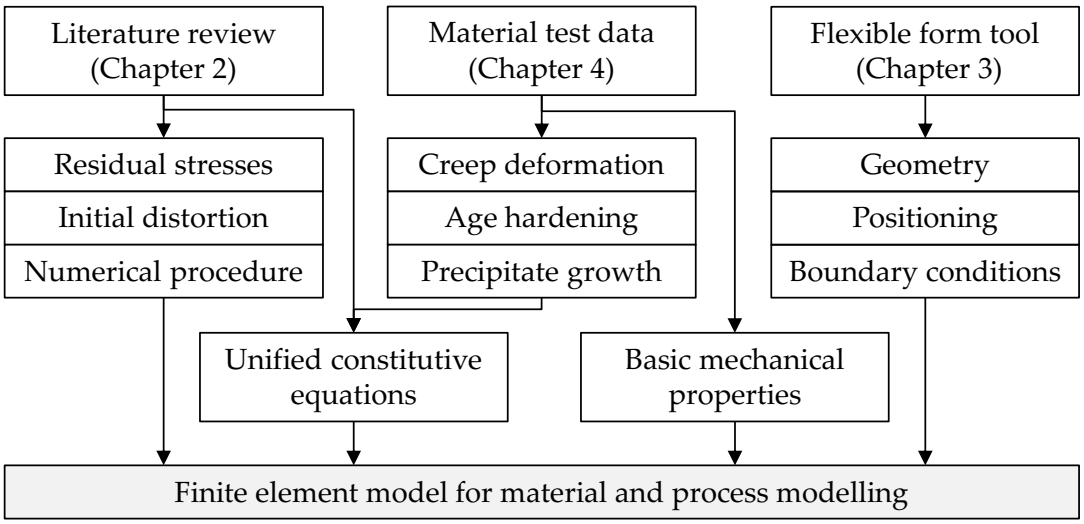

Figure 40. An overview of the material and process modelling methodology.

Using the material test data presented in Chapter 4, material constants and initial conditions for CAF of 7B04-T651 at 115 °C for 22 h were determined for a set of mechanism-based, unified creep-ageing constitutive equations presented in

Chapter 2. The multiaxial viscoplastic material model was implemented into a commercial FE solver and followed by the verification of the material modelling result. A geometric model of the flexible CAF tool described in Chapter 3 was then developed. The material model for 7B04-T651 and the geometric model of the flexible form tool together make up the generic FE model for modelling flexible CAF operations. This FE model takes into account thermal-friction interactions between tooling and plate surfaces and the typical residual stress fields that exist in surface-machined 7000-series aluminium plates prior to forming. Finally, the numerical and definition procedures used to define a case-specific FE model are presented at the end of this chapter.

5.2. Material modelling technique

5.2.1. Constitutive equations

In order for double curvature CAF to be modelled, Zhan *et al.* (2011b) rewrote the equation set (Eqs. (2.18) – (2.24)) to take into account the multiaxial creep-ageing behaviour of 7000-series aluminium alloys. The multiaxial constitutive equation set is presented as follows:

$$\dot{\varepsilon}_e^{cr} = A_1 \sinh\{B_1[\sigma_e(1-\overline{\rho}_d) - k_{\varepsilon c}\sigma_y]\} \tag{5.1}$$

$$\dot{\sigma}_{age} = C_a \dot{\overline{r}}_p{}^{m_1}(1-\overline{r}_p) \tag{5.2}$$

$$\dot{\sigma}_{sol} = C_s \dot{\overline{r}}_p{}^{m_2}(\overline{r}_p - 1) \tag{5.3}$$

$$\dot{\sigma}_{dis} = A_2 \cdot n_d \cdot \overline{\rho}_d{}^{n_d-1}\dot{\overline{\rho}}_d \tag{5.4}$$

$$\sigma_y = \sigma_{sol} + \sqrt{\sigma_{age}^2 + \sigma_{dis}^2} \tag{5.5}$$

$$\dot{\overline{r}}_p = C_r(Q_r - \overline{r}_p)^{m_3}(1 + \gamma_r \overline{\rho}_d{}^{m_4}) \tag{5.6}$$

$$\dot{\overline{\rho}}_d = A_3(1-\overline{\rho}_d)\dot{\varepsilon}_e^{cr} - C_\rho \overline{\rho}_d{}^{m_5} \tag{5.7}$$

where A_1, B_1, $k_{\varepsilon c}$, C_a, m_1, C_s, m_2, A_2, n_d, C_r, Q_r, m_3, γ_r, m_4, A_3, C_ρ and m_5 are material constants in Eqs. (5.1) – (5.7). Equivalent rate of creep strain ($\dot{\varepsilon}_e^{cr}$) is a function of

normalised dislocation density ($\overline{\rho}_d$), von Mises equivalent stress (σ_e) and the material's yield strength (σ_y), as described by Eq. (5.1). $\overline{\rho}_d = (\rho - \rho_i)/\rho_m$ where ρ_i and ρ_m are respectively the dislocation density of the virgin material and the maximum (saturated) dislocation density that the material could have. Thus ρ varies from ρ_i to ρ_m and $\overline{\rho}_d$ varies from 0 (initial) to 1 (saturation), assuming $\rho_i \ll \rho_m$. During CAF, the material is strengthened due to ageing (σ_{age}), solute hardening (σ_{sol}) and work (dislocation) hardening (σ_{dis}). The kinetics of these hardening mechanisms are described by Eqs. (5.2) – (5.4) respectively, and each of their contribution to σ_y is described by Eq. (5.5). Effects of σ_{age} and σ_{sol} on creep deformation are taken into account by $\overline{\rho}_d$ and the normalised radius of precipitates ($\overline{r}_p$). $\overline{r}_p = r/r_c$ where r and r_c are the current and peak-aged precipitate size respectively. $0 \leq \overline{r}_p < 1$ indicates under-ageing, $\overline{r}_p = 1$ indicates peak-ageing, and the material is over-aged when $\overline{r}_p > 1$.

5.2.2. Determination of initial conditions

Table 9 presents the initial conditions determined for modelling the CAF of 7B04-T651 at 115 °C using Eqs. (5.1) – (5.7). The as-quenched yield strength of the alloy was 206 MPa (Li *et al.*, 2008). A value of $\sigma_{sol}^0 = 190$ MPa was chosen for the as-recieved T651 condition. Before any creep-ageing takes place, $\sigma_{age}^0 = \sigma_y^0 - \sigma_{sol}^0$, where $\sigma_y^0 = 537$ MPa was obtained from the tensile tests. $\bar{r}_p^0 = 1$ was set as the material is at its peak-aged condition. The initial dislocation density is significantly smaller than the maximum dislocation density and an initial normalised dislocation density of $\bar{\rho}_d^0 =$ 1E-5 was used instead of 0 for numerical reason.

Table 9. Initial conditions for CAF of 7B04-T651 (115 °C).

σ_{sol}^0	σ_{age}^0	σ_y^0	$\bar{r}_p^0$	$\bar{\rho}_d^0$
190	347	537	1	1E-5

5.2.3. Determination of material constants

An evolutionary-algorithm-based optimisation software, developed by Zhang *et al.* (2012) and had been provided access by Prof. Jianguo Lin of Imperial College London, was used for material constant determination. The experimentally obtained creep-ageing curves and yield strength evolutions presented in Chapter 4 were used to determine the CAF material constants. This was coupled with manual constant adjustments carried out in MATLAB to calibrate for the normalised radius from TEM analysis result as mentioned in Chapter 4. Table 10 presents the material constants determined for modelling the CAF of 7B04-T651 at 115 °C.

Table 10. The material constants determined for CAF of 7B04-T651 (115 °C).

A_1	B_1	$k_{\varepsilon c}$	C_a	m_1	C_s	m_2	A_2	n_d
1.95E-6	0.042	0.16	4	0.9	0.2	0.45	260	0.7
C_r	Q_r	m_3	γ_r	m_4	A_3	C_ρ	m_5	
0.098	1.8	2.2	3	2	150	0.145	1.5	

Figure 41 illustrates a comparison of the calibrated creep-ageing curves and yield strength evolutions with those obtained experimentally via material testing. Maximum deviations of 0.29 mε and 9.35 MPa are observed after 22 h of creep-ageing, which represent a 5.6 and 1.8% difference respectively. Thus, characteristics of both the viscoplastic deformation and yield strength evolution of 7B04-T651 during creep-ageing have been captured with close agreements.

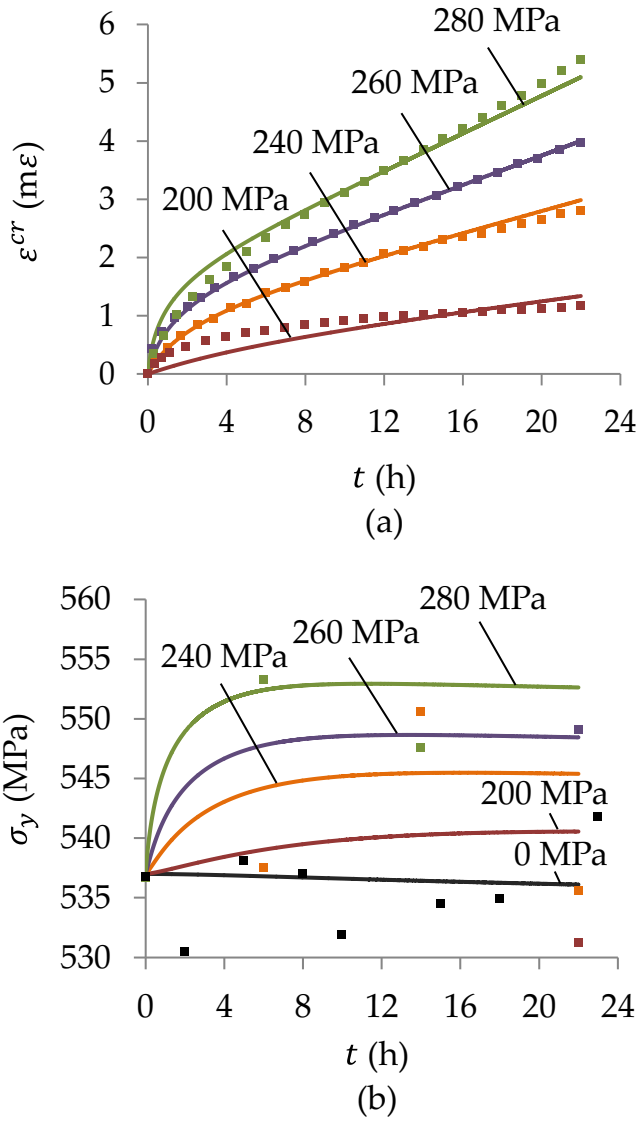

Figure 41. Comparison of the experimentally obtained (symbols) and calibrated (solid lines) (a) creep-ageing curves and (b) yield strength evolutions for creep-ageing at 115 °C under the indicated stress levels.

5.2.4. Implementation of material model

Assigning the initial conditions (Table 9) and material constants (Table 10) to Eqs. (5.1) – (5.7) gives the material model for the alloy 7B04-T651 under the CAF condition of 115 °C. This material model was implemented into the commercial FE solver Abaqus (v6.11, Dassault Systèmes Simulia, Providence, RI, USA) via the user-defined subroutine CREEP.

5.2.5. Verification of material model implementation

In order to ensure correct implementation of the material model into Abaqus, a verification study was carried out using a single beam model (Figure 42). A unit length 3D deformable wire was created in Abaqus and seeded with a global size of 0.1 mm. The wire was meshed using two-node linear beam elements B31 and treated to have a unit radius circular cross-section.

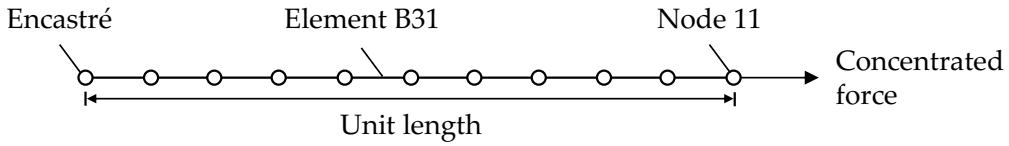

Figure 42. A schematic of the boundary and loading conditions applied to the beam model for constitutive modelling.

Basic mechanical properties of $E = 67$ GPa and $v = 0.33$ were assigned and the creep-ageing behaviour of 7B04-T651 was implemented as mentioned above. Five creep-ageing conditions were modelled which are equivalent to those that were physically tested (Chapter 3). Table 11 provides a list of the concentrated forces applied to node 11, which were calculated to match the five physically tested creep-ageing conditions.

Table 11. The concentrated forces used that correspond to the physically tested stress levels.

Required σ (MPa)	Concentrated force = $\sigma\pi$ (N)
0	0
200	628.319
240	753.982
260	816.814
280	879.646

A three-step analysis was conducted – firstly, the encastré boundary condition was assigned and allowed to propagate throughout the entire course of simulation. Secondly, the concentrated force was applied over a 1 h ramp-controlled period. Finally, creep-ageing of the material took place over a 22 h visco step with a fixed time increment of 0.001 h.

Figure 43 shows a comparison of the calibrated creep-ageing curves and yield strength evolution with the material modelling results. A close agreement between the FE-simulated and calibrated creep-ageing response is observed (Figure 43a). Under stress-free-ageing, the deviation in creep strain is almost negligible. The deviation increases slightly with increasing applied stress levels due to the use of fixed time increment. The maximum deviation of the FE-simulated creep strain from that calibrated is observed under $\sigma = 280$ MPa and is 0.17 mε (3.42% difference). The good agreement between the FE-simulated and calibrated yield strength evolution shows a similar trend (Figure 43b). Under $\sigma = 280$ MPa, the total accumulated difference in yield strength after 22 h is 0.73 MPa (0.13% difference). The deviation again decreases with reducing applied stress level and becomes negligible under $\sigma \leq 200$ MPa. These results have verified the accurate implementation of the 7B04-T651 (115 ^{o}C, 22 h) CAF material model into Abaqus.

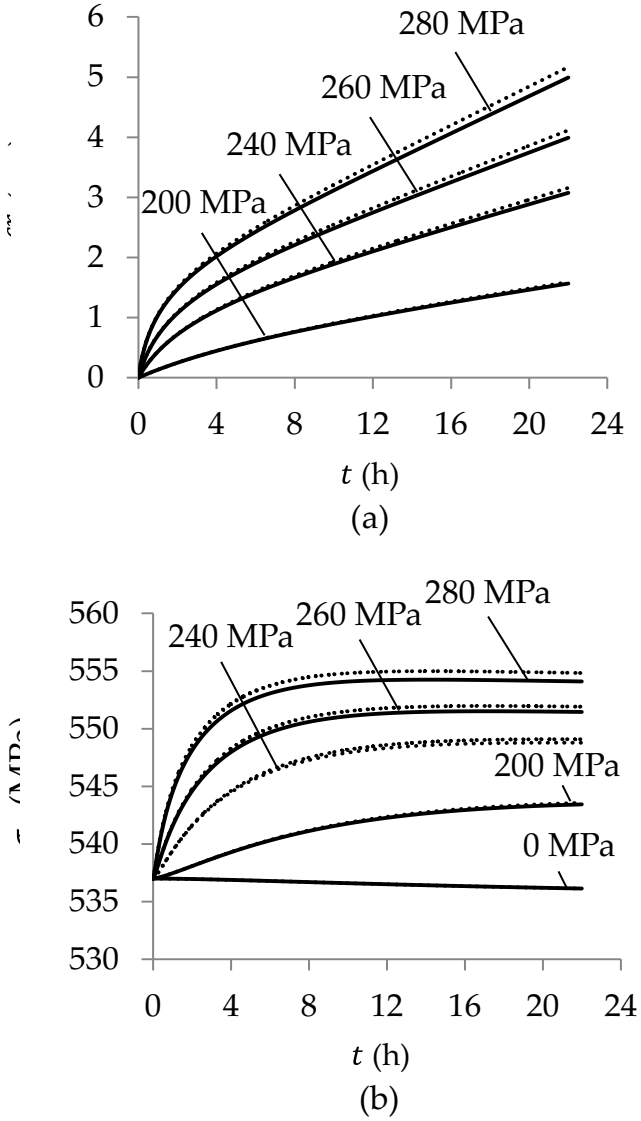

Figure 43. Comparisons of the material model calibration (solid lines) and verification (dotted lines) results. (a) Creep-ageing curves and (b) yield strength evolutions.

5.3. Process modelling technique

5.3.1. Geometry and mesh

An FE model of the flexible forming tool described in Chapter 3 was constructed in Abaqus for modelling flexible CAF operations (Figure 44).

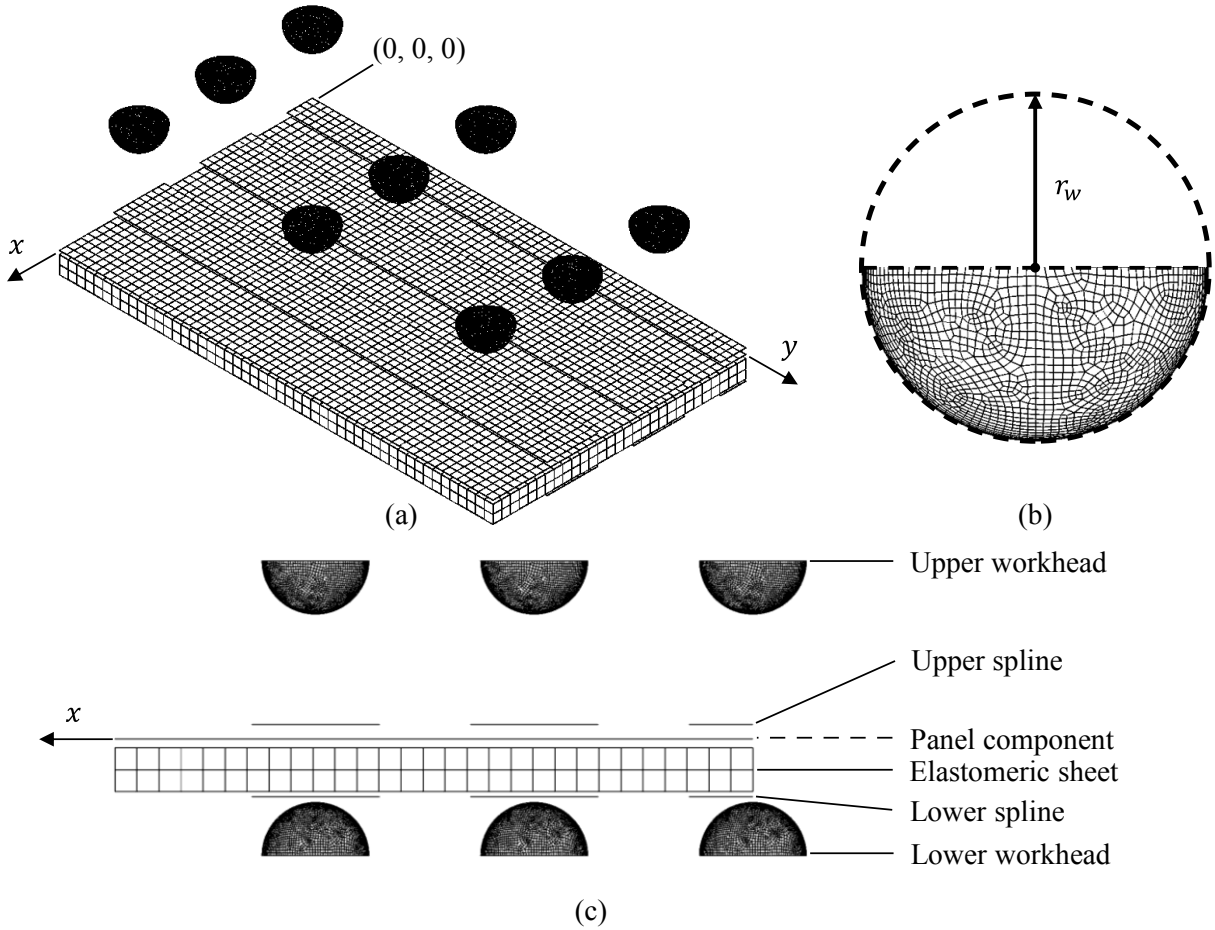

Figure 44. (a) Isometric view of the generic finite element model. (b) Finite element mesh of a workhead with an arbitrary revolving axis (dashed line) and the radius of revolvement (r_w). (c) xz-plane view of the finite element model with the different parts illustrated.

The use of a quarter model was chosen by taking into account symmetries of the target form shapes and computational time. Only workheads of the forming pins were modelled which are assumed to be perfectly spherical with a radius of r_w = 14.65 mm. The workheads were modelled using four-node discrete rigid elements R3D4.

Initial distortions of the plates were taken into account by creating a unique geometric model for each plate. For the single curvature forming tests, this was

achieved by creating four points for each plate, each positioned to the yz coordinates that correspond to the measured initial deflections (Chapter 4, Section 4.2), the four points were then connected using a spline function and the connected spline was extruded to a depth of 175 mm in the x direction to represent the width of a quarter plate. For the double curvature forming tests, the CMM-measured grid of each plate was processed using MATLAB and then transferred into Abaqus, by utilising a combination of the built-in spline and loft functions.

The splines, panel component and elastomeric sheet are all rectangular with their widths, lengths and thicknesses orientated to align with the x, y and z axes respectively. The splines and panel component were discretised using four-node linear shell elements S4R with reduced integration activated to avoid shear and membrane locking. The shell elements always represent the middle surface of the object. The elastomeric sheet was modelled using eight-node linear brick elements C3D8RH with reduced integration and hybrid formulation activated. Hybrid formulation is commonly used to model rubber-like material behaviour for incompressible ($v = 0.5$) or near incompressible ($v > 0.475$) materials (Abaqus, 2011). Table 12 presents a summary of the element and geometric properties assigned to the different parts of the FE model.

Table 12. A summary of the element and geometric properties assigned to the different parts.

Part name	Element type	$x \times y \times z$ dimensions (mm)	Number of through-thickness Simpson's integration points
Upper workheads	R3D4	-	-
Upper splines	S4R	$35^{*} \times 300 \times 3$	31
Panel component	S4R	$175 \times 300 \times h$	99
Elastomeric sheet	C3D8RH	$175 \times 300 \times 12$	-
Lower splines	S4R	$35^{*} \times 300 \times 3$	31
Lower workheads	R3D4	-	-

* The widths of the upper and lower splines in the middle along $x = 0$ are 17.5 mm due to x-symmetry.

Mesh quality plays an important role in FE modelling and can largely affect both the accuracy of the geometry represented by the mesh as well as numerical convergence of the final solution. For this reason, mesh convergence studies were

carried out on one-mesh-at-a-time on the deformable meshes of the splines, elastomeric sheet and panel component. Table 13 presents the final conditions of the convergent FE meshes. Convergences were achieved for the shape of the splines and both the shape and stress state of the panel component. Readers are referred to Appendix G for details of the convergence studies.

Table 13. The number of elements (n) and equivalent approximate global size of the convergent finite element meshes.

Mesh	n	Approximate global size (mm)
Full splines	420	5
Elastomeric sheet	2900	6
Panel component	2100	5

For the workheads which were modelled as rigid bodies, no numerical issues but their geometric representation needs taken into account. In order to ensure smooth contact surfaces, the mesh of each workhead was globally seeded with an approximate global size of 0.05 r_w.

5.3.2. Positioning and boundary conditions

The parts were positioned in a way similar to that illustrated in Figure 44. A detail graphical illustration of the model positioning and boundary conditions applied is shown in Figure 45. The centre of the panel component (or a corner of the quarter panel) was first brought to the origin at $x = y = z = 0$ and the other parts were positioned by displacing them away from the panel component, taking into account the thicknesses of shell and solid elements. For example, the z position of the upper splines is $z_{us} = +h/2 + 1.5$ mm, whilst the z position of the lower splines is $z_{ls} = -h/2 - 12 - 1.5$ mm. Nine workheads were positioned in the xy plane to match a quarter of the physical form tool design; a centre workhead was first positioned at $x = y = 0$ and the other workheads were positioned in a way so that they are spaced equidistantly by $x = 60$ mm and $y = 120$ mm in the final configuration. When setting up the model for a specific CAF operation, z positions of workheads must also

consider the thicknesses of shell elements, allowing space for splines to be placed directly under the upper workheads and above the lower workheads.

As illustrated in Figure 45a and Figure 45b, symmetric boundary conditions were applied along the lines of axes $x = 0$ and $y = 0$. An additional boundary condition, $u_x = 0$, was assigned to the centre lines of the full splines to avoid slippage to occur in the x direction. Boundary conditions of the rigid workheads were assigned through their reference points, which were positioned at the tip of each workhead (Figure 45c). The lower workheads were all assigned with an encastré boundary condition and z -positioned according to the pin height requirement for each specific case. In a similar manner, the upper workheads were fixed in all directions except in z, as each upper workhead were z-positioned and assigned with a unique displacement loading condition specific to each shape being formed.

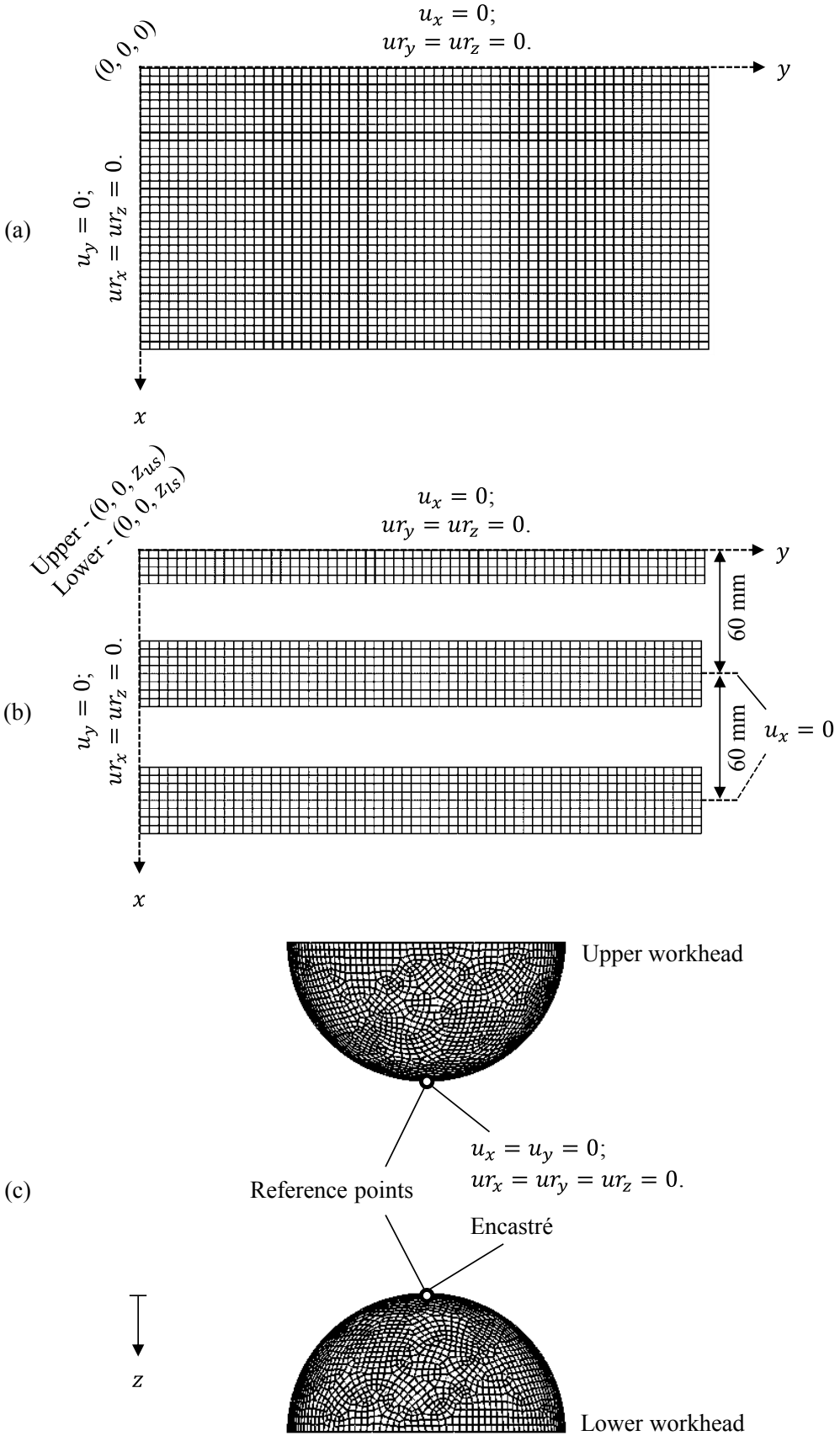

Figure 45. Positions and boundary conditions of (a) the panel component, (b) upper and lower splines, and (c) an arbitrary pair of workheads (positions not specified).

5.3.3. Material properties

Table 14 presents the materials properties assigned to the different parts of the FE model. The splines were modelled as spring steels and are not expected to experience any plastic deformation during CAF in this research. The elastomeric sheet has a Shore A hardness of 60 and was modelled as an isotropic hyperelastic material using the neo-Hookean strain energy potential given by

$$U = C_{10}(\bar{I}_1 - 3) + \frac{1}{D_1}(J^{el} - 1)^2 \ , \tag{5.8}$$

where U is the strain energy per unit of reference volume, C_{10} and D_1 are temperature-dependent material parameters, $\bar{I}_1$ is the first deviatoric strain invariant and J^{el} is the elastic volume ratio (Abaqus, 2011). Abaqus requires C_{10} and D_1 as the input parameters with the latter expressed as

$$D_1 = \frac{3(1-2\nu)}{\mu_0(1+\nu)} \ , \tag{5.9}$$

where $\mu_0 = 2C_{10}$ is the initial shear modulus of the material. Experimental and FE characterisation performed on rubber and polyurethane under tension and compression at a low strain rate of 0.05 s^{-1} suggest that the value of C_{10} for elastomers of the same hardness grade ranges between 1.3 and 1.6 MPa (Lam *et al.*, 2011). A value of $C_{10} = 1.45$ MPa was assigned to the elastomeric sheet and $D_1 = 0$ MPa which implies full incompressibility.

Table 14. A summary of the material properties assigned to the different parts.

Part name	Material	E (GPa)	ν	α (K^{-1}) (Bhushan, 2000)
Upper workheads	-	-	-	-
Upper splines	Spring steel	210	0.3	1.3E-5
Panel component	7B04-T651	67	0.33	2.3E-5
Elastomeric sheet	Silicone rubber	-	-	2.5E-5
Lower splines	Spring steel	210	0.3	1.3E-5
Lower workheads	-	-	-	-

The panel component was modelled as 7B04-T651 using the material modelling technique detailed in the preceding section.

5.3.4. Contact scheme

Table 15 presents the contact relationships between the different parts of the FE model. The stiffer body of each contact pair was always the master surface. Finite sliding formulation with surface-to-surface discretisation was used to ensure no penetration between all master and slave surfaces. A two configurations, path-based tracking algorithm was used which is preferred for tracking large relative motion on double-sided shell surfaces. Tangential behaviour was modelled using isotropic penalty formulation with friction coefficients of 0.20 and 0.25 assigned between elastomer-metal (Dirikolu and Akdemir, 2004) and aluminium-steel (Foster *et al.*, 2009) interactions respectively.

Table 15. Contact scheme and friction coefficients between contact surfaces.

		Master surface					
		Upper workheads	Upper splines	Panel component	Elastomeric sheet	Lower splines	Lower workheads
Slave surface	Upper workheads		-	-	-	-	-
	Upper splines	0.25		-	-	-	-
	Panel component	-	0.25		-	-	-
	Elastomeric sheet	-	-	0.20		0.20	-
	Lower splines	-	-	-	-		0.25
	Lower workheads	-	-	-	-	-	

5.3.5. Residual stresses

5.3.5.1. Quantification of key features

In a preliminary research conducted to investigate the influence of machining-induced residual stresses on springback prediction in CAF, considering residual stress in simulations has reduced the difference between experimental and simulated vertical plate deflections by over 34% (Lam *et al.*, 2015d). As a result of this finding, the present model takes into account the effect of the typical machining-induced

residual stress fields that exist in surface-machined 7000-series aluminium plates prior to CAF submission.

In the article, a typical machining-induced residual stress field was reconstructed using Eqs. (5.10) – (5.12). For ease of description, the equations are presented first. For $-h/2 \leq z \leq (-h/2 + d)$

$$\sigma_{res}(z) = \left(z + \frac{h}{2}\right)\left(\frac{\sigma_{res}^{surf} - \sigma_{res}^{comp}}{-d}\right) + \sigma_{res}^{surf}, \tag{5.10}$$

for $(-h/2 + d) \leq z \leq (h/2 - d)$ (adapted from Young *et al.* (2005))

$$\sigma_{res}(z) = \left(\sigma_{res}^{comp} - C\right)\left[\frac{e^{-20(X+1)} + e^{+20(X-1)}}{2}(3X^2 - 1)\right] + C, \tag{5.11}$$

and for $(h/2 - d) \leq z \leq h/2$

$$\sigma_{res}(z) = \left(z - \frac{h}{2}\right)\left(\frac{\sigma_{res}^{surf} - \sigma_{res}^{comp}}{d}\right) + \sigma_{res}^{surf}, \tag{5.12}$$

where z is the through-thickness location, h is the plate thickness, σ_{res}^{comp} and σ_{res}^{surf} are respectively the maximum compressive stress and surface stress of σ_{res} and d is the depth where σ_{res}^{comp} is observed.

Figure 46 shows a typical σ_{res} profile that was reconstructed using Eqs. (5.10) – (5.12). In Figure 46, $\bar{z}$ is the normalised thickness such that $\bar{z} = z/h$.

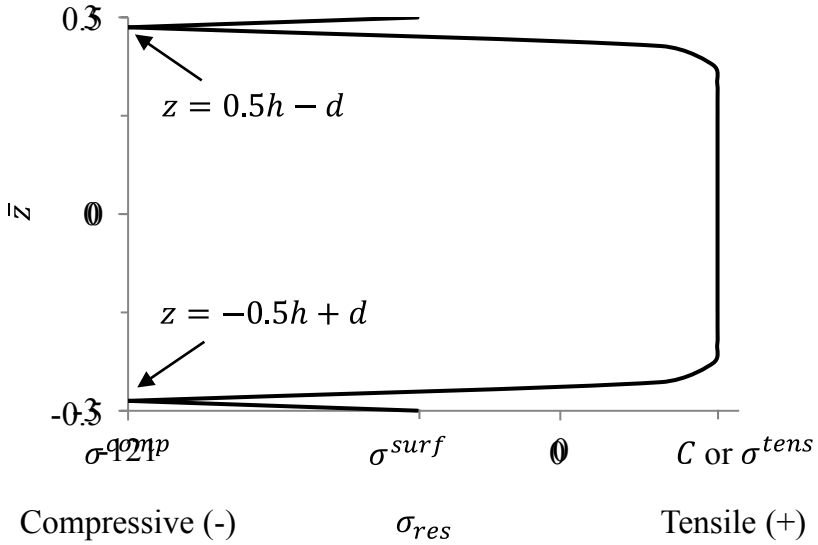

Figure 46. Key features of a typical machining-induced residual stress profile through the normalised plate thickness.

σ_{res}^{comp} does not exist on the machined surfaces but within the subsurface region (Brinksmeier *et al.*, 1982). Eq. (5.10) describes the linear subsurface σ_{res} that grows from σ_{res}^{surf} on the bottom plate surface to σ_{res}^{comp} at a depth of d above the bottom surface. Young *et al.* (2005) investigated machining-induced residual stress and distortion and a family of basis functions was proposed in order for them to determine the possible stress distributions that could have led to the distortions they observed in their experiments. One of the basis functions was adapted in Eq. (5.11) and forms the core of σ_{res}. The basis function operates within the domain $-1 \leq X \leq 1$, exhibits large magnitudes near the machined surfaces and decays exponentially to small values towards the plate centre – these are the typical features of machining-induced residual stresses. The constant C is required for σ_{res} to satisfy force and moment equilibria. Finally, Eq. (5.12) describes the linear subsurface σ_{res} for the top surface of the plate. Table 16 summarises the values that quantify the key features of σ_{res} based on literature findings. The σ_{res}^{comp} usually appears at $d = 22 \pm 8$ μm below a machined surface with its magnitude significantly greater than σ_{res}^{surf} and σ_{res}^{tens}.

Table 16. A summary of the average (standard deviation) surface, maximum compressive and maximum tensile residual stress levels due to the surface machining operations performed on 7000-series aluminium alloys by the referenced studies.

σ_{res}^{surf} (MPa)	σ_{res}^{comp} (MPa)	σ_{res}^{tens} (MPa)	References
25 (97)	-155 (86)	14 (18)	Denkena *et al.* (2008); Tang *et al.* (2009); Huang *et al.* (2013)

5.3.5.2. Implementation of residual stress fields

Assigning the values in Table 16 fully quantifies Eqs. (5.10) – (5.12). The same σ_{res} profile was assigned to the transverse and longitudinal directions of the plate as the initial σ_x and σ_y via the user-defined subroutine SIGINI. A pilot simulation was run for each case in a geostatic step to establish force and moment equilibria for the initial σ_x and σ_y. During the geostatic step, redistributions of σ_x and σ_y occur until

equilibria are satisfied. At the same time, further distortions may occur depending on the difference between the initial and final converged stresses. Since initial distortions of the plates were already taken into account by the geometric models, the distortions that arise during the geostatic step are effectively unwanted displacements. In such cases, the constant C in Eq. (5.11) was optimised so that as equilibria were satisfied, the change in maximum compressive stress due to stress redistribution and the maximum change in vertical displacement of the plate had to be smaller than 1 MPa and 1E-3 mm respectively. The final σ_{res} profile was reached for each plate upon satisfying both the equilibria and the criteria imposed on the change in maximum stress and vertical displacement at the same time.

5.3.6. Numerical procedure

Figure 47 illustrates a schematic of the temperature and displacement loading profiles for a typical CAF simulation. A six-step modelling procedure was employed and is summarised below:

i) **Initiation** – define an initial temperature (T_0), boundary conditions and contact scheme and allow them to propagate throughout the entire simulation.

ii) **Loading** – apply a unique u_z loading condition (d_r) to each upper workhead over a ramp-controlled time period (t_1). d_r is equal to the distance between the surfaces of any pair of upper and lower workheads minus the sum of thicknesses of the upper splines, panel component, elastomeric sheet and lower splines.

iii) **Heating** – apply the CAF temperature (T) to the splines, elastomeric sheet and panel component over a specific heating time (t_2) or heating rate.

iv) **Creep-ageing** – propagate the simulation into a visco step and hold it for duration of the creep-ageing time (t).

v) **Cooling** – allow the splines, elastomeric sheet and panel component to return to the initial temperature (T_0) over a specific cooling time (t_3) or cooling rate.

vi) **Unloading** – raise the upper workheads over a ramp-controlled time period (t_4).

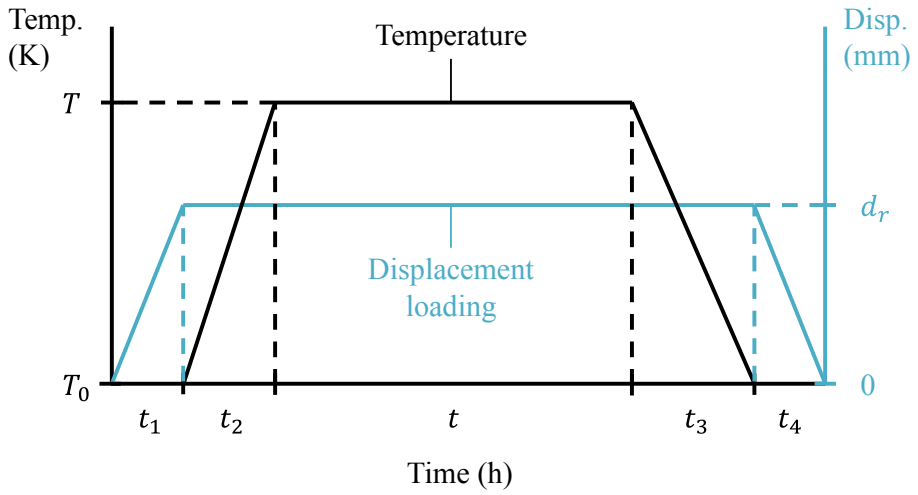

Figure 47. Schematics of the temperature and displacement-controlled loading profiles.

5.3.7. Case-specific definition procedure

Thus, models that are constructed following the above procedures are referred to as the *generic FE model* in this thesis. Below provides a summary of the steps that were followed each time to define a case-specific model:

i) Assign section thickness, h, to the panel component.

ii) Reposition all the parts above and below the blank according to the change in h.

iii) Position the upper and lower workheads according to the case-specific pin height requirement.

iv) Assign the case-specific parameters d_r, T_0, T, t_1, t_2, t, t_3 and t_4.

v) Run a pilot simulation to generate a part file (.prt) and from which retrieve the element numbers (NOEL) that correspond to the panel component.

vi) Assign the residual stress profiles to the retrieved NOEL via the user-defined subroutine SIGINI.

vii) Include in the input file (.inp) the following statement:
**Initial Conditions, type=Stress, user*

viii) Run the simulation using the updated input file.

In situations when the effect of residual stresses need not be considered, the simulation is run after step (iv).

CHAPTER 6.

MODELLING RESULTS & DISCUSSIONS

6.1. Introduction

The modelling results obtained using the generic FE model developed in Chapter 5 are presented and discussed in this chapter. The first section establishes the springback prediction accuracy of the FE model by making comparisons between the single curvature CAF tests' formed plate deflections and those simulated using the FE model. The validated FE model was then employed in the second section to showcase this thesis' research output by utilising altogether all the flexible form tool, the experimental techniques and modelling techniques developed in this thesis to produce accurately shaped panel components via CAF.

6.2. Single curvature forming test for model validation

6.2.1. Modelling input

Using the generic FE model and following the procedures outlined in Chapter 5 to define each case-specific problem by assigning initial deflections, plate thickness and a form tool span bending radius of 1200 mm, springback of the nine creep-age formed plates (Chapter 4) were all simulated under conditions that match their physically tested conditions.

Table 17 presents the variables assigned to describe the temperature and loading profiles of the simulations.

Table 17. Variables that describe the temperature and loading profiles of the forming simulations.

Variable	(Unit)	Assigned value
t_1	(h)	0.1
t_2	(h)	4
t	(h)	22
t_3	(h)	4
t_4	(h)	0.1
T_0	(K)	295.15
T	(K)	388.15

6.2.2. Results

Table 18 presents a comparison of the experimental and FE-simulated final deflections of the singly curved formed plates. On average, an absolute difference of 0.79±0.46 mm is recorded between the experimental and FE-simulated final plate deflections.

Table 18. Plate thickness and simulated final deflections of the singly curved formed plates.

#	Plate thickness (mm)	Final deflections (mm) at $y = 240$ mm		Absolute difference (mm)
		Experiment	Simulation	
1	3.20	3.27	2.46	0.81
2	3.26	3.76	2.66	1.10
3	3.40	5.22	4.35	0.87
4	4.88	4.99	3.53	1.46
5	5.30	4.91	3.66	1.25
6	5.31	2.53	1.82	0.71
7	8.09	3.57	4.23	0.66
8	8.20	4.51	4.63	0.12
9	8.20	4.35	4.44	0.09
			Average±SD	0.79±0.46

Figure 48 presents the results in Table 18 in the form of a bar chart. The variation of the FE-simulated deflections from one plate to another closely resembles those of the experimental results. As with the experimental results, no apparent correlation can be concluded between plate thickness and final deflections.

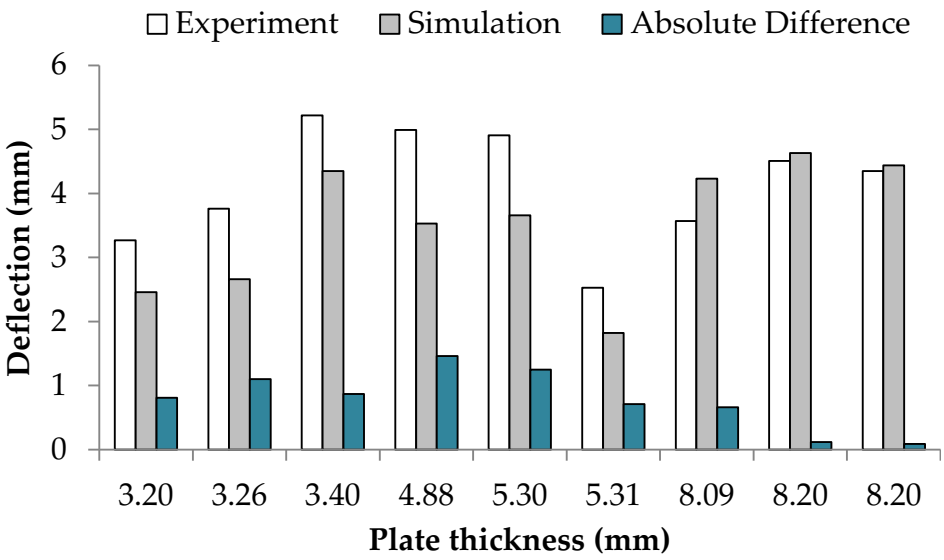

Figure 48. The experimental (white) and simulated (grey) final deflections and their absolute differences (turquoise).

6.2.3. Discussions

Figure 49 shows the weak correlation ($R^2 \sim 0$) between plate thickness and final plate deflection. As plate thickness increases but with the same amount of deformation imposed ($R = 1200$ mm), the material near the surfaces of the plate is effectively put under a higher level of stress during creep-ageing. A stronger positive correlation was therefore expected between plate thickness and final plate deflection. The weak correlation shown indicates the presence of other factors which influenced springback prediction.

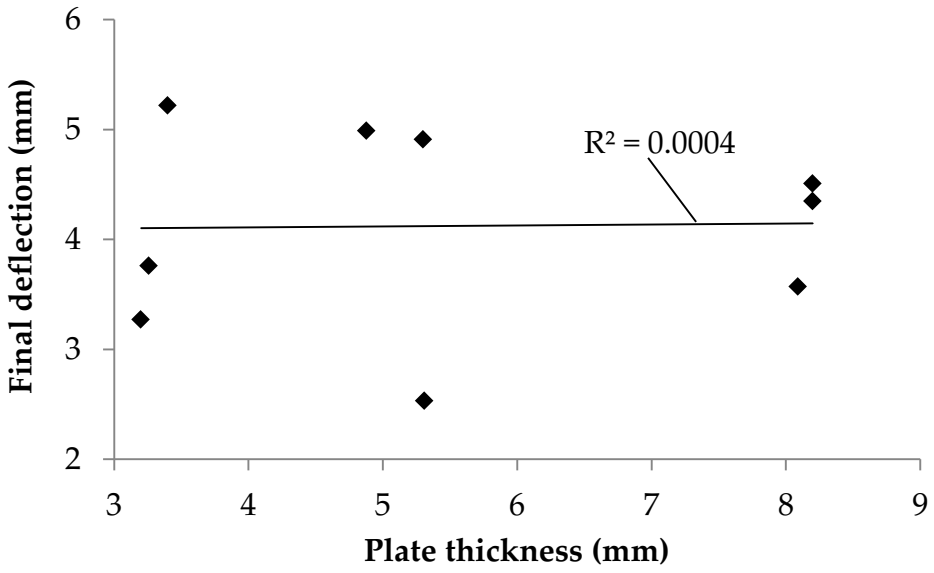

Figure 49. The weak correlation between plate thickness and experimental final plate deflection.

Figure 50 shows the positive correlation between the experimental results of initial and final deflections of the plates presented in Table 7 and Table 8 in Chapter 4. The correlation suggests that under the current CAF condition, initial deflections of plates play a more important role in springback prediction than the thickness of plate. The present results agree well with those presented in a paper recently published at the International Journal of Mechanical Sciences (Lam *et al.*, 2015d). In particular, the study found that conforming initial deflections (as is the case in this study) contribute positively to the final formed shape of plates.

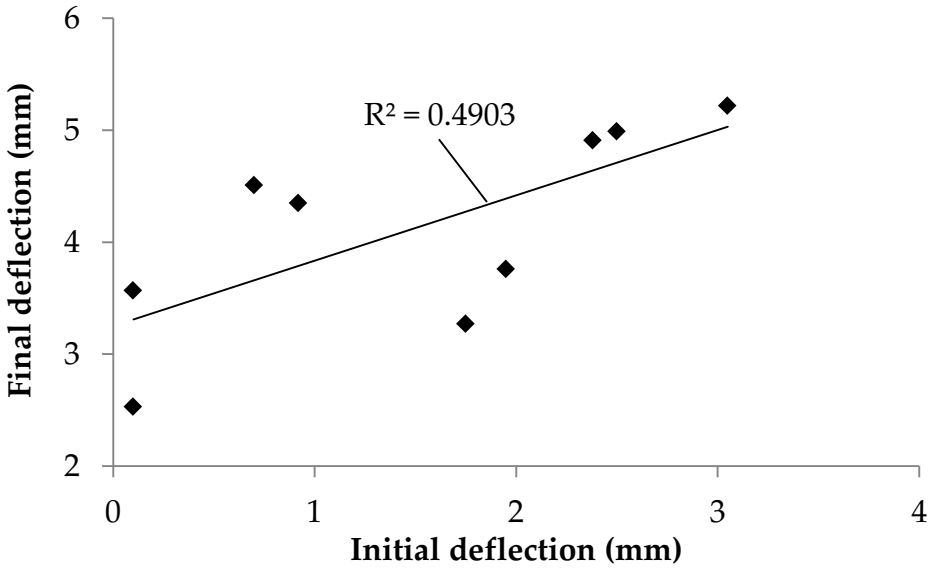

Figure 50. The positive correlation between initial deflection and experimental final plate deflection.

Figure 51 shows the negative correlation between initial plate deflection and plate thickness. As mentioned previously in Chapter 4, the thinner plates tend to have larger initial deflections than the thicker ones. The effects of initial deflection, as seen in Figure 50 and Figure 51, and plate thickness therefore counteract each other on their contributions to final plate deflection, leading to the unexpectedly weak correlation between plate thickness and final plate deflection observed in Figure 49.

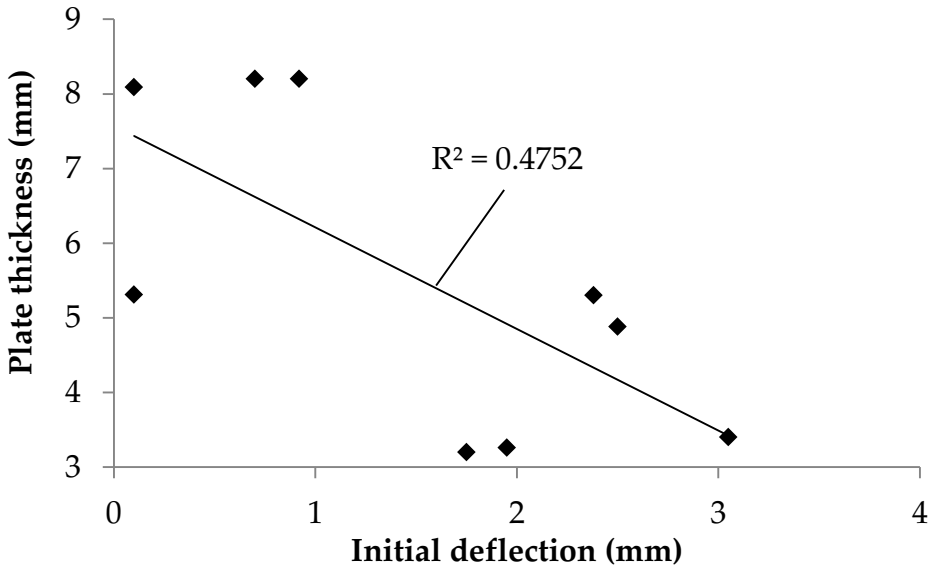

Figure 51. The negative correlation between plate thickness and initial deflection.

6.2.4. Summary

The material and process modelling techniques have been utilised to predict the springback of plates, creep-age formed using the proposed tooling and experimental techniques. The experimental and modelling procedures have been validated by making comparisons between experimental and FE-simulated final plate deflections. Despite the complicated relationships between initial deflections, residual stress effect and final plate deflections, an average absolute difference of 0.79±0.46 mm was achieved. This suggests that the developed modelling techniques can be used to accurately predict the final shape of plates formed using the proposed flexible CAF tool and experimental procedure.

6.3. Double curvature forming test for springback compensation

6.3.1. Integrated modelling techniques

Figure 52 shows a flowchart of the displacement-adjustment-(DA)-based integrated modelling procedure for springback compensation.

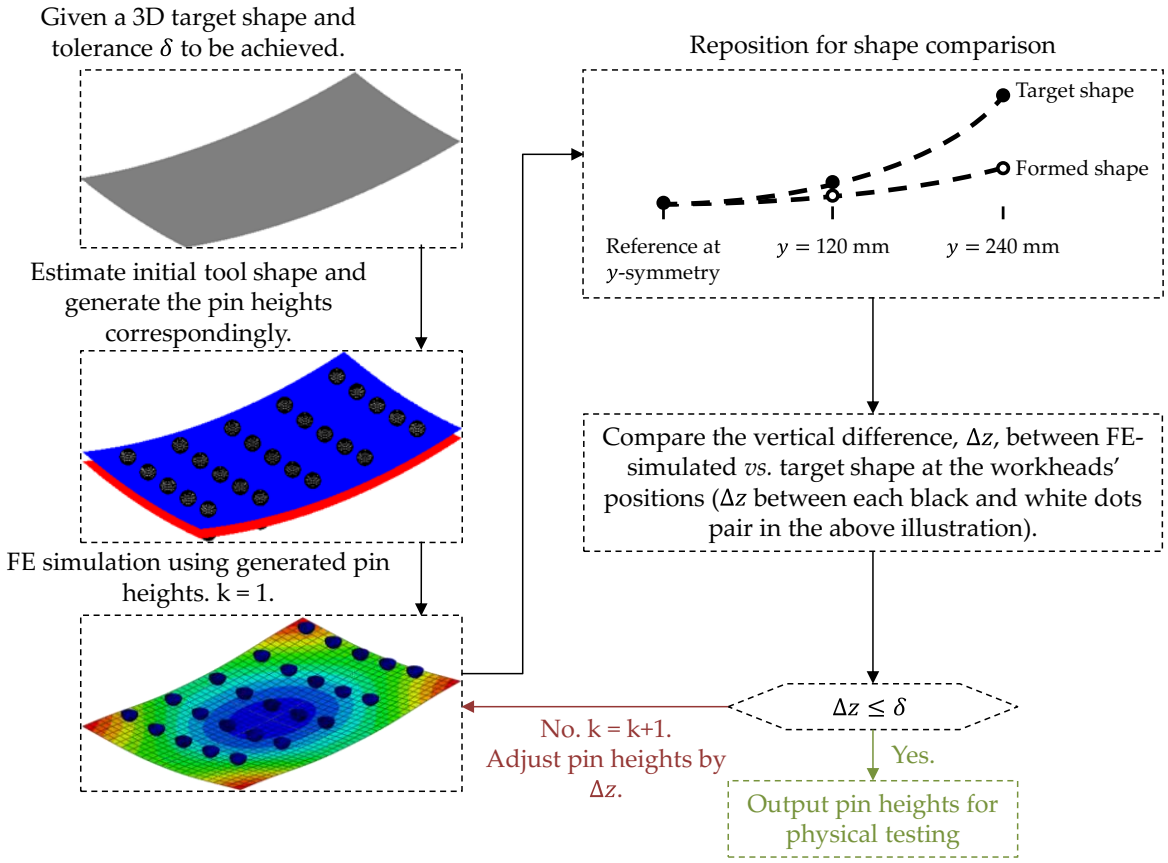

Figure 52. Flowchart of the displacement-adjustment-method-based integrated modelling procedure for springback compensation.

A flat panel is first given to be formed to a doubly curved target shape within a required tolerance of δ; defined as the absolute vertical difference between the target and formed panel shapes over the entire panel area. Because the DA method has been originally developed for plastic sheet metal forming processes (Gan and Wagoner, 2004), and as a result of the high springback feature of CAF, the conventional DA-practice of using target shape as the initial tool shape usually leads to little to no deformation in a large number of early-stage iterations. In order to reduce the amount of potential iterations and thus speed up the springback

compensation process, the required loaded panel shape was first estimated based on the analytical method validated by Lam and Lin (2014). The analytical method neglects the effects of residual stresses and initial distortions, assumes loading by pure bending and approximates the loaded panel shape with constant bending radii along both the span and chord directions.

Upon obtaining the estimated loaded panel shape, which is represented by a doubly curved 3D surface with constant radius of curvatures, the required pin heights are further calculated using vector and surface calculations. The set of initial pin heights are then inputted to the generic FE model for CAF process simulation with initial distortions of the plates taken into account. After the first iteration, the FE-formed shape is extracted and compared against the target shape. The absolute vertical difference, $|\Delta z|$, between the FE-simulated and target shape at each workhead's xy-position are compared. If $|\Delta z| > \delta$, the corresponding pin height is adjusted by the same amount of $|\Delta z|$ (in the direction opposite to that of the springback) before the next iteration of simulation is run. This springback compensation process is repeated until all $|\Delta z| \leq \delta$. Finally, a comparison is made between the continuous surfaces of the target and FE-simulated shapes and the final set of pin heights that satisfies maximum $|\Delta z| \leq \delta$ are logged and used to setup the flexible form tool for springback-compensated CAF tests to be conducted.

Following the above procedure, one double curvature CAF test were carried out on each plate thickness with a target to achieve $R_x = 4000$ mm, $R_y = 8000$ mm and $\delta = 0.2$ mm. Table 19 shows the loaded panel shape estimated for each plate for process initiation at $k = 1$.

Table 19. The loading radius of curvatures used to initiate the springback compensation process for each plate.

	R_x (mm)	R_y (mm)
3.1 mm	600	1000
5.3 mm	700	1340
8.2 mm	1000	2000

6.3.2. Results

6.3.2.1. Tool design modelling results

Figure 53 shows the reduction of the maximum $|\Delta z|$ throughout the springback compensation process. A relatively large maximum $|\Delta z|$ is observed in the first iterations due to the many assumptions involved in the analytical method. Nonetheless, three iterations were sufficient for all the FE-simulated plates to achieve the required maximum $|\Delta z| \leq 0.2$ mm. The modelling pin heights at $k = 3$ were then used to setup the flexible form tool for physical springback-compensated CAF tests.

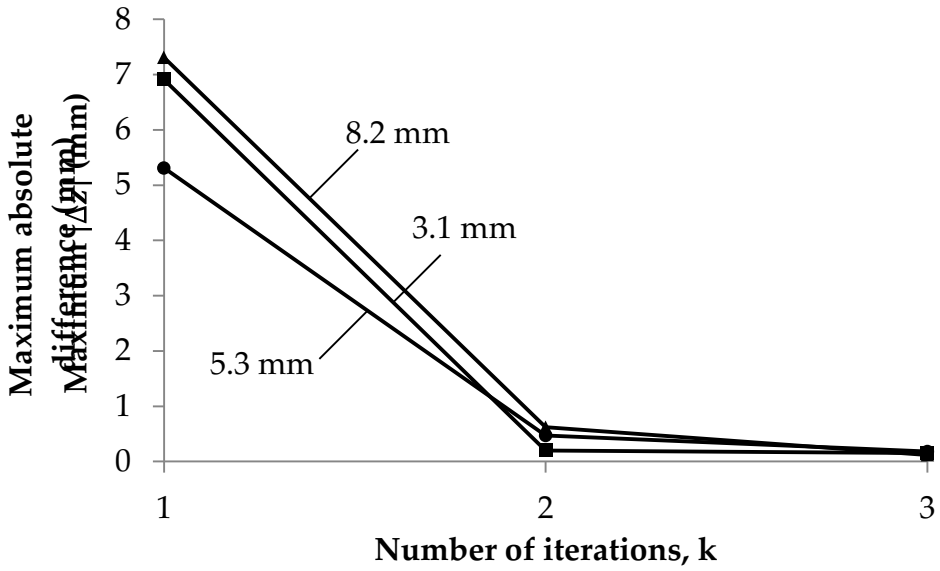

Figure 53. Maximum absolute vertical difference between the target and FE-simulated shapes over iterations of the springback compensation process.

6.3.2.2. Springback-compensated forming test results

Figure 54 shows the shape comparisons between the initial, target and creep-age formed shapes of the plates. For all the shapes, the z-deflection at $x = 120$ and $y = 240$ mm position is always set to zero as the reference point. The three plates all have a varying degree of initial distortions with the z-deflections gradually increases with decreasing x and y toward the plate centre until a maximum deflection is reached at $x = y = 0$ mm. The final formed shapes of the plates also follow the same trend.

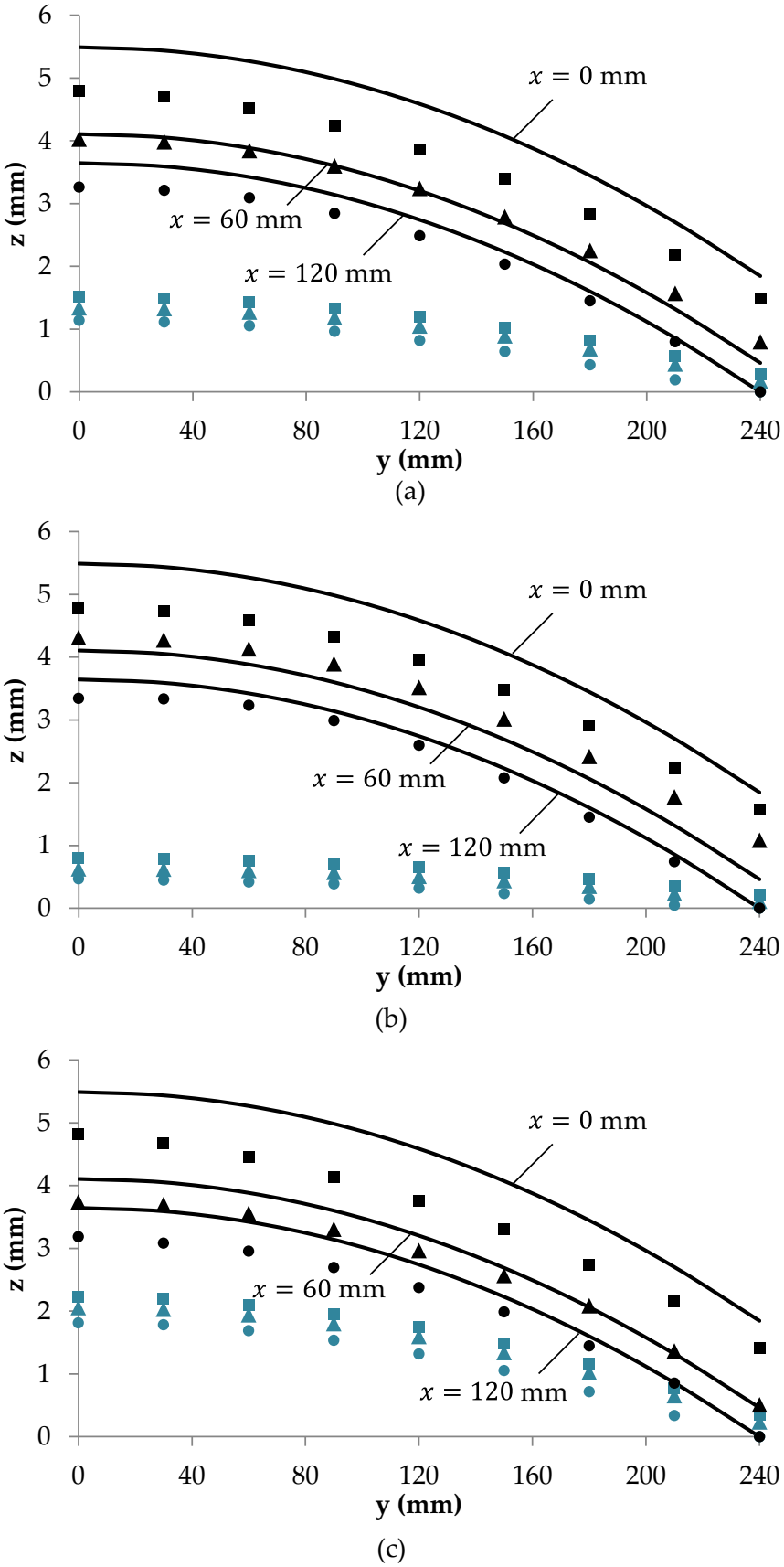

Figure 54. Comparison of the initial shape (turquoise markers), target shape (solid lines) and the shape of the formed plates (black markers) for (a) the 3.1, (b) 5.3 and (c) 8.2 mm thick plates.

Table 20 summarises the maximum z and the maximum $|\Delta z|$ attained by each plate. The maximum z has an average of 4.80 ± 0.02 mm and shows a good accuracy when compared with the target shape of $R_x = 4000$ mm and $R_y = 8000$ mm, which has a maximum z of 5.49 mm. The final deflections of the plates formed via the present procedure are consistently smaller than that of the target shape. This may be attributed to the concept of the DA method where the plate is only further bent until the optimising parameter ($|\Delta z|$ in this case), has reached within the zone of tolerance, δ. Finally, the average 0.81 ± 0.14 mm of maximum $|\Delta z|$ value also shows good consistency with the 0.79 ± 0.46 mm recorded from the model validation results.

Table 20. The maximum deflection and maximum absolute vertical difference from target shape attained by the 3.1, 5.3 and 8.2 mm plates.

Plate thickness (mm)	Maximum z (mm)	Maximum $\|\Delta z\|$ (mm)
3.1	4.80	0.75
5.3	4.78	0.71
8.2	4.81	0.97

6.3.3. Summary

The validated model has been integrated with the DA-method and used to model springback-compensated tool designs. Given a target shape to be achieved by three plates of different thicknesses, the initial tool shape was first estimated for each plate. The estimated tool shape was then used to initiate the iterative process of springback compensation with the plates' initial distortions and typical residual stress fields taken into account. The required tolerance of 0.2 mm vertical deflections was achieved by all the FE-simulated plates within three iterations. Using the springback-compensated tool designs to perform physical CAF tests, an average 0.81 ± 0.14 mm of maximum absolute vertical difference from the target shape was achieved.

The springback compensation test results show that the tooling, experimental and modelling techniques developed in this thesis can be put together and used to model the final deflection of plates formed via CAF to a remarkable accuracy. The

accuracy of the springback compensation test results summarises the outcome of this thesis. In particular, it demonstrates the predictive accuracy that can now be achieved for springback-compensated CAF tests performed in a research laboratory environment with the aid of the integrated modelling techniques developed in this thesis.

CHAPTER 7.

SUMMARY & FUTURE WORK

7.1. Summary

CAF is a well-established technique for forming extra-large integrally stiffened aluminium panels and the problem of springback hinders its wider industrial application. In order to overcome this ongoing challenge, the application of CAF must be made available to a greater range of alloys. This research adopts a flexible approach by integrating the concept of springback compensation to tooling design and process modelling. The development of ad-hoc experimental and modelling techniques to accurately shape panel components via CAF is presented in this thesis.

- The creep-ageing behaviour of aluminium alloy 7B04-T651 has been experimentally studied using creep-ageing and tensile tests. The test results have been applied to determine a CAF material model for the alloy under the given CAF condition.
- A novel flexible sparse-point tool has been proposed. This tool design attempts to close the existing technology gap in the field of flexible form tools for shaping extra-large components via CAF. A laboratory-scale prototype has been made and applied to the experimentation work performed in this thesis.

- The ad-hoc experimental and modelling techniques have been integrated and the springback predictive ability of the CAF process model has been validated. Despite the complicated relationships observed between initial deflections, residual stress effect and final plate deflections, the validation results showed an average absolute difference of 0.79±0.46 mm between the experimental and simulated final plate deflections.
- The CAF process model with confirmed springback predictive ability has been integrated with the concept of springback compensation to model springback-compensated tool shapes. Using the modelled tool shapes to perform CAF tests produced plates that have an average 0.81±0.14 mm of maximum absolute vertical difference from the target shape within three iterations.

7.2. Future Work

The springback predictive ability of the FE process model is dependent upon a number of input parameters and conditions. For instance, the use of a typical residual stress field in the current model is a limitation that needs to be further investigated. A possible method to overcome this limitation is to consider the effect of the original manufacturing process and processing conditions of the workpiece before they are received for the CAF stage. This can be further extended to the development of constitutive models or multiple process models that consider the effect of multi-stage manufacturing processes on residual stress fields, and eventually their influence on the springback of panel components in CAF.

The flexible tool design proposed in this thesis utilises sparsely spaced controlling points to create an equivalent forming surface with fewer supporting points, thereby achieving part-count reduction and lightweighting of the forming tool. During CAF, internal stresses of the panel relax and shape deviation may occur at regions where there lack support from forming pins. The spacing between

forming pins can therefore influence the behaviour of dynamic stress relaxation and creep accumulation of the panel component being formed. Further research may look into the effect of such shape deviation on the change in springback. The maximum allowable spacing between neighbouring forming pins can be quantified for any given shape, maximising the lightweighting potential of the proposed forming tool.

A major disadvantage of CAF is the long processing hours it requires to manufacture a component due to its utilisation of time-temperature-dependent stress relaxation and creep. Recent research has begun looking into the possibility of introducing additional energy sources, such as vibrational energy, to the CAF process with an aim to accelerate the mechanisms of stress relaxation and precipitation in CAF. Although further research is yet to confirm the mechanisms and results behind them, research into the design of more advanced tooling that can allow the introduction of vibration energy to the panel component being formed may also be a useful research direction.

REFERENCES

Abaqus (2011) *Abaqus 6.11 Theory Manual*. Dassault Systèmes Simulia, Providence, RI, USA.

ACARE (2010) *Aeronautics and air transport research success stories and benefits beyond aviation.* In: Handover-Document, 28th November 2011, Brussels, Belgium. [url: accessed 28th October 2014].

Adachi T, Kimura S, Nagayama T, Takehisa H and Shimanuki M (2004) Age forming technology for aircraft wing skin. *Materials Forum*, 28, 202 – 7.

Ageform (n.d.) *Ageformable panels for commercial aircraft.* [url: accessed 28th October 2014].

Airbus (2011) *Airbus in Illescas delivers first A350 XWB Wing Lower Cover to Airbus in Broughton.* [url: accessed 26th October 2014].

Air France (2011) *The Air France A380: Air France Airbus A380 Landing.* [url: accessed 15th July 2015].

Ansted EW (1892) *Machine for bending and forming springs.* Patent US 483094.

ATL Technology Licensing (2014) Creep Forming. [Video] YouTube. [url: accessed 4th June 2015].

Austal (n.d.) *Aluminium Hull Structure in Naval Applications*. Austal Shipyards: Australia and USA. [url: accessed 30th October 2014].

Benham PP, Crawford RJ and Armstrong CG (1999) *Mechanics of Engineering Materials*. 2nd Edition. Longman. p.464.

Bhushan B (2000) *Modern Tribology Handbook, Two Volume Set.* Boca Raton, CRC Press.

Bilstein RE (1980) *Stages to Saturn: A technological history of the Apollo/Saturn launch vehicles.* Washington, D.C., NASA History Office. [url: accessed 28th October 2014].

Boeing (n.d.) *History: Saturn V Moon Rocket*. Boeing. [url: accessed 29th October 2014].

Bonnafe JP, Destandau C and Fougeras J (1996) Age creep forming process modelling and experimentation in aluminium alloys – Validation on Ariane 5 main tank bulkheads segments. *Proceedings of the 4th European Conference on Residual Stresses, ECRS4*, Cluny, France, June 1996, 823 – 828.

Borradaile JB (1999) Future aluminium technologies and their application to aircraft structures. *New Metallic Materials for the Structure of Aging Aircraft*, Corfu, Greece, 19th to 20th April 1999. [url: accessed 13th November 2014].

Bourdin JP, Bonnafe JP, Delmotte J, Grosjean E and Roelandt JM (1999) Shape and thickness optimization of an aeronautical structure manufactured using age creep forming process. In: Batoz JL, Chedmail P, Cognet G and Fortin C (eds.) *Integrated Design & Manufacturing in Mechanical Engineering '98, Proceedings of the 2nd IDMME Conference*, 27th to 29th May 1998, Compiègne, France, 315 – 322. [doi].

Brinksmeier E, Cammett JT, König W, Leskovar P, Peters J and Tönshoff HK (1982) Residual stresses – Measurement and causes in machining processes. *CIRP Annals – Manufacturing Technology*, 31(2), 491 – 510.

Burchitz IA (2008) *Improvement of Springback Prediction in Sheet Metal Forming*. Report number: MC1.02121. [url: accessed 18th June 2013].

Caltech Engineering Services (2012) 4-Point Bend SSC Test. [url: accessed 12th November 2012].

Denkena B, Boehnke D and de Leon L (2008) Machining induced residual stress in structural aluminium parts. *Production Engineering*, 2(3), 247 – 253. [doi].

Dirikolu MH and Akdemir E (2004) Computer aided modelling of flexible forming process. *Journal of Materials Processing Technology*, 148(3), 376 – 381. [doi].

Dranevitan (2011) *Production Processes of the Shinkansen Train*. [url: accessed 8th June 2015].

Eberl F, Gardiner S, Campanile G, Surdon G, Venmans M and Prangnell P (2006) *Leading the way with advanced aluminium solutions for aerospace structures.* [Presentation] Aeronautics Days, Vienna, Austria, 19th to 21st June.

Eberl F, Gardiner S, Campanile G, Surdon G, Venmans M and Prangnell P (2008) Ageformable panels for commercial aircraft. *Proceedings of the Institution of Mechanical Engineers, Part G: Journal of Aerospace Engineering*, 222, 873 – 886. [doi].

Flightglobal (2011) *Aerolia, once Airbus, delivers nose section for first A350 (Update1).* [url: accessed 23rd Aug 2014].

Foster AD, Mohamed MS, Lin J and Dean TA (2009) An investigation of lubrication and heat transfer for a sheet aluminium heat, form-quench (HFQ) process. *Steel Research International*, 79, 113 – 119.

Friese A, Lohmar J and Wustefeld F (2006) Current applications of advanced peen forming implementation. In: Wagner L (ed.) *Proceedings of the 8th International Conference on Shot Peening, ICSP-8,* 16th to 20th September 2002, Garmisch-Partenkirchen, Germany. [doi].

Gan W and Wagoner RH (2004) Die design method for sheet springback. *International Journal of Mechanical Sciences*, 46(7), 1097 – 1113.

General Dynamics Electric Boat (n.d.) Image Library – Virginia Class. [url: accessed 25th April 2015].

Guines D, Gavrus A and Ragneau E (2008) Numerical modeling of integrally stiffened structures forming from creep age forming technique. *International Journal of Material Forming*, 1(1), 1071 – 1074. [doi].

Haas, E.G. and Kesselman, M. (1996) *Adjustable form die.* Patent US 5546784.

Hess F (1931) *Process and apparatus for manufacturing anatomically accurate individual foot supports for shoes*. Patent US 1826783.

Ho KC, Lin J and Dean TA (2004a). Modelling of springback in creep forming thick aluminum sheets. *International Journal of Plasticity*, 20(4 – 5), 733 – 751.

Ho KC, Lin J and Dean TA (2004b). Constitutive modelling of primary creep for age forming an aluminium alloy. *Journal of Materials Processing Technology*, 153 – 154, 122 – 127.

Holman MC (1989) Autoclave age forming large aluminum aircraft panels. *Journal of Mechanical Working Technology*, 20, 477 – 488. [doi].

Hornauer KP and Kohler W (1990) Development of the peen forming process for spherical shaped components. In: *Proceedings of the 4th International Conference on Shot Peening, ICSP-4,* Tokyo, Japan, 585 – 594. [url: accessed 28th October 2014].

Huang L, Wan M, Chi C and Ji X (2007) FEM Analysis of Spring-backs in Age Forming of Aluminum Alloy Plates. *Chinese Journal of Aeronautics*, 20(6), 564 – 569. [doi].

Huang S, Zeng Y and Huang X (2009a) FE analysis of creep age forming for aluminium alloy 2324. *Journal of Plasticity Engineering*, 16(4), 129 – 133. [doi].

Huang X, Zheng Y and Huang S (2009b) Experimental research on the creep age forming for aluminium alloy 2324. *Journal of Plasticity Engineering*, 16(3), 136 – 139.

Huang X, Sun J, Li J, Han X and Xiong Q (2013) An experimental investigation of residual stresses in high-speed end milling 7050-T7451 aluminium alloy. *Advances in Mechanical Engineering*, 2013, Article ID 592659, 7 pages. [doi].

Idem K and Peddieson J (2005) Simulation of the Age Forming Process. *Journal of Manufacturing Science and Engineering*, 127, 165 – 172. [doi].

Ignis (2006) *Ariane 5 Le Bourget FRA 001*. [url: accessed 25th April 2015].

Inforzato DJ, Costa PR Jr and Fernandez FF (2012) Creep-age forming of AA7475 aluminum panels for aircraft lower wing skin application. *Material Research*, 15(4), 596 – 602. [doi].

Islamoff II (1965) *Metal-forming techniques.* Washington, D.C., NASA Technology Utilization Division. [url: accessed 28th October 2014].

Jeshvaghani RA, Shahverdi HR and Hadavi SMM (2012) Investigation of the age hardening and operative deformation mechanism of 7075 aluminum alloy under creep forming. *Materials Science and Engineering A*, 552, 172 – 178. [doi].

Jeunechamps PP, Ho KC, Lin J, Ponthot JP and Dean TA (2006) A closed form technique to predict springback in creep age-forming. *International Journal of Mechanical Sciences*, 48(6), 621 – 629.

JPRail (2014) *What is Shinkansen Bullet Train*. [url: accessed 8th May 2015].

JRLZAGS03 (2009) *Airbus A380 – Wing Construction – HD*. [Video] YouTube. [url: accessed 18th August 2014].

Kebir H, Roelandt JM, Delmotte J and Bonnafe JP (2000) Optimization of space structures manufactured using age creep forming process. In: *European Congress on Computational Methods in Applied Sciences & Engineering, ECCOMAS 2000*, 11th to 14th September, Barcelona, Spain. [url: accessed 03rd June 2015].

Kim H and Koç M (2008) Numerical investigations on springback characteristics of aluminum sheet metal alloys in warm forming conditions. *Journal of Materials Processing Technology*, 204, 370 – 383. [doi].

Kowalewski ZL, Hayhurst DR and Dyson BF (1994) Mechanisms-based creep constitutive equations for an aluminium alloy. *Journal of Strain Analysis*, 29(4), 309 – 316. [doi].

Lam ACL, Chandaria V, Patel R, Simmonds J and Zou J (2011) *Material characterisation and finite element modelling of rubber, PU, EVA and SALi as energy absorbing materials.* MEng project report. Imperial College London.

Lam ACL and Lin J (2014) A validated analytical solution for the two-dimensional bending of aluminium plates under creep-ageing conditions. *Key Engineering Materials*, 622 – 623, 1107 – 1116. [doi].

Lam ACL, Shi Z, Yang H, Wan L, Davies CM, Lin J and Zhou S (2015a) Creep-age forming AA2219 plates with different stiffener designs and pre-form age conditions: Experimental and finite element studies. *Journal of Materials Processing Technology*, 219, 155 – 163. [doi / url].

Lam ACL, Shi Z, Lin J, Huang X, Zeng Y and Dean TA (2015b) A method for designing lightweight and flexible creep-age forming tools using mechanical splines and sparse controlling points. *International Journal of Advanced Manufacturing Technology*, 80(1 – 4), 361 – 372. [doi / url].

Lam ACL, Shi Z, Huang X, Zeng Y, Li Z and Lin J (2015c) *A die mechanism, an apparatus, and a method for shaping a component for creep-age forming.* Patent Application GB 1502734.5. Filed 18th February.

Lam ACL, Shi Z, Lin J and Huang X (2015d) Influences of residual stresses and initial distortion on springback prediction of 7B04-T651 aluminium plates in creep-age forming. *International Journal of Mechanical Sciences*, 103, 115 – 126. [doi / url].

Lamartin GF (2004) *Model designation of military aerospace vehicles*. U.S. Department of Defense. Report number: DoD 4120.15-L. [url: accessed 28th October 2014].

Leuschner R, Palm F, Schubert T, Weissgaerber T and Kieback B (2010) Scalmalloy® = A unique high strength AlMgSc type material concept processed by innovative technologies for aerospace applications. In: European Powder Metallurgy Association. *Proceedings of the PM2010 Powder Metallurgy World Congress,* 10th to 14th October 2010, Florence, Italy. pp. 273 – 280. [url: accessed 1st November 2014].

Levers A (2003) Jumbo Processes. *Journal of Manufacturing Engineer*, 82(3), 42 – 45.

Levers A (2008a) *Creep forming a metallic component*. Patent US 7322223 B2.

Levers A (2008b) *Aircraft component manufacturing tool and method.* Patent EP 1581357 B1.

Levers A (2010) Broughton: From Wellington Bombers to the A380. *International Journal for the History of Engineering & Technology*, 80(1), 55 – 79. [doi].

Li B, Lin J and Yao X (2002) A novel evolutionary algorithm for determining unified creep damage constitutive equations. *International Journal of mechanical Sciences*, 44(5), 987 – 1002.

Li C, Wan M, Wu X-D and Huang L (2010) Constitutive equations in creep of 7B04 aluminum alloys. *Materials Science and Engineering: A*, 527(16 – 17), 3623 – 3629.

Li D, Zhao H, Zhu M, Li X, Sang Y, Luo H, Xu Y and Zhang Y (2013) *Autoclave-based creep age forming flexible frock*. Patent CN 101774274 B.

Li Z, Xiong B, Zhang Y, Zhu B, Wang F and Liu H (2008) Microstructural evolution of aluminium alloy 7B04 thick plate by various thermal treatments. *Transactions of Nonferrous Metals Society of China*, 18, 40 – 45. [doi].

Lin J and Yang J (1999) GA-based multiple objective optimisation for determining viscoplastic constitutive equations for superplastic alloys. *International Journal of Plasticity*, 15(11), 1181 – 1196.

Lin J, Ho KC and Dean TA (2006) An integrated process for modelling of precipitation hardening and springback in creep age-forming. *International Journal of Machine Tools and Manufacture*, 46(11), 1266 – 1270.

Lo R, Zinner W and Pernpeintner R (2007) *Space Transportation Systems – Propulsion and Structures*. [Presentation] CEAS European Air & Space Conference, Berlin, Germany, 10th – 13th September. [url: accessed 26th October 2014].

Mahendra B, Ankanna B, Tirupathi Reddy K and Ravichandra M (2013) Modeling and structural analysis of a pressure hull under dynamic load. *International Journal of Modern Engineering Research*, 3(6), 3552 – 3559.

Marciniak Z, Duncan JL and Hu SJ (2002) *Mechanics of sheet metal forming*. Bytterworth-Heinemann. Oxford.

McMaster University (2007) *Our Research – Formability Test: Cantilever Bend Test.* [url: accessed 9th November 2012].

MiX (1971) Diagram of Saturn V Launch Vehicle. *Marshall Space Flight Center's Image Archive.* [url: accessed 29th October 2014].

Moulton R (1996) *Robert Bicycle Repair History.* [url: accessed 19th October 2014].

MT Aerospace (n.d.) *Shaping Technologies*, MT Aerospace, Augsburg, Germany. [url: accessed 26th October 2014].

Munroe J, Wilkins K and Gruber M (2000) *Integral Airframe Structures (IAS) – Validated feasibility study of integrally stiffened metallic fuselage panels for reducing manufacturing costs.* Boeing Commercial Airplane Group, Seattle, Washington. Report number: NASA/CR-2000-209337.

Narasimhan N and Lovell M (1999) Predicting springback in sheet metal forming: an explicit to implicit sequential solution procedure. *Finite Elements in Analysis and Design*, 33(1), 29 – 42. [doi].

Nardiello JA, Christ RJ and Papazian JM (2000) *Block-set form die assembly.* Patent US 6053026.

National Shot Peening (n.d.) *Peening Gallery*. [url: accessed 19th October 2014].

Pacchione M and Fideu P (2014) *Method for producing a structural component, and structural component*. Patent US 20140087143 A1.

Park JW, Hong YS and Lim SH (2000) *Dieless forming apparatus.* Patent US 6151938.

Peddieson J and Buchanan G (1990) Mathematical modelling of an age-forming process. *Mathematical & Computer Modelling*, 14, 1057 – 1060. [doi].

Petit-Renaud F (2006) Optimization of the shot peening parameters. In: Wagner L (ed.) *Proceedings of the 8th International Conference on Shot Peening, ICSP-8,* 16th to 20th September 2002, Garmisch-Partenkirchen, Germany. [doi].

Pinson GT (1980) *Apparatus for forming sheet metal*. Patent US 4212188.

Premium AEROTEC (n.d.) *Manufacturing*. [url: accessed 23rd May 2015].

SAE International (2008) *Europe investigating new aerospace press-forming possibilities.* [url: accessed 6th November 2012].

Sallah M, Peddieson Jr J and Foroudastan S (1991) A mathematical model of autoclave age forming. *Journal of Materials Processing Technology,* 28(1 – 2), 211 – 219.

SpaceX (2010) *COTS Demonstration Flight 1.* [url: accessed 26th October 2014].

Tang ZT, Liu ZQ, Pan YZ, Wan Y and Ai X (2009) The influence of tool flank wear on residual stresses induced by milling aluminium alloy. *Journal of Materials Processing Technology*, 209(9), 4502 – 4508. [doi].

Triumph Group (2010) *Wings: Triump Aerostructures – Vought Aircraft Division – Red Oak*. [url: accessed 28th October 2014].

Wagoner R and Li M (2007) Simulation of springback: Through-thickness integration. *International Journal of Plasticity*, 23(3), 345 – 360.

Wang Y, Deng Y, Kang J and Zhang J (2014) Effects of vibration on creep age forming of 7055 aluminium alloy. *Journal of Aeronautical Materials*, 34(3), 81 – 85. [doi].

Wustefeld F, Kittel S, Kopp R, Linnemann W, Werner G, Durr W and Kohler W (1996) ¼ Tank bulkhead segment for the European Ariane 5. In: *Proceedings of the 6th International Conference on Shot Peening, ICSP-6*, San Francisco, CA, USA, 87 – 94. [url: accessed 28th October 2014].

Yang H (2013) *Creep Age Forming Investigation on Aluminium Alloy 2219 And Related Studies*. PhD Thesis. Imperial College London.

Yang H, Davies CM, Lin J and Dear JP (2013) Prediction and assessment of springback in typical creep age forming tools. *Proceedings of the Institution of Mechanical Engineers, Part B: Journal of Engineering Manufacture*, 227(9), 1340 – 1348.

Yiyuan (2013) *CRH380A-6016 20130211*. [url: accessed 27th April 2015].

Young KA, Nervi S and Szabo B (2005) *Machining-induced residual stress and distortion*. SAE Technical Paper. [doi].

Zeng Y and Huang X (2008) Forming technologies of large integral panel. *Acta Aeronautica et Astronautica Sinica*, 29(3), 721 – 727.

Zhan L, Lin J and Dean TA (2011a) A review of the development of creep age forming: Experimentation, modelling and applications. *International Journal of Machine Tools & Manufacture*, 51, 1 – 17. [doi].

Zhan L, Lin J, Dean TA and Huang M (2011b) Experimental studies and constitutive modelling of the hardening of aluminium alloy 7055 under creep age forming conditions. *International Journal of Mechanical Sciences,* 53(8), 595 – 605.

Zhan L, Li Y, Huang M and Zheng M (2012) Constitutive equation describing creep ageing of 2124 aluminium alloy. *Journal of South China University of Technology (Natural Science Edition)*, 40(4), 107 – 111.

Zhan L, Yan S, Yang Y, Huang M, Shen W and Zhao X (2014) A research on the creep age forming of 2524 aluminium alloy: springback, mechanical properties and microstructures. *Advances in Mechanical Engineering*, Article ID: 707628. [doi].

Zhang J, Deng Y and Zhang X (2013a) Constitutive modeling for creep age forming of heat-treatable strengthening aluminum alloys containing plate or rod shaped precipitates. *Materials Science and Engineering: A*, 563, 8 – 15.

Zhang J, Deng Y, Li S, Chen Z and Zhang X (2013b) Creep age forming of 2124 aluminium alloy with single/double curvature. *Transactions of Nonferrous Metals Society of China*, 23(7), 1922 – 1929.

Zhang P, Lin J and Balint D (2012) *OPT-CAF: the optimisation tool for calibrating creep constitutive equations.* Department of Mechanical Engineering, Imperial College London.

APPENDIX A.

COMMUNICATION OF RESEARCH

A1. Patent

Lam ACL, Shi Z, Huang X, Zeng Y, Li Z and Lin J (2015) *A die mechanism, an apparatus, and a method for shaping a component for creep-age forming.* Patent Application GB 1502734.5. Filed 18th February.

A2. Journal articles

Lam ACL, Shi Z, Huang X, Yang Y, Zeng Y and Lin J (2015) Material modelling and its application to creep-age forming of aluminium alloy 7B04. *Manufacturing Review*, 2, 19. [doi].

Lam ACL, Shi Z, Lin J and Huang X (2015) Influences of residual stresses and initial distortion on springback prediction of 7B04-T651 aluminium plates in creep-age forming. *International Journal of Mechanical Sciences,* 103, 115 – 126. [doi / url].

Lam ACL, Shi Z, Lin J, Huang X, Zeng Y and Dean TA (2015) A method for designing lightweight and flexible creep-age forming tools using mechanical splines and sparse controlling points. *International Journal of Advanced Manufacturing Technology,* 80(1 – 4), 361 – 372. [doi / url].

Lam ACL, Shi Z, Yang H, Wan L, Davies CM, Lin J and Zhou S (2015) Creep-age forming AA2219 plates with different stiffener designs and pre-form age conditions: Experimental and finite element studies. *Journal of Materials Processing Technology*, 219, 155 – 163. [doi / url].

Lam ACL and Lin J (2014) A validated analytical solution for the two-dimensional bending of aluminium plates under creep-ageing conditions. *Key Engineering Materials*, 622 – 623, 1107 – 1116. [doi].

A3. Conference papers

Lam ACL, Shi Z, Huang X, Yang Y, Zeng Y and Lin J (2015) Material modelling for creep-age forming of aluminium alloy 7B04. *MATEC Web of Conferences*, 21, Article number: 12006. In: Qin Y, Dean TA, Lin J, Yuan SJ and Vollertsen F (eds.) *Proceedings of the 4th International Conference on New Forming Technology, ICNFT 2015*, Glasgow, Scotland, UK, 6th to 9th August 2015. [doi].

Yang Y, Lam ACL, Shi Z, Lin J and Said R (2015) Constitutive modelling of creep-ageing behaviour of peak-aged aluminium alloy 7050. *MATEC Web of Conferences*, 21, Article number: 12008. In: Qin Y, Dean TA, Lin J, Yuan SJ and Vollertsen F (eds.) *Proceedings of the 4th International Conference on New Forming Technology, ICNFT 2015*, Glasgow, UK, 6th to 9th August 2015. [doi].

A4. Invited presentations

Lam ACL (2015) *Modelling of residual stresses and initial distortion for creep-age forming processes*. Imperial-AVIC Biannual Workshop, AVIC Centre for Structural Design and Manufacture, London, UK, 15th June.

Lam ACL (2014) *Recent progress on the development of a modular and flexible sparse-point tool for creep-age forming*. Imperial-AVIC Biannual Workshop, AVIC Centre for Structural Design and Manufacture, London, UK, 1st December.

Lam ACL (2014) *A validated analytical solution for the two-dimensional bending of aluminium plates under creep-ageing conditions.* 15th International Conference on Metal Forming, University of Palermo, Palermo, Italy, 21st to 24th September.

Lam ACL (2014) *Part-count reduction for a flexible creep-age forming tool design*. Imperial-AVIC Biannual Workshop, AVIC Centre for Structural Design and Manufacture, London, UK, 14th July.

Lam ACL (2014) *Modularity in tooling design for making large airframe panels*. Metal Forming and Materials Modelling Group Seminar, Imperial College London, London, UK, 2nd July.

Lam ACL (2013) *Creep-age forming tool innovation*. Imperial-AVIC Biannual Workshop, AVIC Centre for Structural Design and Manufacture, London, UK, 11th November.

Lam ACL (2013) *A reconfigurable tool for springback compensation in creep-age forming*. Visit of BAMTRI's Deputy Chief Engineer Shuili Gong and the Academician of the Chinese Academy of Engineering Qiao Guan, AVIC Centre for Structural Design and Manufacture, London, UK, 27th June.

Lam ACL (2013) *Innovative tooling techniques for creep-age forming*. Visit of FAI's Vice Chief Designer Shengang Tan, AVIC Centre for Structural Design and Manufacture, London, UK, 21st March.

A5. Deliverable reports

Lam ACL and Lin J (2015) *Creep-Age Forming Tool Innovation*. Department of Mechanical Engineering, Imperial College London. Report number: AVIC-SDM-2015-09-11-LAM.

Lam ACL and Lin J (2015) *Creep-Age Forming Tool Innovation*. Department of Mechanical Engineering, Imperial College London. Report number: AVIC-SDM-2015-03-16-LAM.

Lam ACL and Lin J (2014) *Creep-Age Forming Tool Innovation*. Department of Mechanical Engineering, Imperial College London. Report number: AVIC-SDM-2014-09-14-LAM.

Lam ACL and Lin J (2014) *Creep-Age Forming Tool Innovation*. Department of Mechanical Engineering, Imperial College London. Report number: AVIC-SDM-2014-03-05-LAM.

Lam ACL and Lin J (2013) *Creep-Age Forming Tool Innovation*. Department of Mechanical Engineering, Imperial College London. Report number: AVIC-SDM-2013-09-05-LAM.

Lam ACL and Lin J (2013) *Creep-Age Forming Tool Innovation*. Department of Mechanical Engineering, Imperial College London. Report number: AVIC-CDM-2013-03-14-LAM.

APPENDIX B.

STRESS ANALYSIS FOR OPTIMAL FORMING TOOL CONFIGURATION

B1. Objective

Conventional flexible tools require the use of tightly packed forming pins to create a continuous forming surface, and as discussed in Chapter 2, such tools are heavy and unfavourable to CAF processes. Driven by the lightweight tooling requirement of CAF, a flexible forming tool was designed and manufactured (Chapter 3) with its practical use demonstrated (Chapter 6).

The tooling design concept is based on the utilisation of flexible splines and sparsely spaced forming pins, which offers a possible lightweight flexible solution for manufacturing extra-large components at low cost. Since such tools were not available until this research, investigations on deformation characteristics of components in sparse-point tooling have not been found in literature, and even more so when it comes to their use in CAF.

Using FE analysis, this appendix presents an investigation of the influence of performing CAF operations in sparse-point tools under various forming conditions on the quality of creep-age formed parts. Since components undergo viscoplastic deformation during CAF, an emphasis is given to the time evolutions of internal

stress states of components during forming, and eventually their effects on their final formed shape. The results from these analyses will be used at the end to provide recommendations to the optimal tooling configuration for the laboratory-scale forming tool used in this research.

B2. Design of stress analyses

The analyses in this appendix follow a one-condition-at-a-time principle whereby the effect of each forming condition is assessed individually. Detail analysis on the potential effects due to the interactions between these conditions is beyond the scope of this study.

In order to investigate how different tooling configurations could affect deformation of components in CAF, the flexible splines and elastomeric sheet were removed from the generic FE model (Chapter 5) one-at-a-time with their effects investigated. Table B1 presents the tooling configurations that are selected for this simulation-based study.

Table B1. Setup of the FE models for analysis of forming in sparse-point tools of different configurations.

Configuration	Elastomeric sheet	Flexible splines
NN		
NY		●
YY (Generic model)	●	●

To model condition YY, the generic FE model described in Chapter 5 is used and assigned with $h = 8.1$ mm. $R = 1200$ mm is inputted to the pin height generation algorithm and the workheads are positioned accordingly. Residual stresses are not included in the present modelling work and hence the possible effects of residual stresses combined with those being investigated are not considered. Modelling with configurations NY and NN were performed with the elastomeric sheet and both the elastomeric sheet and splines removed respectively. In this appendix, many descriptions of the different tooling elements are made with reference to the spatial

arrangement of the initial model setup. For clarity and completeness, the model definitions of YY are illustrated in Figure B1.

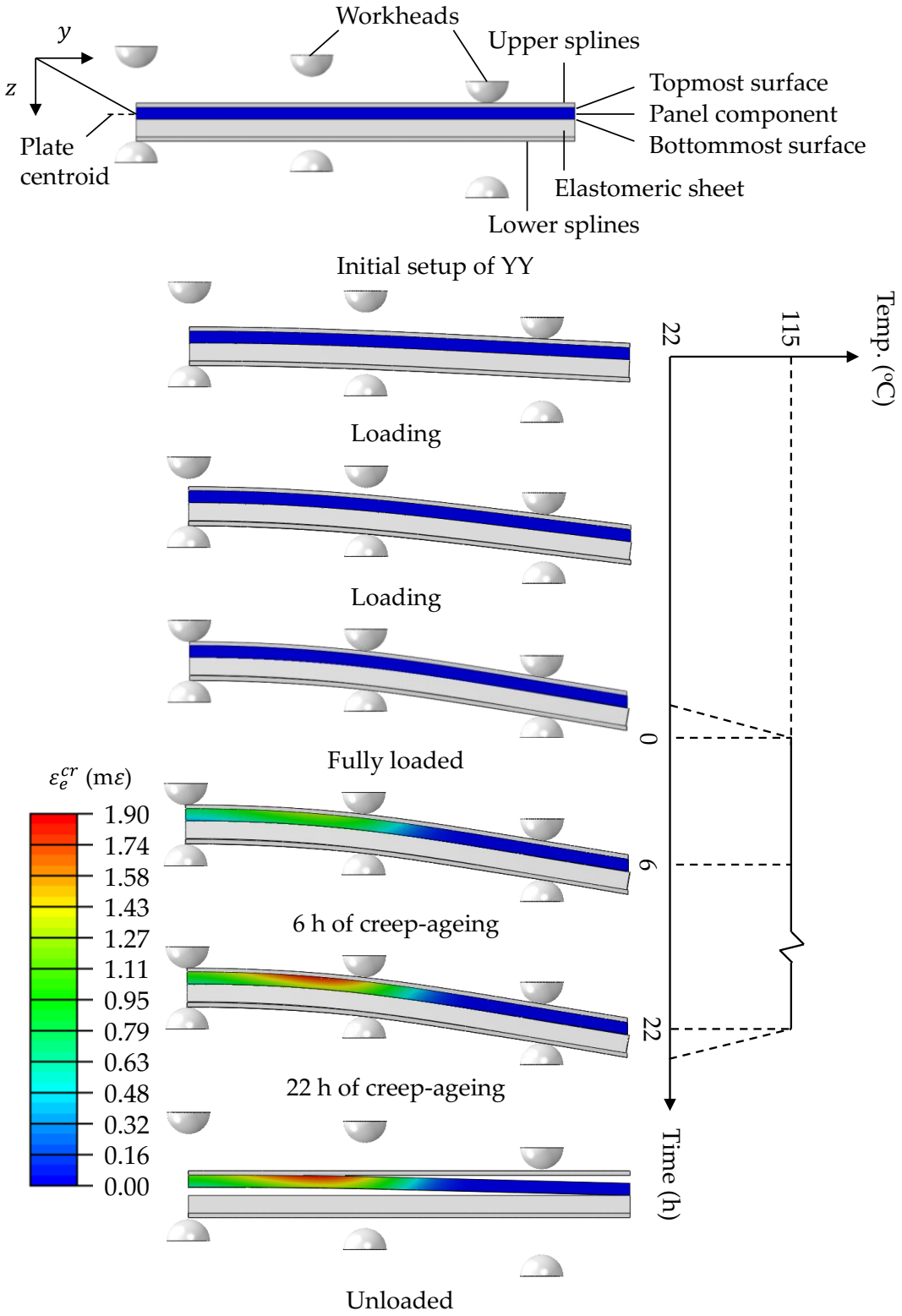

Figure B1. Definitions of the creep-age forming simulations and coordinate system used with to-scale rendering of shell thicknesses. Illustrated below are the six-frame configurations throughout the process of loading, heating, creep-ageing, cooling and unloading.

Deformation in CAF is initiated by stress-induced creep strain, which leads to the occurrence of creep-induced stress relaxation, and eventually introducing permanent deformation to the panel component being formed. The main focus of this study is hence given to the stress analysis of the panel component undergoing viscoplastic deformation during creep-ageing.

B3. Stress analyses

In this section, characteristics of stress relaxation and creep deformation of panel components formed using the generic model (configuration YY) are first presented (B3.1). This is to allow readers to first be familiarised with the typical features of sparse-point CAF. Subsequently, the mechanics of how those features vary with changing individually the tooling configuration (B3.2), friction condition (B3.3), thermal-friction interactions (B3.4) and overloading condition (B3.5) are investigated. At the end, the effects of varying these forming conditions on the formed shape profiles and springback of creep-age formed components are summarised and discussed (B3.6).

B3.1. Stress relaxation and creep deformation in sparse-point tools

B3.1.1. Method

In order to establish the typical stress relaxation and creep deformation characteristics of panel components in sparse-point CAF operations, a simulation was run with the tooling configuration YY. The creep-ageing time evolutions of those characteristics are investigated.

B3.1.2. Results

Results are presented for the creep-ageing time evolutions of von Mises equivalent stress (σ_e) and effective creep strain (ε_e^{cr}) distributions of the plate formed in the tool with both splines and elastomeric sheet (YY). The field plots were generated with the xz- and yz-planes mirrored to illustrate the full model for clarity. The way the

following results are described is with reference to the $x \geq 0$ mm and $y \geq 0$ mm portion of the plate.

Figure B2a shows the σ_e relaxation on the topmost tensile surface of the plate. A higher overall σ_e state is observed in the region between the $y = 0$ and 120 mm workheads. The maximum σ_e (σ_e^{max}) is observed at $x = 175$ mm, where a maximum stress relaxation of 105.2 MPa occurred which reduced σ_e^{max} from 285.1 to 180.0 MPa after 22 h of creep-ageing. 38% of which took place within 1 h, 68% at 6 h, 83% at 12 h and 94% at 18 h of creep-ageing. The overall σ_e state decreases gradually with increasing y and minimum σ_e (σ_e^{min}) is observed outside the forming region. Within the outer y region of between $y = 200$ to 300 mm, local σ_e concentrations increase towards the proximity of where the $y = 240$ mm workheads are located.

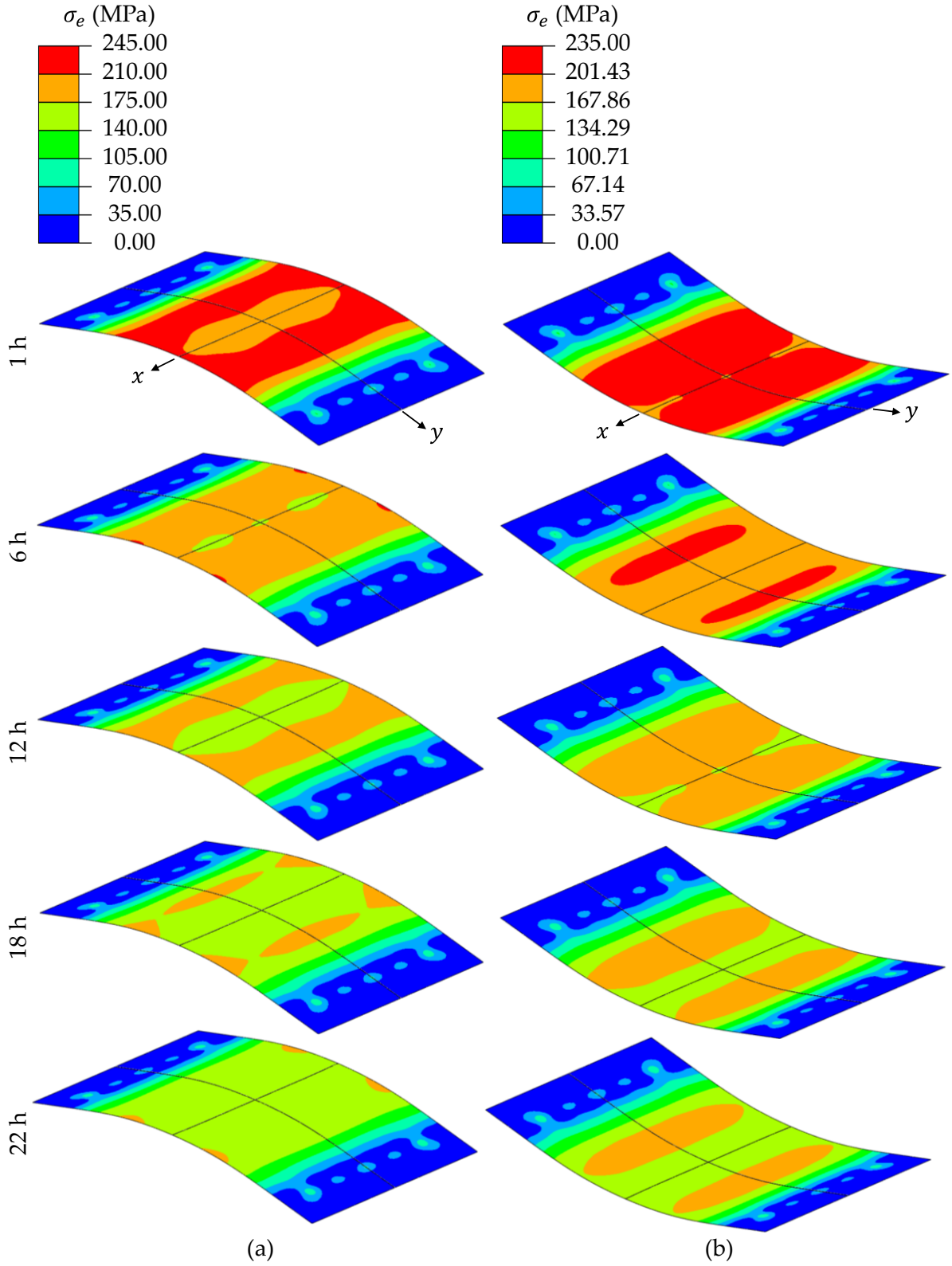

Figure B2. Evolutions of von Mises equivalent stress distributions of the 8.1-mm-thick plate's (a) topmost tensile and (b) bottommost compressive surfaces over the 22 h creep-ageing step.

A similar magnitude and distribution of σ_e is observed on the bottom compressive surface (Figure B2b). At $t = 0$ h, $\sigma_e^{max} = 268.7$ MPa is observed between the $y = 0$ and 120 mm workheads, where the highest elastic deformation is encountered. The σ_e^{max} represents a 6% difference from that of the topmost tensile surface. A total of 90.3 MPa of maximum stress relaxation took place after 22 h of creep-ageing, 15% smaller than that of the tensile surface and reduced the σ_e^{max} to 178.4 MPa. The evolution of maximum stress relaxation is 32%, 65%, 82% and 94% at $t = 1$, 6, 12 and 18 h respectively. As oppose to that observed on the tensile surface, within the $y = 60$ to 120 mm region, a lower σ_e state is observed at $x = 175$ mm than the x-inner region. In general, σ_e decreases gradually in a y-outward manner, with a stress concentration near the proximity of the $y = 240$ mm workheads. The corresponding field plots of effective creep strain distributions are shown for the same plate and arranged in the same format in Figure B3.

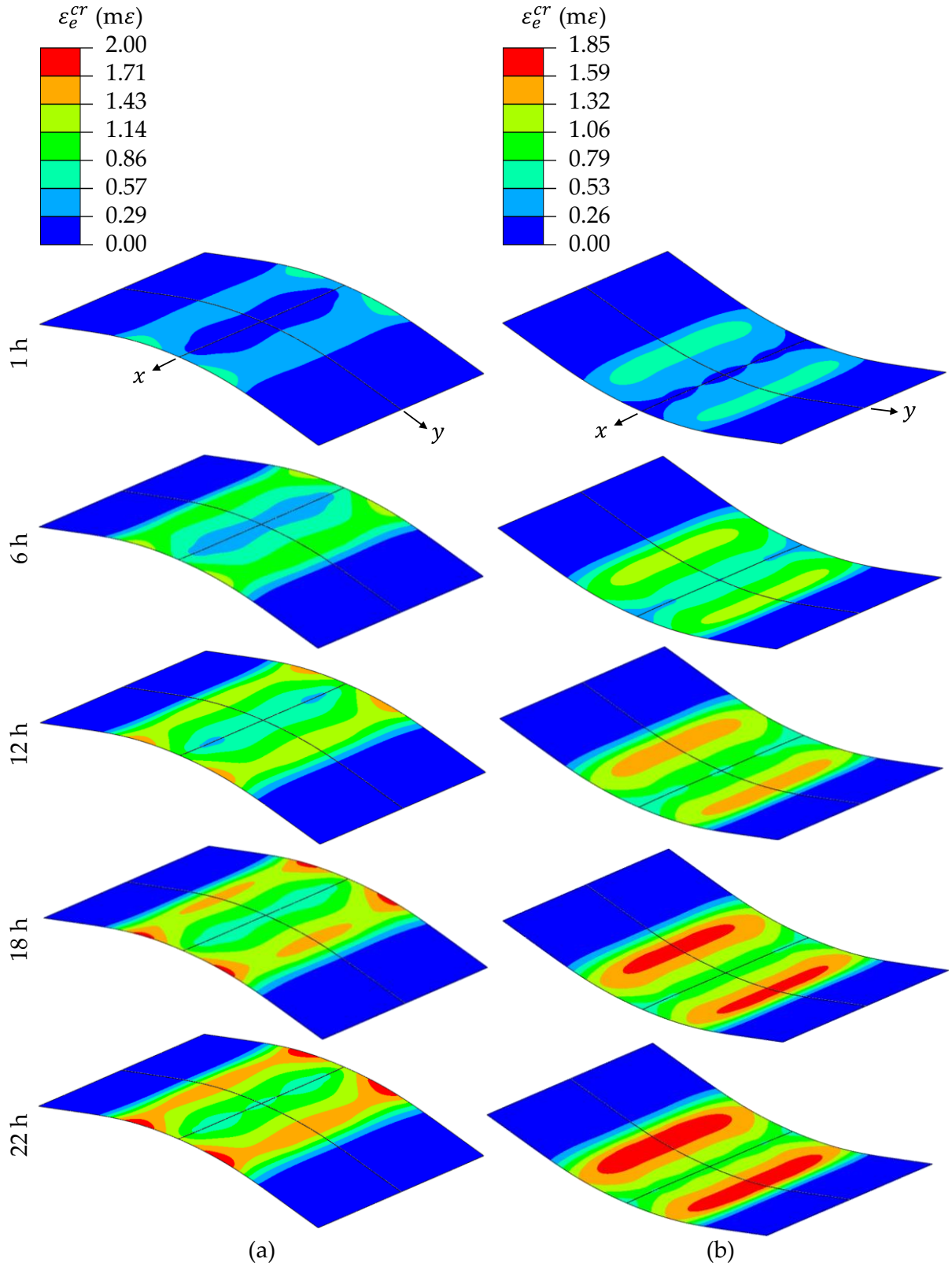

Figure B3. Evolutions of effective creep strain distributions of the 8.1-mm-thick plate's (a) topmost tensile and (b) bottommost compressive surfaces over the 22 h creep-ageing step.

B3.2. Effect of tooling configuration on stress state

B3.2.1. Method

In order to investigate the effect of tooling configuration on stress state of panel components in sparse-point CAF operations, two additional simulations were run with the tooling configurations NN and NY. The topmost surfaces' von Mises equivalent stress distributions at $x = 60$ mm at the fully loaded, heated and creep-aged stages are investigated. The characteristics of stress relaxation and creep deformation in these tooling configurations are compared with the corresponding results obtained from the previous simulation that was run in configuration YY (B3.1).

B3.2.2. Results

Results are presented for the von Mises equivalent stress (σ_e) distributions of the topmost surfaces of plates forming in the three tooling configurations; the tools with direct workhead contact (NN), with splines only (NY) and both splines and elastomeric sheet (YY).

A comparison of the three through-y σ_e distributions at full loading is presented in Figure B4. Within the region of $y = 0$ to 60 mm at full loading, a little difference (< 10 MPa) is observed between the three and they are all close to the theoretical σ_e value of 223.2 MPa. Peaks in σ_e are observed at locations that correlate to those of the workheads' positions. In all three cases, the highest peaks of the distributions are observed near 120 mm with a second peak observed near 240 mm. The σ_e levels recorded at these peaks are summarised in Table B2.

Table B2. Values of peak von Mises equivalent stresses recorded from the through-y distributions.

Configuration	First peak σ_e (MPa)	Second peak σ_e (MPa)
NN	323.1	138.7
NY	356.7	268.6
YY	259.1	81.8

The highest overall stress response is seen in NY, which has a through-y average σ_e of 169 MPa. It is followed by the 157 MPa of NN and the 147 MPa of YY.

These averages are all lower than the theoretical pure bending σ_e value, representing 66% to 76% of the latter. The magnitudes of the peak σ_e follow the same order of sequence as that of the average values, with NY the highest, NN the middle and YY the lowest (Table B2).

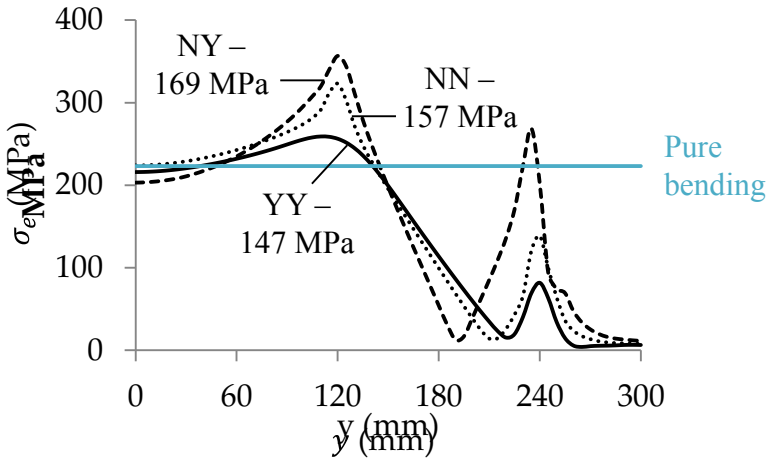

Figure B4. A comparison of the theoretical von Mises equivalent stress value (pure bending) with distributions of that on the topmost surfaces of plates formed in different tooling configurations. The values indicate the through-y average von Mises equivalent stress.

Unlike the positions of peak σ_e, the minimum σ_e value between the two peaks varies largely in y-positions for the three cases. It is observed that the minimum value is furthest away from the second peak position when the latter takes the highest value of all the three cases (for NY) whilst the opposite is also true (for YY).

Further comparisons illustrating the through-y σ_e distributions of the plates at 0 and 22 h of creep-ageing time are presented in Figure B5. The total amount of σ_e relaxed and creep strain accumulated are plotted on the same graphs for each tool.

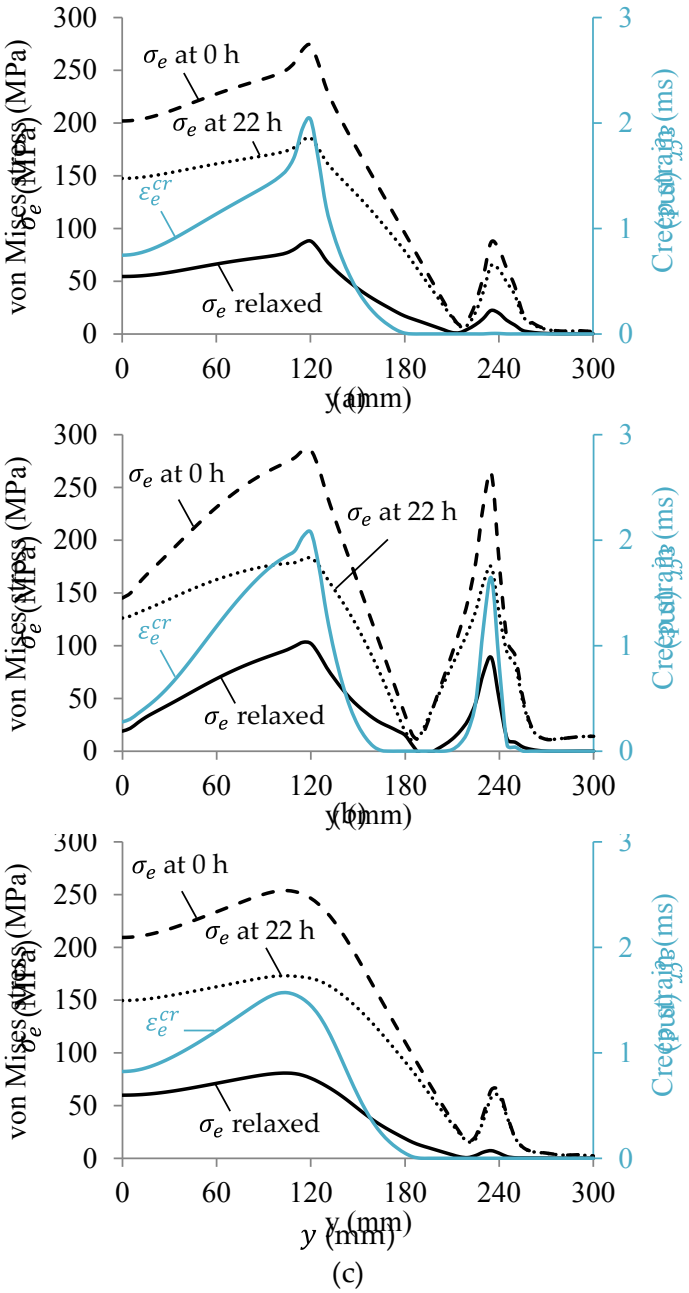

Figure B5. Comparisons of the through-*y* von Mises equivalent stress distributions in tooling configurations (a) NN, (b) NY, and (c) YY at 0 and 22 h of creep-ageing. Also plotted are the total amount of stress relaxed and effective creep strain accumulated. Results are for the topmost surfaces of plates.

B3.3. Effect of friction condition on stress state

B3.3.1. Method

In order to investigate the effect of friction condition on stress state of panel components in sparse-point CAF operations, three additional simulations were run with frictionless contacts assigned between all parts of the models NN, NY and YY. Both the topmost and bottommost surfaces' longitudinal stress distributions at $x =$ 60 mm at full loading are investigated. These results are compared with the corresponding results obtained from the three simulations that were run (B3.1 – B3.2) with the normal friction conditions assigned.

B3.3.2. Results

Figure B6 shows the through-y longitudinal stress distributions of the plates in the three tooling configurations simulated with and without friction. The topmost and bottommost surfaces of all the plates are in general in a tensile and compressive stress state respectively. Figure B7 further quantifies the results by plotting for the topmost plate surfaces, the absolute through-y-average values of those curves. Of the three configurations, the plate formed in NY has the highest overall stress state followed by NN, and with YY the smallest. In terms of stress state sensitivity to friction, model NN has a higher sensitivity to friction than model NY. The stress sensitivity to friction of model YY is the smallest and is also close to negligible.

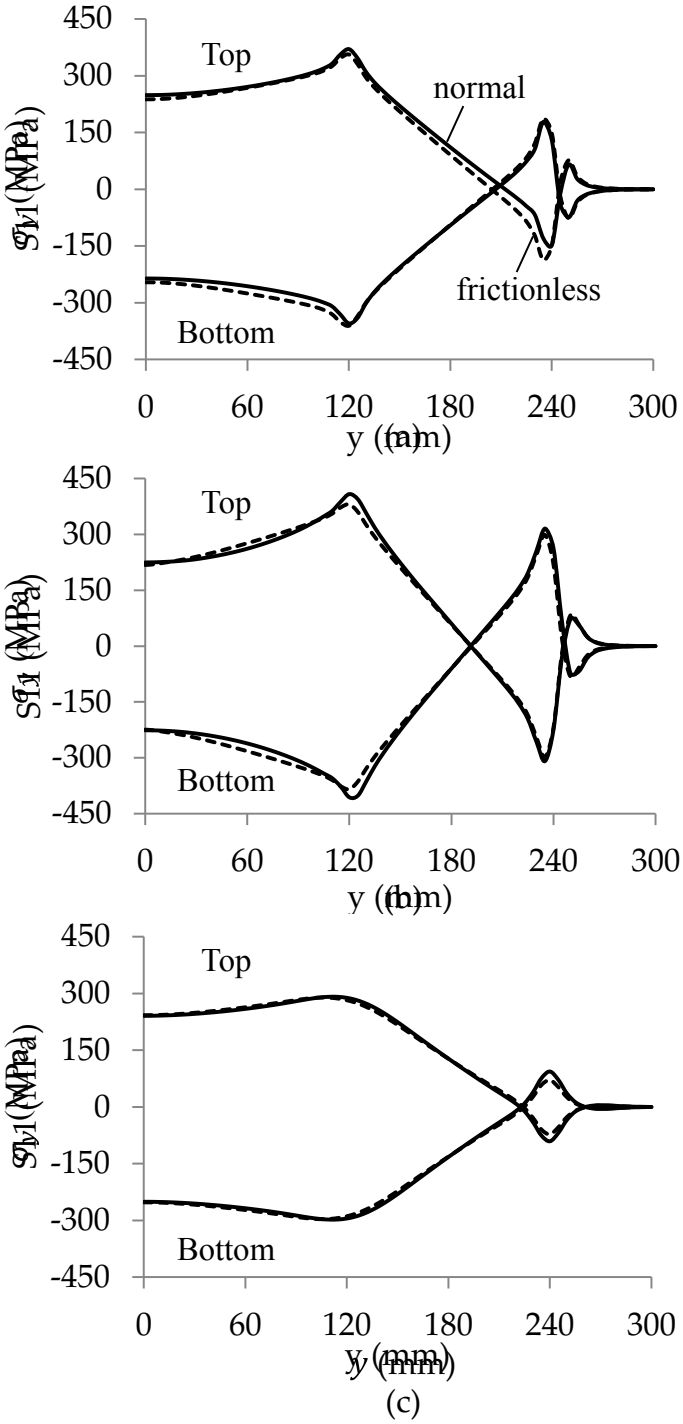

Figure B6. Comparisons of the through-*y* longitudinal stress distributions due to modelling with and without friction in tooling configurations (a) NN, (b) NY and (c) YY. Results are for the topmost and bottommost surfaces of plates at full loading.

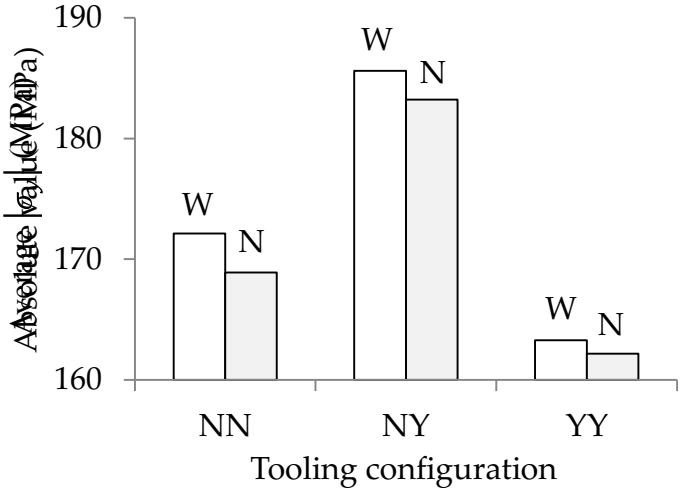

Figure B7. A comparison of the through-*y* averages of absolute longitudinal stresses due to modelling with (W) and without (N) friction in tooling configurations NN, NY and YY. Results are for the topmost surfaces of plates at full loading.

B3.4. Effect of thermal-friction interactions on stress state

B3.4.1. Method

In order to investigate the effect of thermal-friction interactions on stress state of panel components in sparse-point CAF operations, the change in longitudinal stress at $x = 60$ mm from before to after heating is compared with the results obtained from the six simulations that were run (B3.1 – B3.3) with and without friction with the three tooling configurations NN, NY and YY.

B3.4.2. Results

Figure B8 shows the change in the through-y average values of absolute longitudinal stresses due to heating the plates in the three tooling configurations. For the topmost surface of the plates (Figure B8a), heating generally caused a negative change in value. This is due to the counteracting stress between the tensile bending stress on the topmost plate surface and the introduction of compressive stress due to constrained heating. In all cases, modelling thermal effects with friction caused a greater change in stress level than without friction. Of the three configurations, YY exhibits the least stress sensitivity to thermal-friction interactions than the other two models. An opposite change in stress level is observed for the bottommost surface of the plates (Figure B8b). The trend of stress sensitivity to thermal-friction interactions remains the same for the bottommost surface.

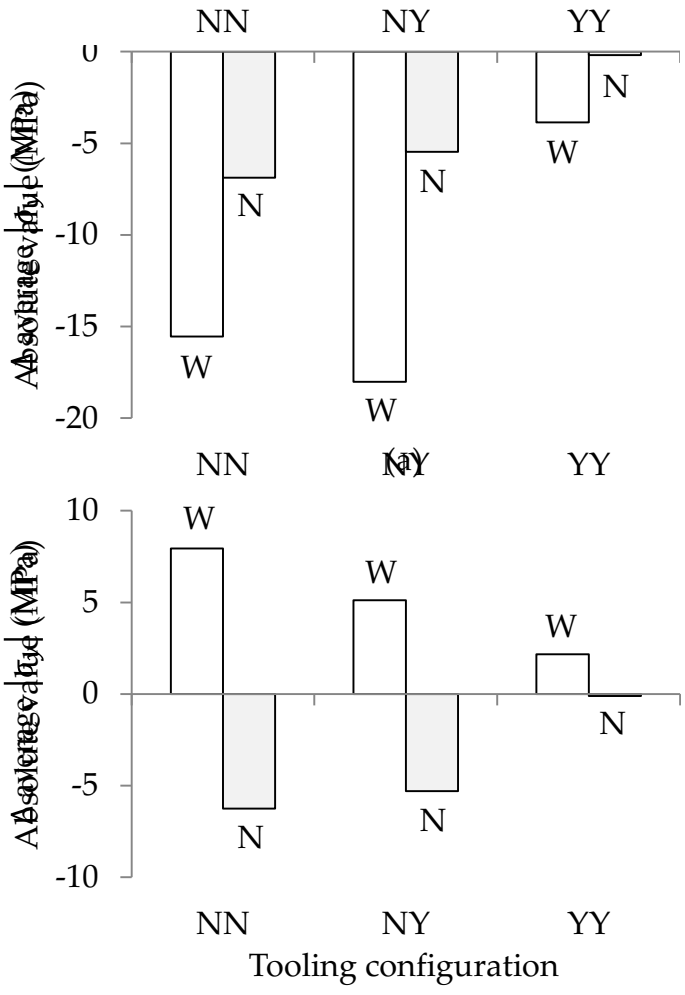

Figure B8. Comparisons of the change in through-*y* average values of absolute longitudinal stresses due to heating in tooling configurations NN, NY and YY. Results are for (a) the topmost and (b) bottommost surfaces of plates forming with (W) and without (N) friction modelled.

B3.5. Effect of overloading on stress state

B3.5.1. Method

In order to investigate the effect of over punch travel on stress state of panel components in sparse-point CAF operations, three additional simulations were run with an additional 0.25 mm (+1% of original punch travel) assigned to the top workheads of the three models (NN, NY and YY). The resulting topmost surfaces' von Mises equivalent stress distributions at $x = 60$ mm are compared with the corresponding results obtained from the previous simulations that were run (B3.1 – B3.2) with normal punch travel and friction conditions.

B3.5.2. Results

Figure B9 compares the through-y equivalent stress distributions for the topmost surfaces of the plates when formed with a normal and +1% overloading punch travels in the three tooling configurations. High local stress concentrations are observed near the workheads' positions in models NN and NY due to the introduction of 1% overloading punch travel. The function of the elastomeric sheet is significant in reducing stress concentrations due to overloading, leading to the significantly less stress state sensitivity to overloading for model YY.

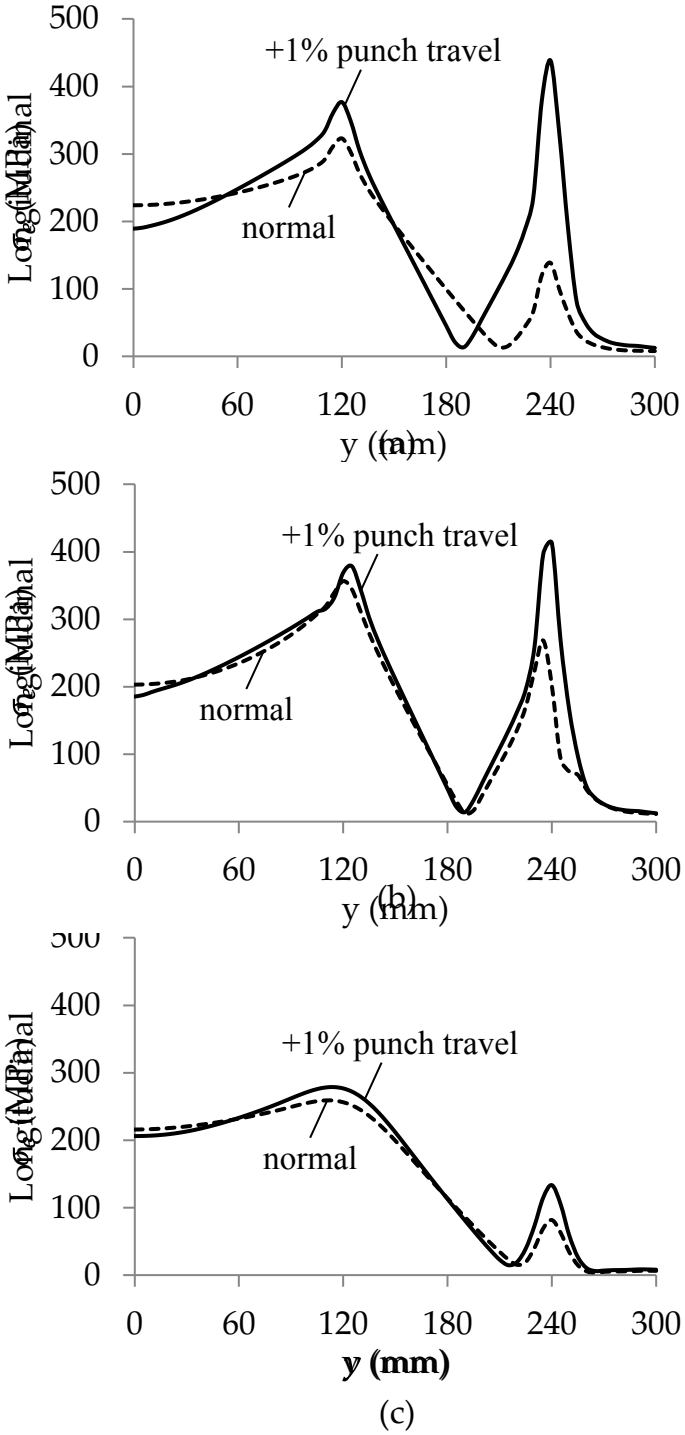

Figure B9. Comparisons of through-*y* von Mises equivalent stress distributions due to normal and overloaded (+1%) punch travel in tooling configurations (a) NN, (b) NY, and (c) YY. Results are plotted for the topmost surfaces of plates at full loading.

B3.6. Springback sensitivity to stress disturbances in different tooling configurations

B3.6.1. Method

In order to investigate the springback sensitivity of panel components to stress disturbances due to all the above-investigated forming conditions in sparse-point CAF operations, the final formed shape profiles and springback of plates from all the nine simulations (B3.1 – B3.3 and B3.5) are outputted, analysed and summarised under this section.

B3.6.2. Results

Figure B10 compares the formed shape profiles of all the plates simulated for the above investigations, with and without the effects of friction and overloading considered in the three tooling configurations. This comparison illustrates directly how the formed shape profiles are affected by the above-investigated stress disturbances in the three tooling configurations.

Figure B10a shows the influence of modelling with and without friction on formed shape profiles. Plates formed in configuration NY have a relatively larger difference in shapes than those formed in NN and YY. Whilst the plates formed in configurations NN and YY have similar formed shape profiles. The effect of friction on formed shape is also apparent with configuration NY, with NN and YY again showing less formed-shape-sensitivity to friction.

Figure B10b shows the influence of overloading on formed shape profiles. All the three models show an observable formed-shape-sensitivity to the 1% overloading punch travel. Overloading the plates in configurations NN and NY have introduced an additional 2 mm deflection to the formed plates. Significant local distortions to the formed shape profiles are also observed near the workheads' positions. The role of an elastomeric sheet in reducing local shape distortion and overall formed shape deviation due to punch overloading is significant. For the same

amount of overloading, the formed shape profile of the plate formed in model YY only saw a maximum of 0.2 mm change in the shape profile of the formed plate.

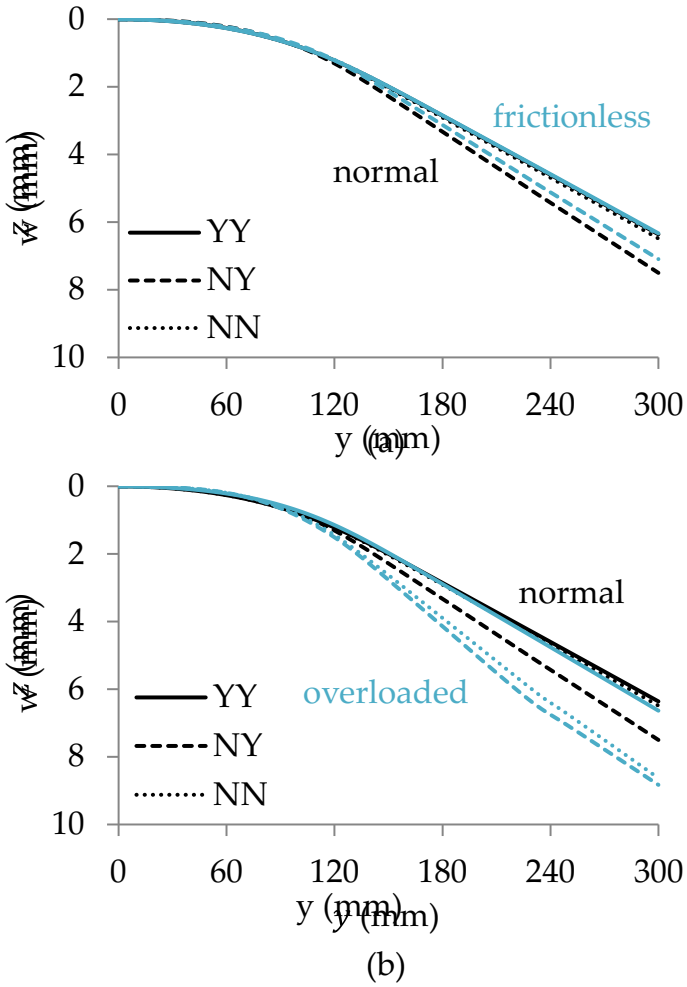

Figure B10. Comparisons of the formed shape profiles of plates simulated under (a) normal *vs.* frictionless and (b) normal *vs.* overloaded conditions in different tooling configurations.

The springback sensitivity to the different forming conditions and in different tooling configurations is summarised in Figure B11. Configuration NY exhibits the greatest springback sensitivity to friction, followed by configuration NN. Both of these configurations have similar springback sensitivity to overloading. Of the three configurations, plates formed in YY have the most stable springback value across all forming conditions, showing the least springback sensitivity to all the effects of friction and overloading.

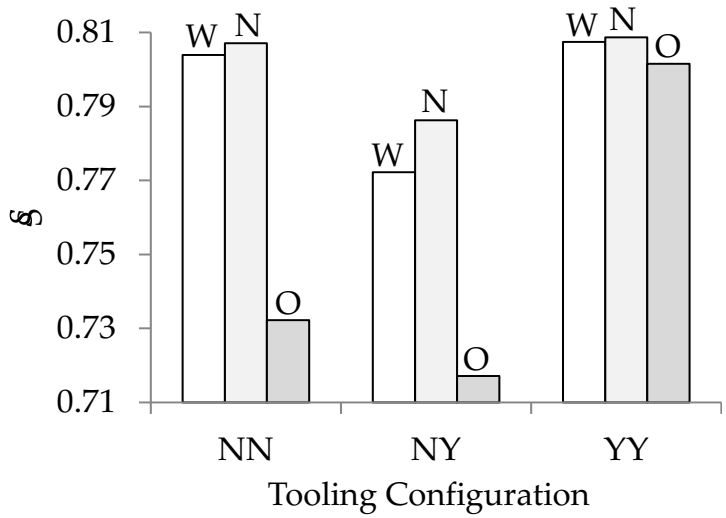

Figure B11. A comparison of springback sensitivity to different forming conditions (W – with friction, N – no friction and O - overloaded) and tooling configurations (NN, NY and YY).

B4. Implications for optimal tooling configurations

Stress analyses of sparse-point CAF of panel components were performed using finite element method. Springback sensitivity of the panel component to different tooling configurations, friction conditions, thermal-friction interactions and overloading were investigated. Based on the simulation results, the following conclusions can be drawn to provide suggestions for the optimal tooling configuration for use in this research:

- Sparse-point tools can be used to accurately load panel components to a given target shape, replacing the need for conventional multipoint tools for flexible forming.
- The tooling configuration with the presence of both splines and elastomeric sheet has the least springback sensitivity to friction conditions, thermal friction interactions and overloading, which can vary in a laboratory-scale CAF environment due to the lack in friction data available, control precisions of loading and heating machines and possible human errors. This configuration is therefore the optimal tooling configuration for this research.

APPENDIX C.

FORM TOOL DESIGN OUTPUT

C1. Part drawings and dimensions

C1.1. Top die holder

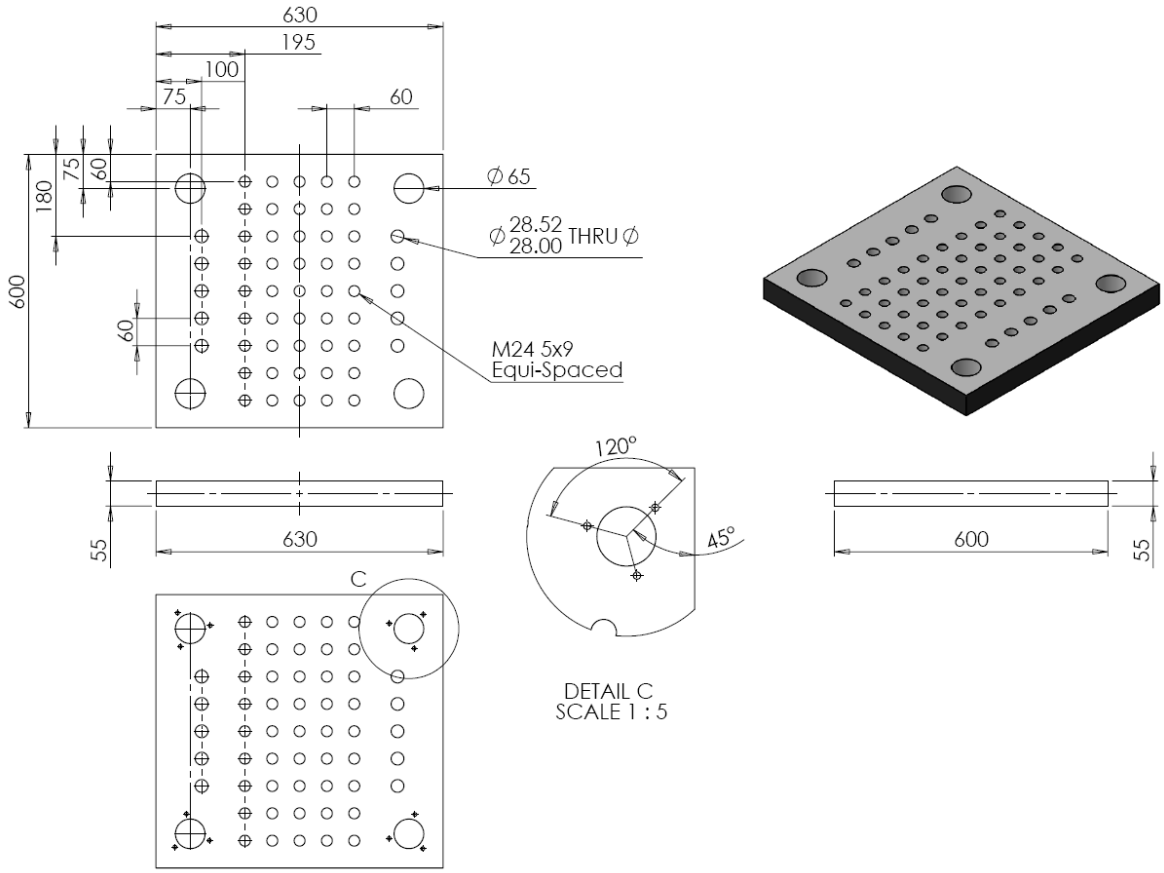

Figure C1. Engineering drawing of the top die holder.

C1.2. Bottom plate

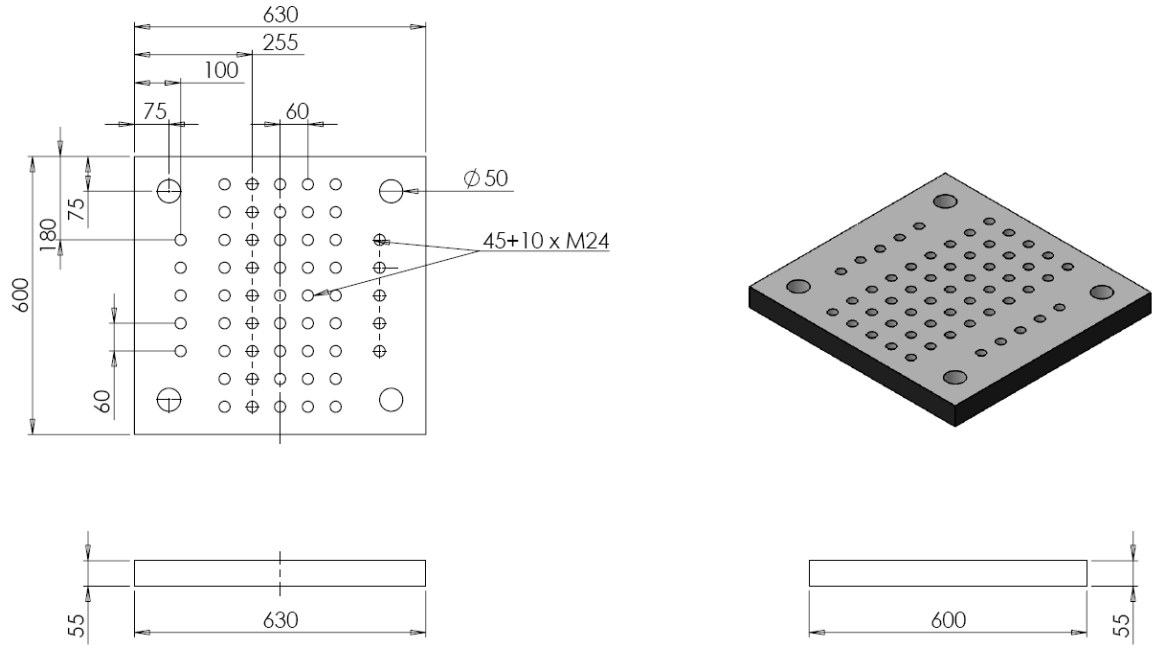

Figure C2. Engineering drawing of the bottom die holder.

C1.3. Precision guide pillars

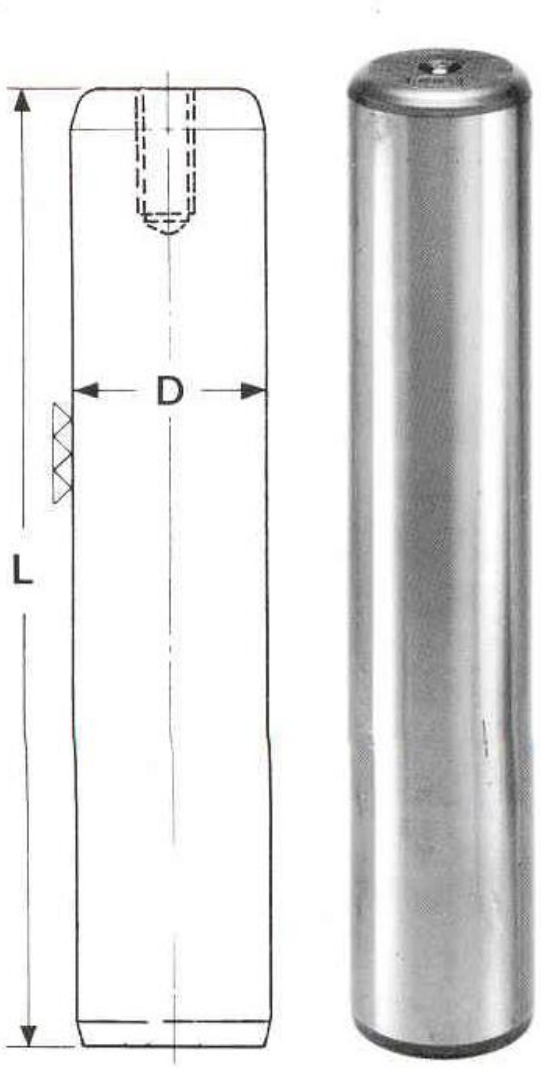

Figure C3. Image and engineering drawing of the precision guide pillars. Image adapted from page 6 of the PDF file at http://www.danlyuk.com/Solid%20Guiding.pdf.

Table C1. Catalogue number and dimensions of the precision guide pillars.

Catalogue Number	5-5045-82
D (mm)	50
L (mm)	450
Pillar Thread Size	M10

C1.4. Demountable steel bushes

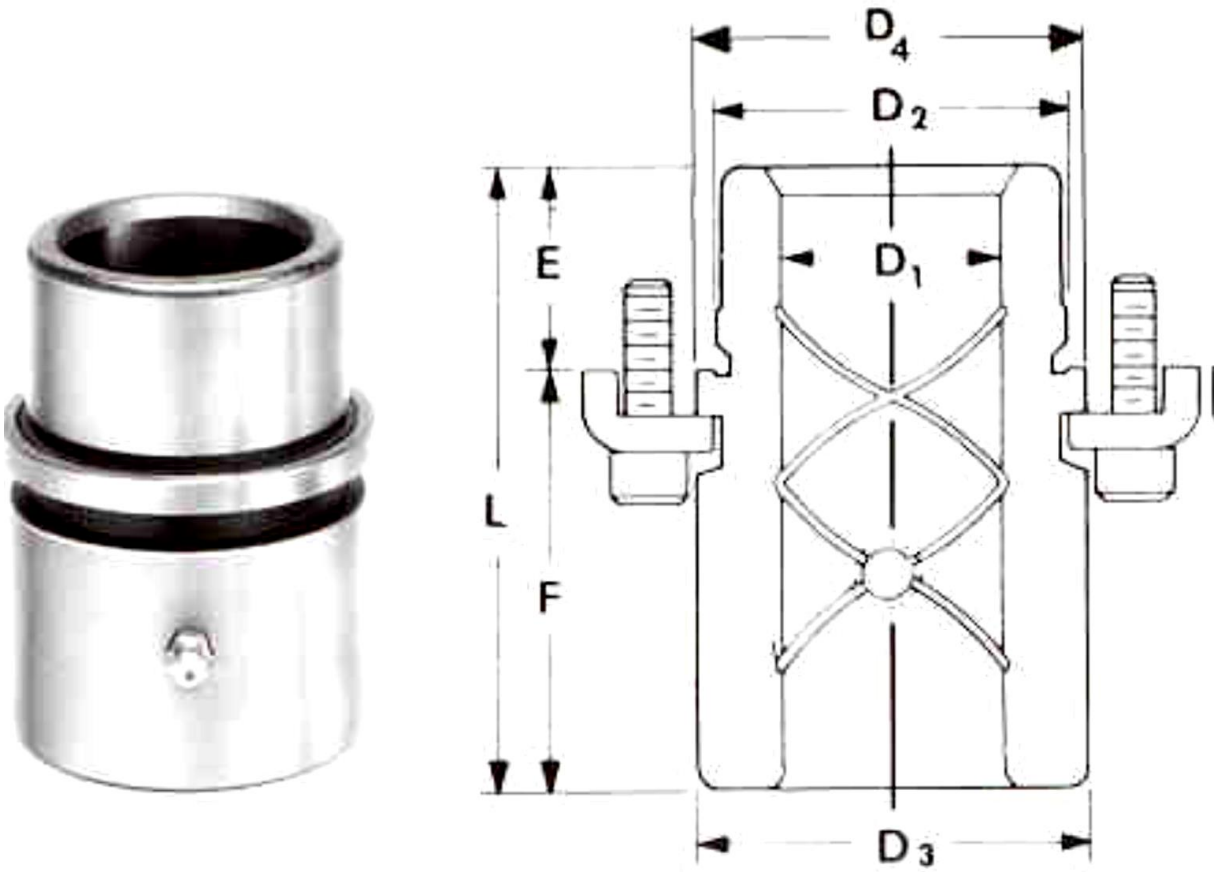

Figure C4. Image and engineering drawing of the demountable steel bushes. Image adapted from page 7 of the PDF file at http://www.danlyuk.com/Solid%20Guiding.pdf.

Table C2. Catalogue number and dimensions of the demountable steel bushes.

Catalogue Number		6-5065-64
D1	(mm)	50
D2	(mm)	65
D3	(mm)	73
D4	(mm)	75
E	(mm)	35
F	(mm)	50
L	(mm)	85
Screw Size		M8

C1.5. M24 studding and nuts

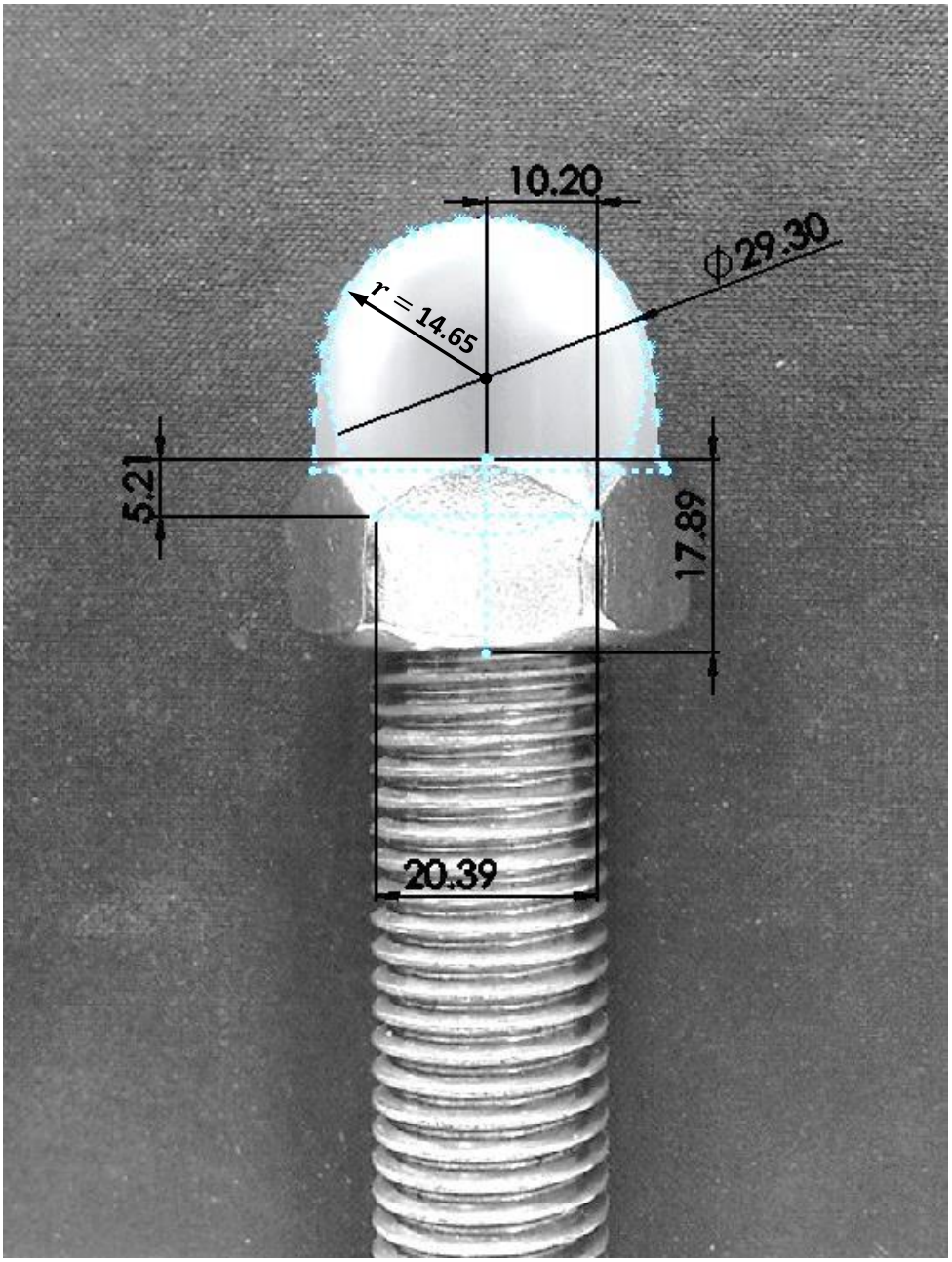

Figure C5. Image-converted SolidWorks model for estimation of forming pin dimensions. Dimensions are in millimetres.

Table C2. A summary of the size and material information of the studding and nuts.

Part	Size/Standard	Material
Studding	M24	A2 stainless steel
Dome Nut	M24	A2 stainless steel
Full Nut	M24	A2 stainless steel

C1.6. Die springs

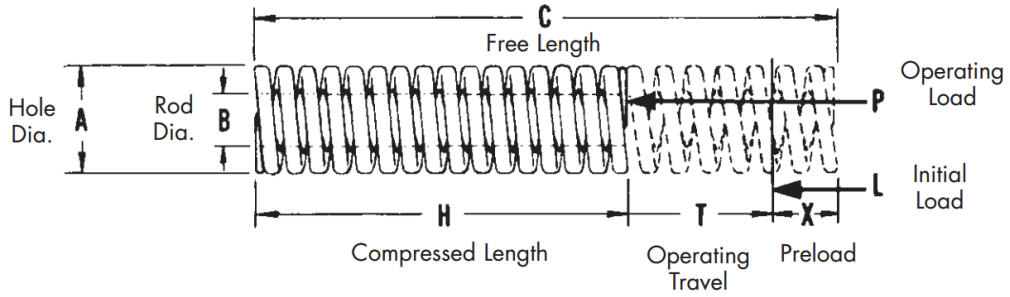

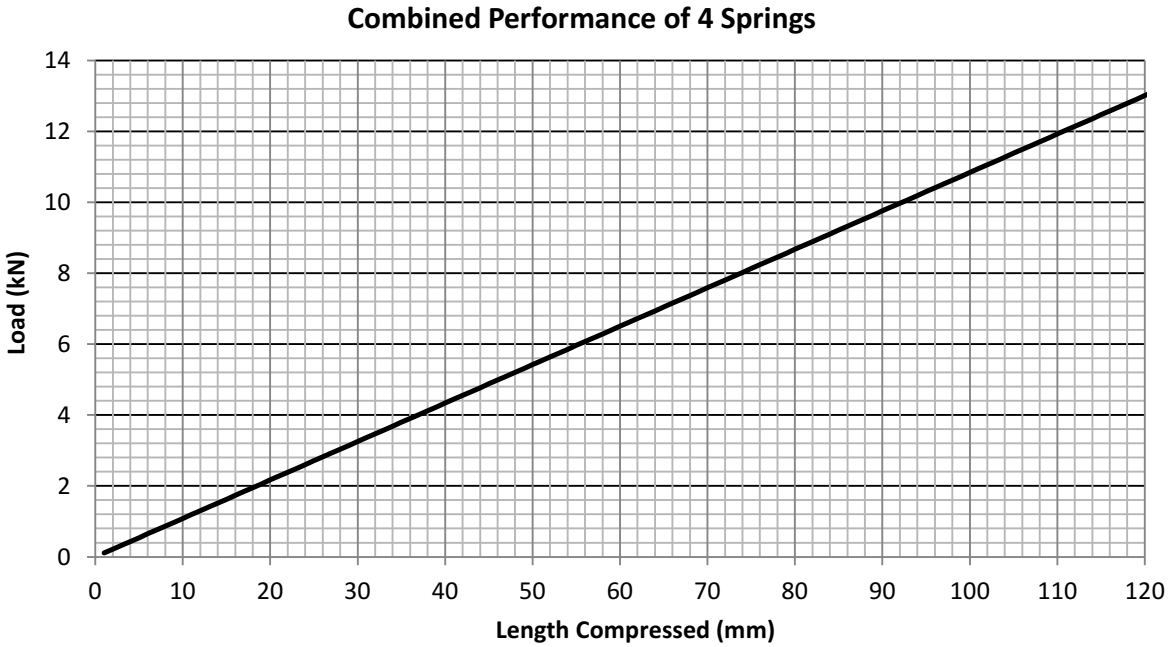

Figure C6. Top: Engineering drawing of a single die spring. Image adapted from page 3 of http://www.danlyuk.com/Danly%20Super%20Springs%20Cat.pdf. Bottom: Estimated combined performance of four die springs.

Table C3. Catalogue number and technical specifications of the die springs.

Catalogue Number	9-3248-110	
Hole Dia. (mm)	50	
Rod Dia. (mm)	25	
Free Length (mm)	305	
Spring Stiffness	2.71 daN to deflect 1 mm	
Long Life	Load (daN)	207
	Deflection (mm)	76
Avg. Life	Load (daN)	248
	Deflection (mm)	92
Max. Deflection	Load (daN)	331
	Deflection (mm)	112
Total to Solid	Load (daN)	423
	Deflection (mm)	156

C2. Current limit to pin heights

Current pin height limitations exist in both the chord and span direction of the tool. Figure C7 shows a view of the forming tool model from the chord direction. The maximum pin height difference in the chord direction is mainly limited by the length of the studding. The adjustable length of the studding is approximately 120 mm. The workhead component of each forming pin is approximately 50 mm in height. This gives a 70 mm maximum height difference between forming pins in the chord direction.

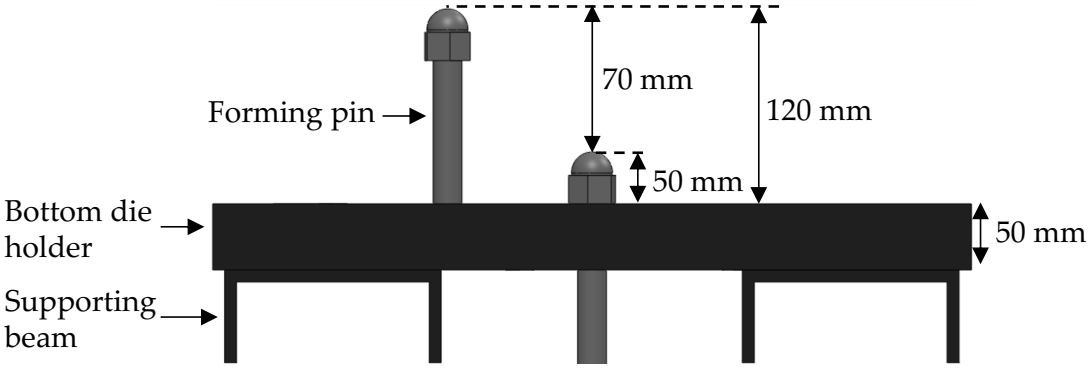

Figure C7. View from the chord direction of the forming tool.

Figure C8 shows the cross-sectional view of the forming tool model at the span direction. The current tool limit is mainly due to the U-channel obstruction. This limit can be expanded by drilling holes into the supporting U-channels to allow forming pins to pass through. This was not done because the shape requirement in this research did not reach this limit.

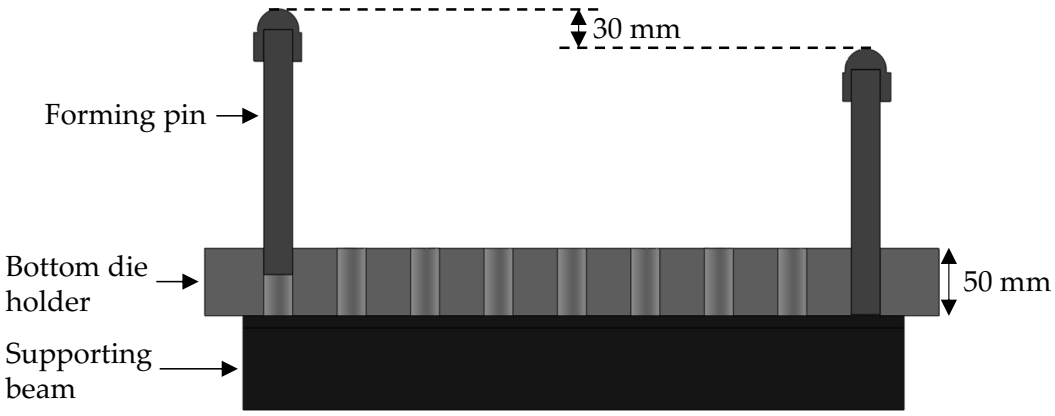

Figure C8. Cross-sectional view at the span direction of the forming tool.

C3. Part count and weight estimation

Table C4. Summary of part-count and weight estimation.

	Unit weight (kg)	Quantity	Total weight (kg)
Top plate/die holder	146.86	1	147
Bottom plate/die holder	150.02	1	150
Precision guide pillar	6.97	4	28
Demountable steel bush	2.09	4	8.5
Die spring	1.41	4	5.7
Locking pin (400 mm stud)	2.06	4	8.3
Forming pin (stud + dome nut + full nut)	0.98	50	49
		Total	396.5

C4. Purchase part details

Table C5. Summary of purchase part details including description, name of supplier and cost.

Description	Supplier	Quantity	Unit cost (£)	Tot. ex. VAT (£)
Die set made to request + die springs 9-3248-110	Danly UK Ltd	1	2143.32	2143.32
M24 1 m stud	Cromwell Tools	8	19.96	159.68
M24 dome nut	Cromwell Tools	45	3.68	165.60
M24 full nut	Cromwell Tools	55	0.93	51.40
M24 3 m stud	Cromwell Tools	2	69.29	138.58
M24 dome nut	Cromwell Tools	19	4.78	90.82
Silicone rubber 264 x 350 x 12 mm^3	Silex Ltd	7	15.58	109.06
Silicone rubber 300 x 600 x 5 mm^3	Silex Ltd	2	14.5.0	29.00
Silicone rubber 45 x 350 x 10 mm^3	Silex Ltd	1	13.00	13.00
Silicone rubber 45 x 350 x 12 mm^3	Silex Ltd	1	14.00	14.00
Silicone rubber 600 x 350 x 12 mm^3	Silex Ltd	2	31.00	62.00
			ex. VAT (£)	2976.46
			inc. VAT (£)	3571.75

APPENDIX D.

COORDINATE-MEASURING MACHINE OPERATION

D1. Software program template

Template.dmi

```
SNSET/SEARCH,20
DMISMN/'Start Template',05.2
FILNAM/'Start Template',05.2
DV(0)=DMESWV/'63,1,2,599'
UNITS/MM,ANGDEC
DECPL/ALL,DEFALT
V(0)=VFORM/ALL,PLOT
DISPLY/TERM,V(0),STOR,DMIS,V(0)
SNSET/APPRCH,15
SNSET/CLRSRF,15
SNSET/DEPTH,0
SNSET/RETRCT,20
SNSET/SEARCH,5
D(0)=DATSET/MCS
MODE/MAN

T(CORTOL_X1)=TOL/CORTOL,XAXIS,-0.1,0.1
T(CORTOL_Y1)=TOL/CORTOL,YAXIS,-0.1,0.1
T(CORTOL_Z1)=TOL/CORTOL,ZAXIS,-0.1,0.1
T(DIAM_1)=TOL/DIAM,-0.1,0.1

RECALL/SA(132_4X20_A0B0)
RECALL/SA(132_4X20_A105B0)
RECALL/SA(132_4X20_A105B180)
RECALL/SA(132_4X20_A105B90)
RECALL/SA(132_4X20_A105B-90)
```

```
RECALL/SA(132_4X20_A45B0)
RECALL/SA(132_4X20_A45B180)
RECALL/SA(132_4X20_A45B90)
RECALL/SA(132_4X20_A45B-90)
RECALL/SA(132_4X20_A90B0)
RECALL/SA(132_4X20_A90B180)
RECALL/SA(132_4X20_A90B90)
RECALL/SA(132_4X20_A90B-90)

TEXT/OPER,'FIT THE 4X20 PROBE THAT HAS BEEN CALIBRATED'
TEXT/OPER,'ADD SENSOR RECALLS FOR ANY OTHER CALIBRATED PROBES THAT
ARE REQUIRED'

TEXT/OPER,'Line 1'

PAUSE
ENDFIL
```

D2. Procedure for machine operation

The CMM operation procedure is summarised as follows:

1. Save the above software program template as “Template”. This is the master copy.
2. Turn on gas pipe and power supply.
3. Start the software Camio 6.3.
4. Select "Open program".
5. Create a copy of the “Template” and rename the new file specifying particular test information.
6. Open the renamed file.
7. Run the program from first line and bring the arrow to below "TEXT/OPER,'Line 1'".
8. Manually operate the CMM and move the probe to the point of origin.
9. Select "Model" and then "Add plane".
10. Enter "XYZ" and size information of the component.
11. Double click the plane and delete a line.

12. Select “Manual operation” mode, select “4 touches”, select “Apply modules” and register points by manually operating the CMM probe.
13. Setup datum: go to “One axis” and tick all of “xyz” under the origin, check “+z axis” and select “OK”.
14. Create slices on the plane using the “Slice” function.
15. Select “Multi Point”, click “Auto”.
16. On the icon bar select “Curve”.
17. The interface on the left changes to program the points on the curve.
18. Go over to the model and click on the curve that you have added (usually blue lines).
19. Notice the white circle (handles) at each end.
20. Click on “Spacing” and enter the distance you want between each point.
21. Now click and frag the white handles along the curve/slice to cover the length of the curve. Each marker will be a point, the red one is point one (can be changed using “Reverse”).
22. Once satisfy with the arrangement, click “Build” and point markers will be generated at each position.
23. Click “Apply” to finish, then click “Apply” to run or “Curve” to do the next slice.
24. Output the points as “Profile of a point”.

APPENDIX E.

TRANSMISSION ELECTRON MICROSCOPY ANALYSIS RESULTS

E1. Overview

This appendix presents the TEM analysis results of the as-received and 22-h-stress-free-aged samples. A list of concluding remarks from these results is then presented at the end of this appendix. Figure E1 shows the thermal cycle of the two samples.

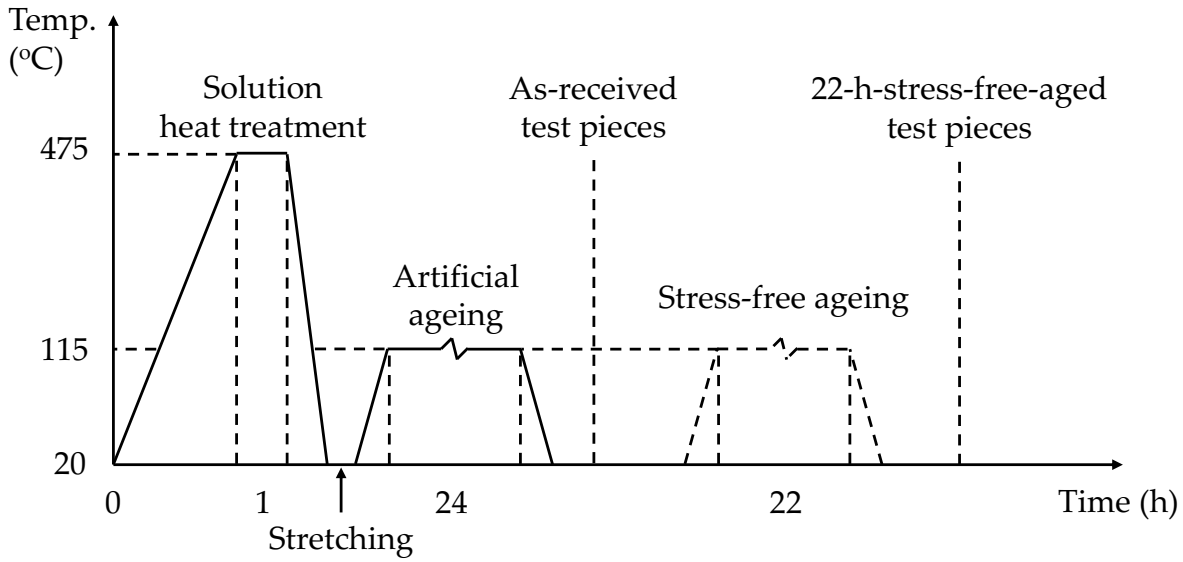

Figure E1. Thermal cycle of the as-received and 22-h-stress-free-aged samples submitted for TEM analysis.

E2. Analysis results of the as-received sample

The TEM analysis results of the as-received sample are presented in this section. Figure E2 and Figure E3 present the TEM micrograph of the distribution of FCC grains. The morphology of fibrous precipitates and the corresponding EDX spectrums are presented in Figure E4. Figure E5 shows the distribution of its GP zone and η′ precipitate. Figure E6 presents a high resolution micrograph of its GP zone. Figure E7 presents a high resolution micrograph of the metastable η′ precipitate, the corresponding FFT image, diffraction pattern and EDX spectrum.

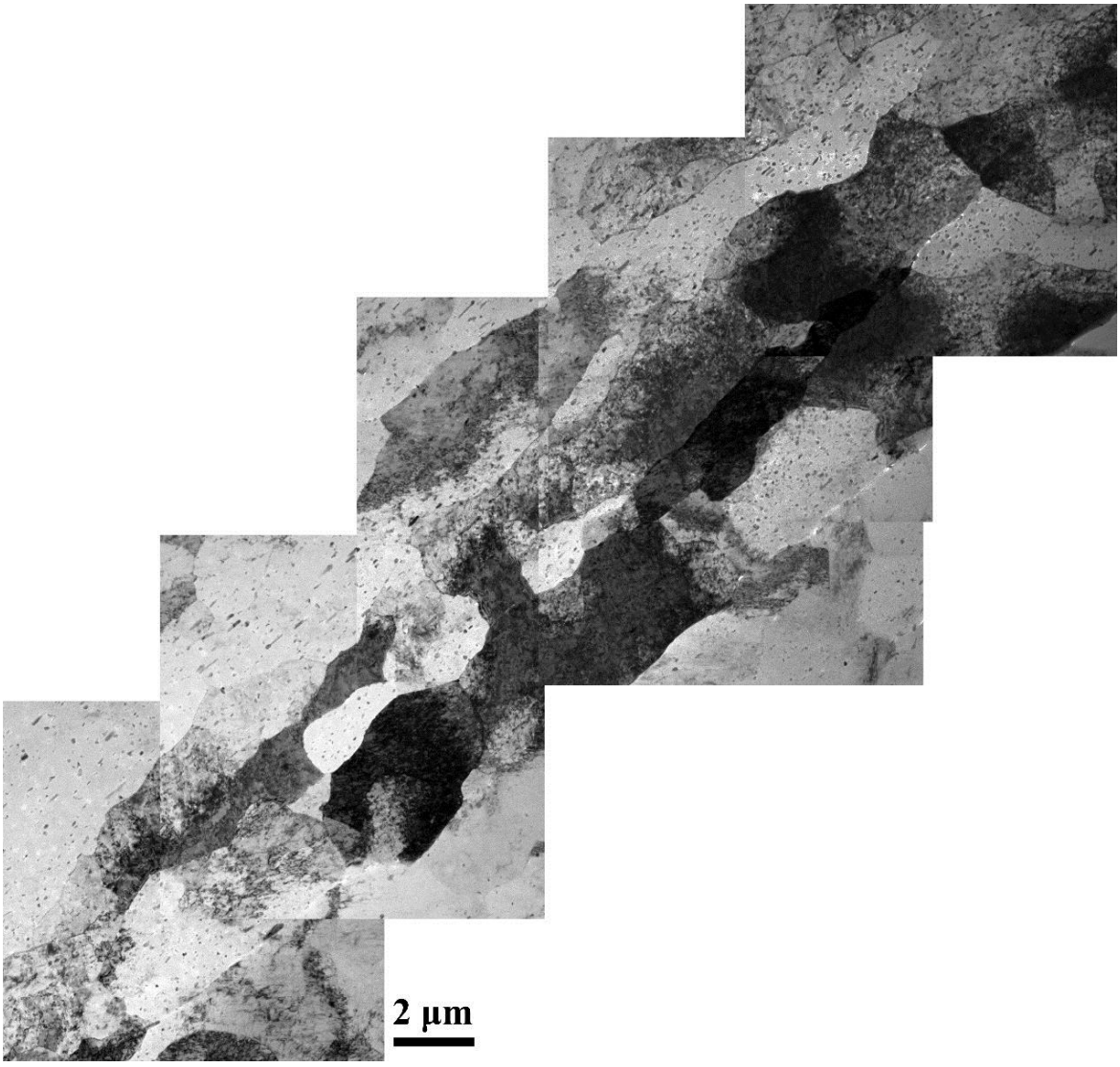

Figure E2. TEM micrograph showing the distribution of FCC grains of the as-received sample.

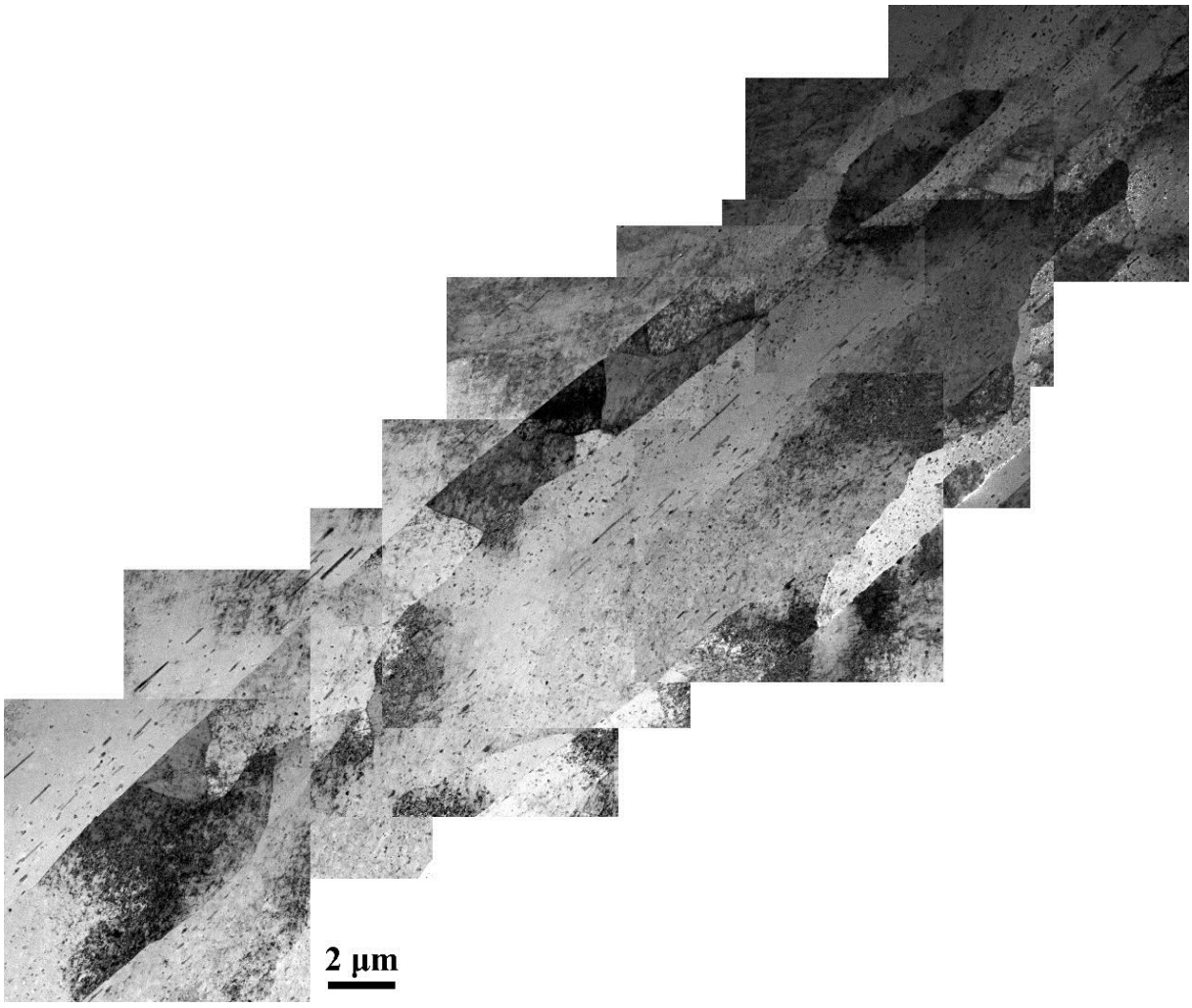

Figure E3. TEM micrograph showing the distribution of FCC grains of the as-received sample.

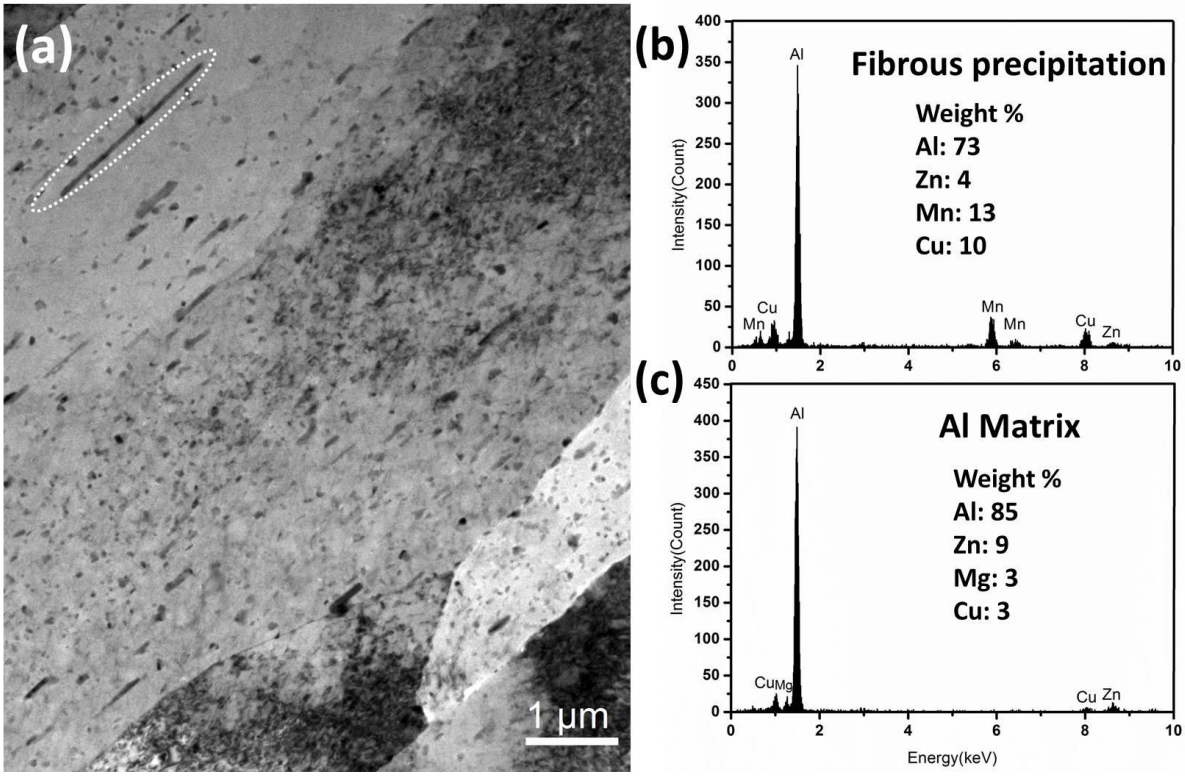

Figure E4. (a) TEM micrograph showing the morphology of fibrous precipitation of the as-received sample in Figure E3. (b) The corresponding EDX spectrum for fibrous precipitation. (c) The EDX spectrum of the aluminium matrix.

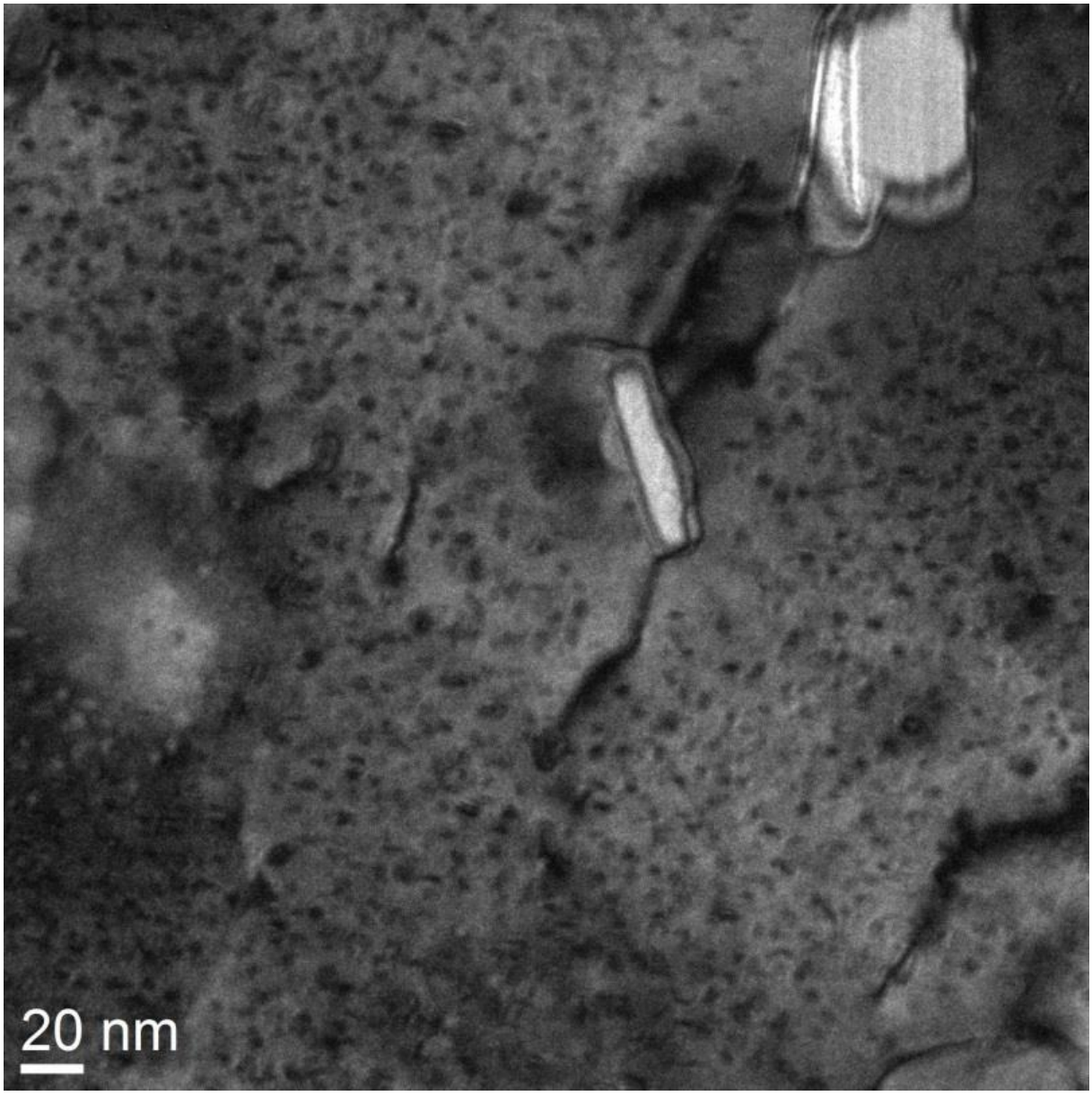

Figure E5. Distribution of GP zone and η′ precipitate in the aluminium matrix of the as-received sample.

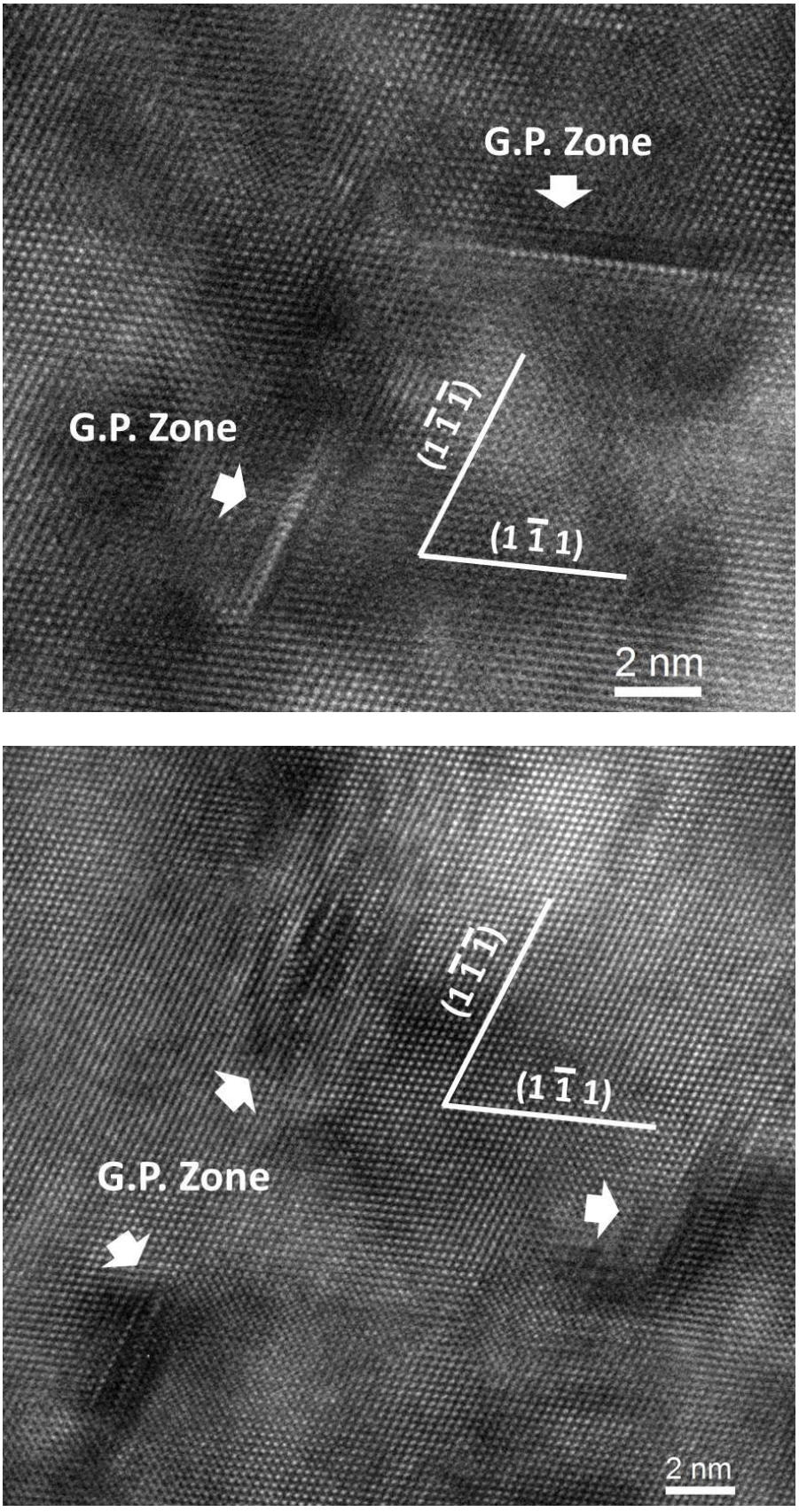

Figure E6. High resolution TEM images showing the distribution of GP zones in the aluminium matrix of the as-received sample.

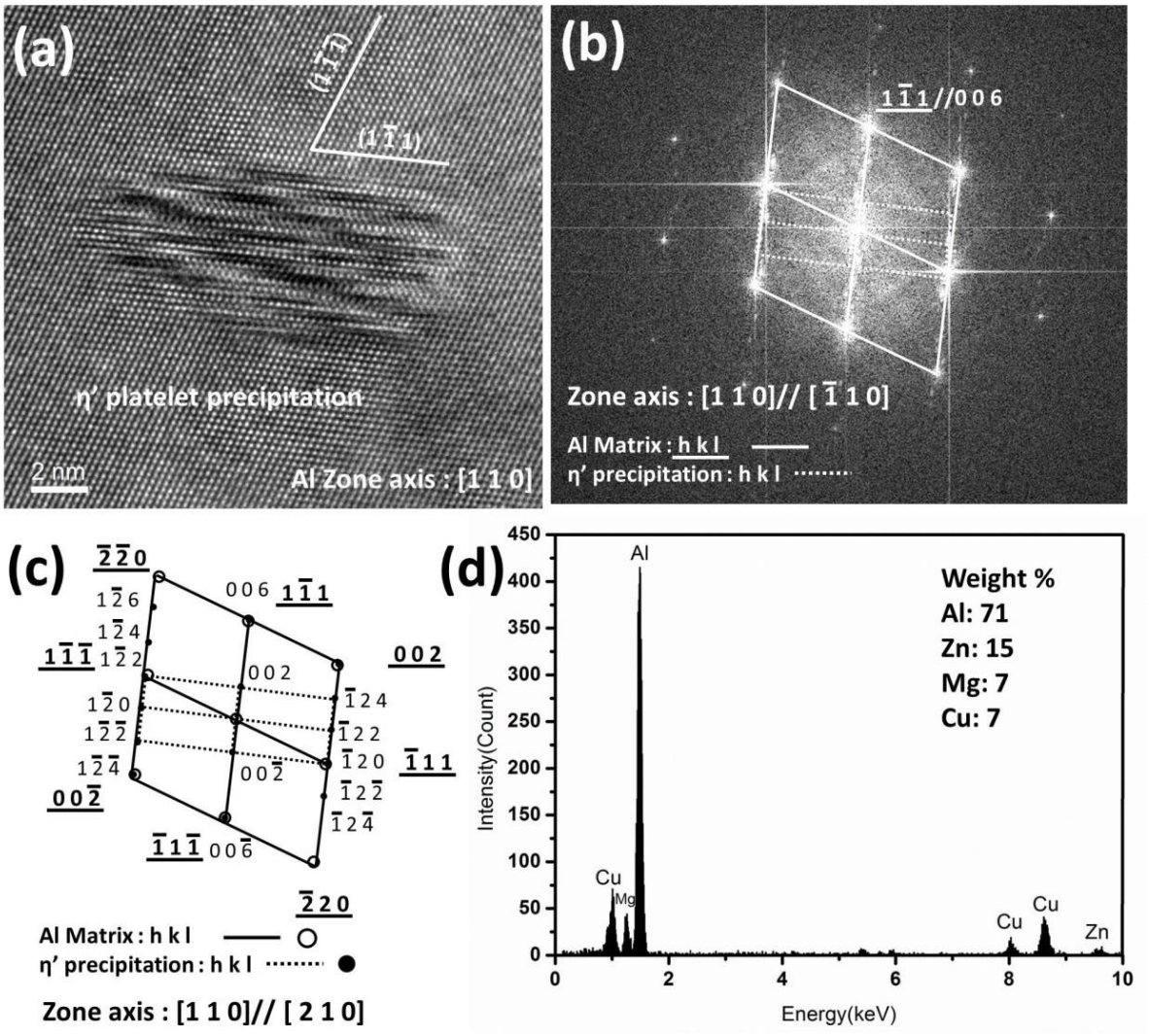

Figure E7. (a) High resolution TEM image showing the metastable precipitation η′ in the aluminium matrix of the as-received sample. (b) The corresponding FFT image from (a). (c) A schematic illustration of diffraction patterns for precipitation and the aluminium matrix. (d) The corresponding EDX spectrum for precipitation image from (a).

E3. Analysis results of the 22-h-stress-free-aged sample

The TEM analysis results of the 22-h-stress-free-aged sample are presented in this section. Figure E8 shows the micrograph of its FCC grains distribution. Figure E9 shows a high resolution image of its GP zones in the aluminium matrix. Figure E10 shows a high resolution image of its metastable η′ precipitate and the corresponding EDX spectrum.

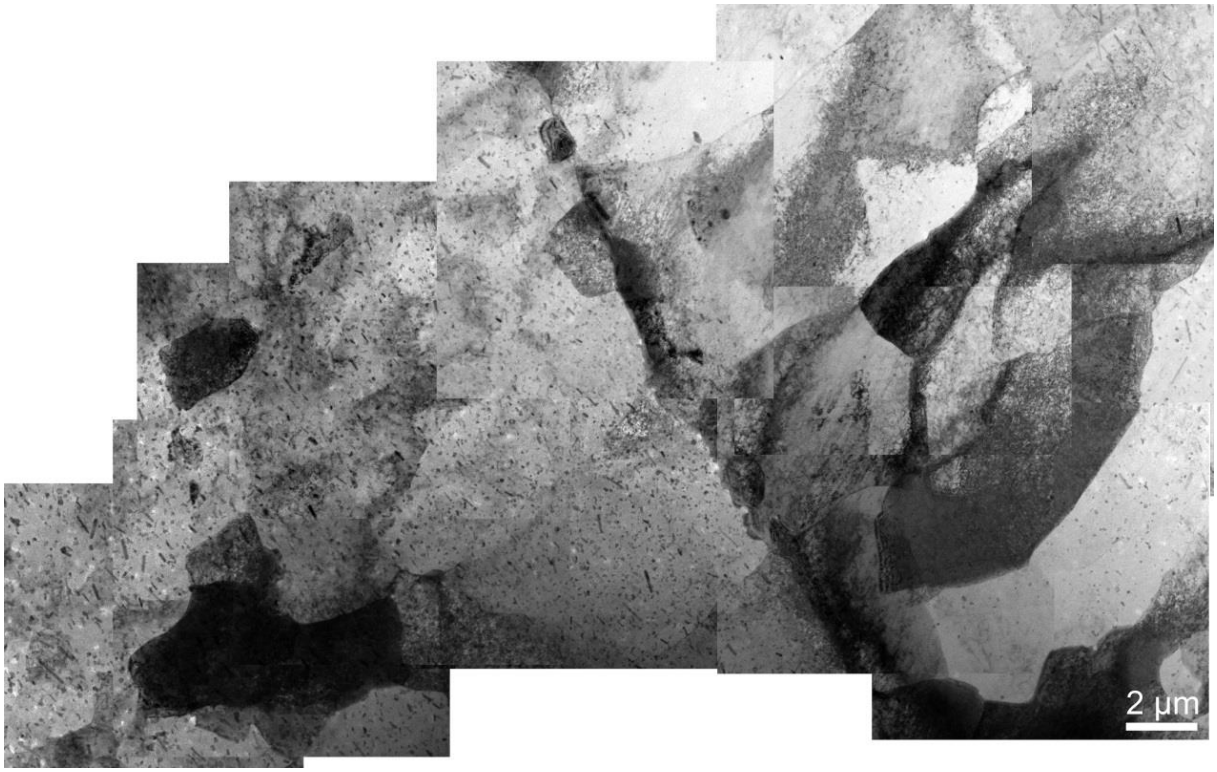

Figure E8. TEM micrograph showing the distribution of FCC grains of the 22-h-stress-free-aged sample.

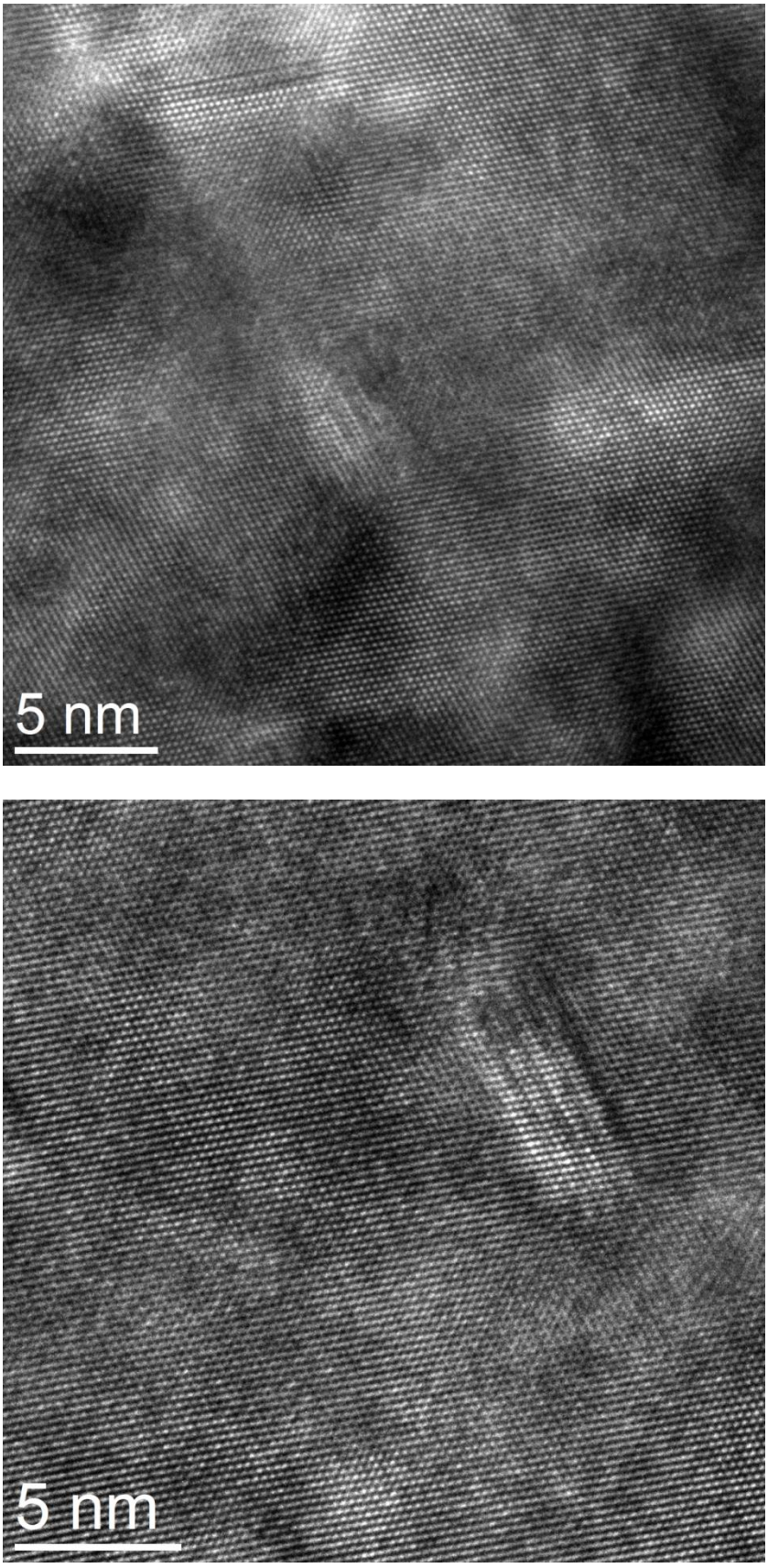

Figure E9. High resolution TEM image showing the GP zones in the aluminium matrix of the 22-h-stress-free-aged sample.

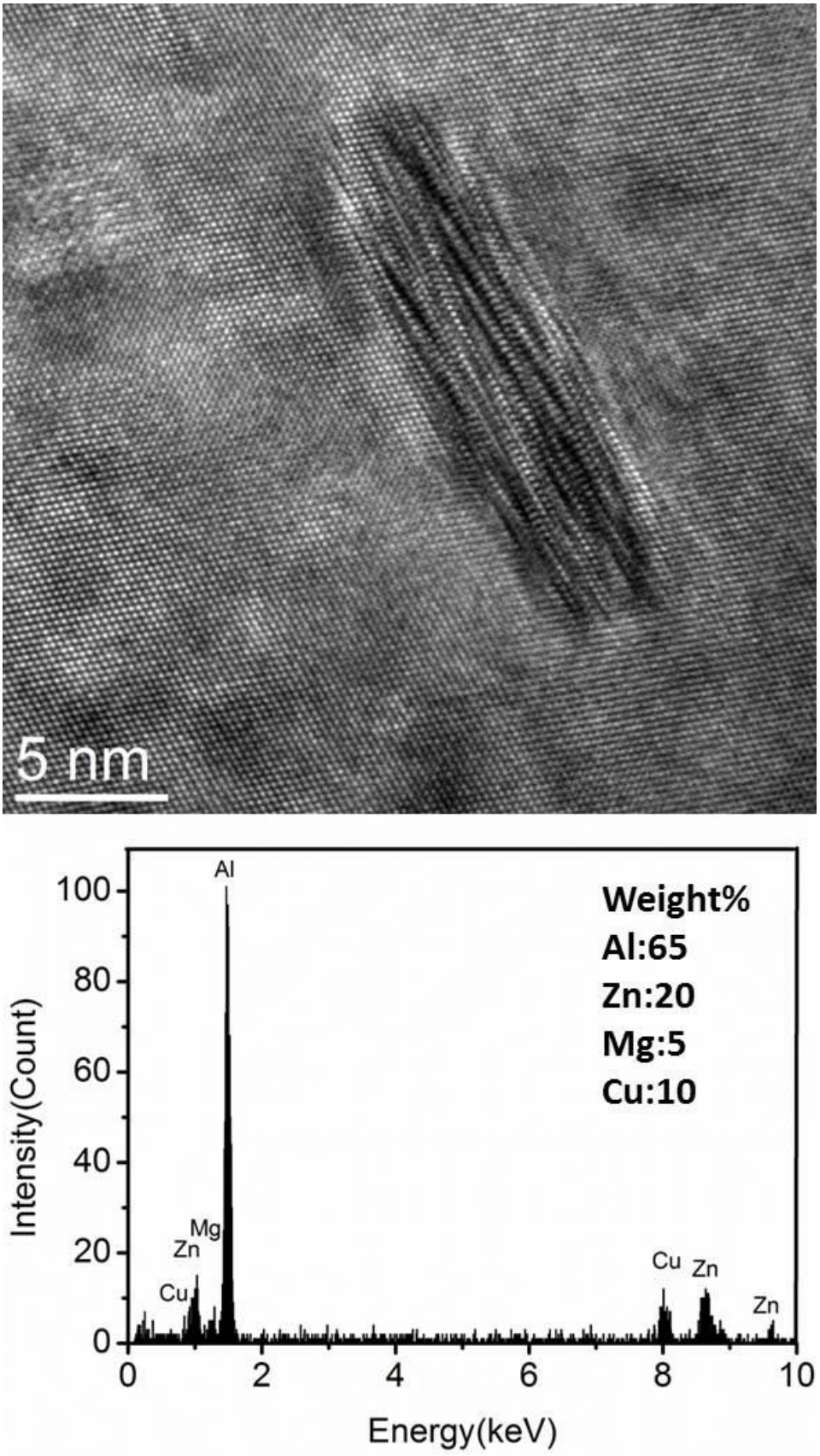

Figure E10. High resolution TEM image showing the metastable η′ precipitate in the aluminium matrix of the 22-h-stress-free-aged sample and the corresponding EDX spectrum.

E4. Concluding remarks

- Both the as-received and 22-h-stress-free-aged samples contain numerous Mn-rich precipitates.
- The GP zone and η′ precipitate co-existed in both samples.
- The average size of η′ precipitate is estimated to be 8.5 nm and 12.6 nm respectively in the as-received and 22-h-stress-free-aged samples.

APPENDIX F.

TENSILE STRESS-STRAIN CURVES

F1. Engineering tensile stress-strain curves of the as-received and creep-aged 7B04-T651 test pieces

Figure F1 shows the engineering stress-strain behaviour of the as-received test piece, as well as those after creep-ageing at 200, 240, 260 and 280 MPa under 115 °C for 22 h. Yield strength of the material is determined as the 0.2% proof stress in this thesis.

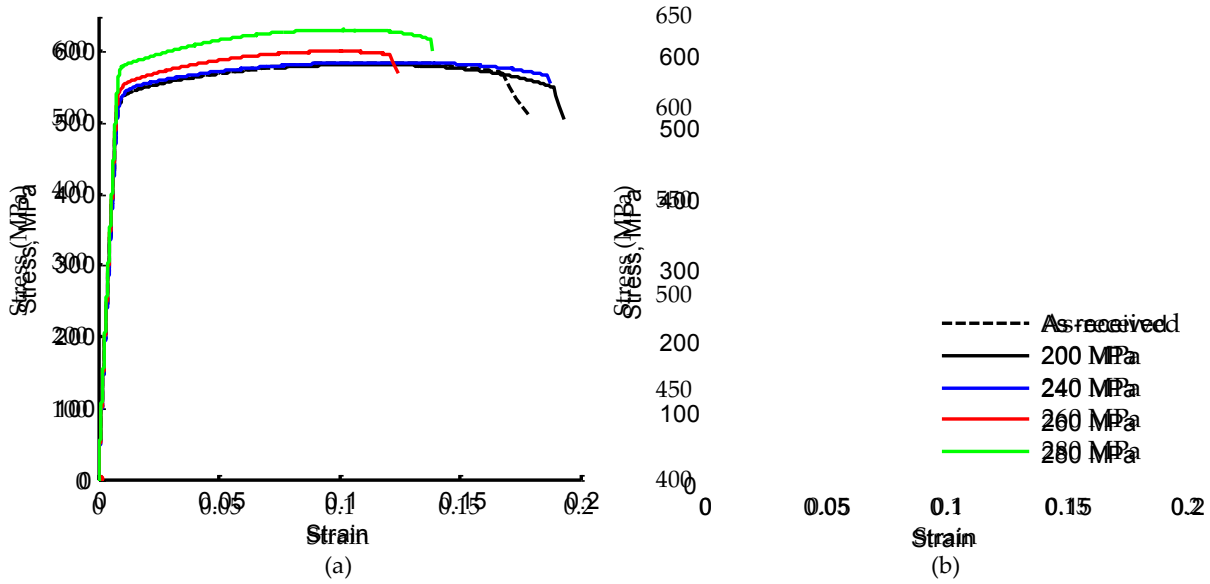

Figure F1. Engineering stress-strain behaviour of the creep-aged alloy (115 °C, 22 h) under the indicated applied stress levels with (a) and (b) showing the same results but having a different scale applied to the vertical axis.

APPENDIX G.

FINITE ELEMENT MESH CONVERGENCE STUDIES

G1. Design of mesh convergence studies

The mesh convergence studies were performed on one-mesh-at-a-time on the deformable FE meshes. Table G1 presents the order of convergence studies carried out and the method of determining the number of elements in each mesh for each study. Convergence study of the full splines mesh was first carried out. Table G2 presents the initial number of elements used for the spline mesh convergence study.

Table G1. Order of the convergence studies carried out and the method of determining the number of elements in each mesh for each study.

Order of study	Mesh studied	Method of determining the number of elements (n) in the other meshes	
		By initial guess	Using the converged n from previous study
1.	Full splines	Elastomeric sheet Panel component	
2.	Elastomeric sheet	Panel component	Splines
3.	Panel component		Splines Elastomeric sheet

Table G2. Number of elements (n) used for the spline mesh convergence study.

Mesh	n
Full splines	30
Elastomeric sheet	2900
Panel component	240

G2. Results

Convergences were achieved for the splines' shape and both the shape and stress state of the panel component. Figure G1 shows the convergences of the normalised deflection and maximum von Mises stress values with increasing number of elements (n) in a full spline. The spline's shape has fully converged at $n = 420$ with its maximum stress value also satisfying 98% of convergence.

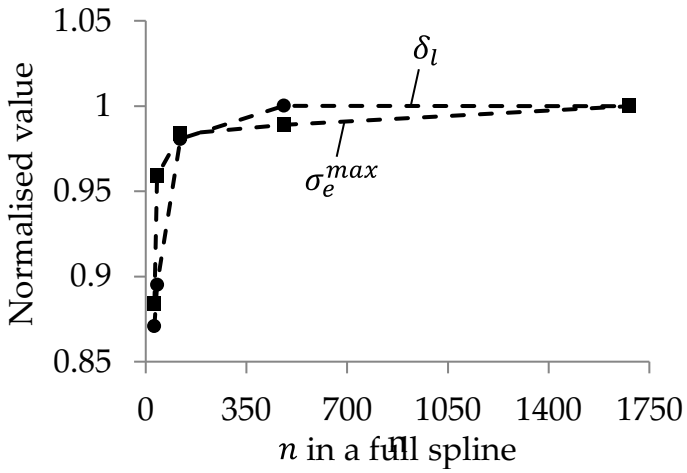

Figure G1. Convergences of the spline's fully loaded deflection (solid line) and maximum von Mises stress (dashed line) with increasing number of elements (n) in a full spline.

Figure G2a shows the change in normalised maximum von Mises stress value with increasing n in the elastomeric sheet and computational time, measured as CPU time. Local stress concentrations exist in the elastomeric sheet due to the small contact area between the rigid workheads and elastomeric sheet, which leads to stress singularity and hence an increasing stress value with n. Within the range of n studied, CPU time has increased significantly from around 6 minutes to over 1 h with increasing n. Further examination on the change in blank shape due to varying n of the elastomeric sheet shows no influence by the mesh condition of the elastomeric sheet (Figure G2b).

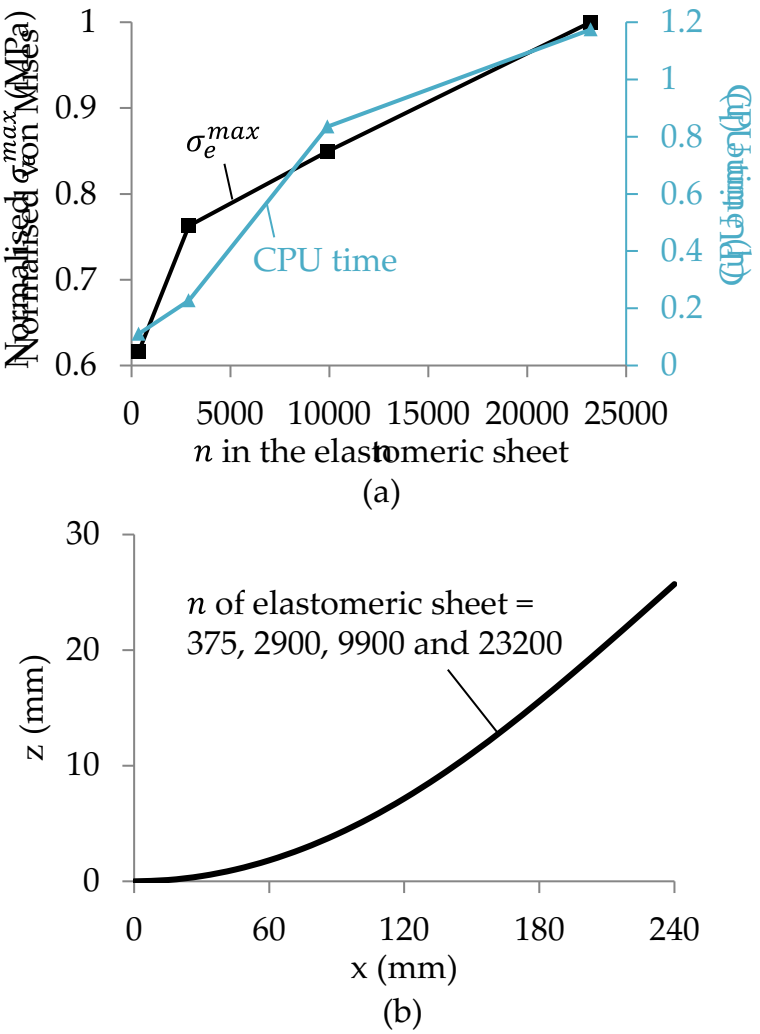

Figure G2. (a) Convergences of the maximum von Mises stress of the elastomeric sheet (square markers) with increasing number of elements (*n*) and computational time (triangular markers). (b) The fully loaded blank shapes with varying *n* in the elastomeric sheet.

Figure G3 shows the convergences of the von Mises stress and final deflection of the panel component with increasing n and CPU time. Convergences of both the stress and deflection values were achieved at approximately n = 2100. A final simulation with a much finer mesh at n = 8400 shows no significant change in the converged values but with CPU time increased significantly from 4 to 12 h.

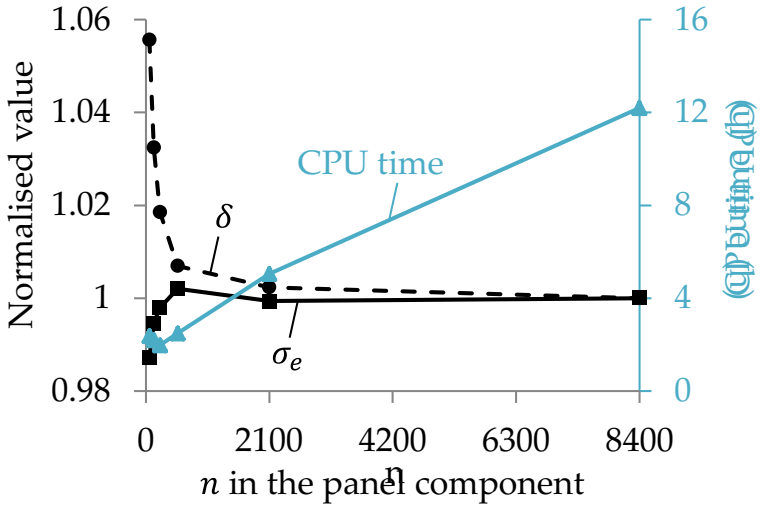

Figure G3. Convergences of the von Mises stress of an arbitrary element of the panel component (solid line) and its final deflection (dashed line) with increasing number of elements in the panel component and computational time.

Table G3 summarises the outcome of this appendix, showing the number of elements in the final convergent FE meshes.

Table G3. Number of elements in the final finite element meshes.

Mesh	n	Approximate global size
Full splines	420	5
Elastomeric sheet	2900	6
Panel component	2100	5